nature portfolio

https://doi.org/10.1038/s41929-021-00732-9

Supplementary information

Enhancing the stability of cobalt spinel oxide towards sustainable oxygen evolution in acid

Supplementary Information

Enhancing the Stability of Cobalt Spinel Oxide Towards Sustainable Oxygen Evolution in Acid

Ailong Li[†], Shuang Kong[†], Chenxi Guo[†], Hideshi Ooka, Kiyohiro Adachi,
Daisuke Hashizume, Qike Jiang, Hongxian Han, Jianping Xiao* and Ryuhei Nakamura*

*Corresponding Authors. E-mail: xiao@dicp.ac.cn and ryuhei.nakamura@riken.jp
[†]These authors contributed equally to this work

Table of Contents (Sections Below are Based on the Main Text)

Catalyst Characterization

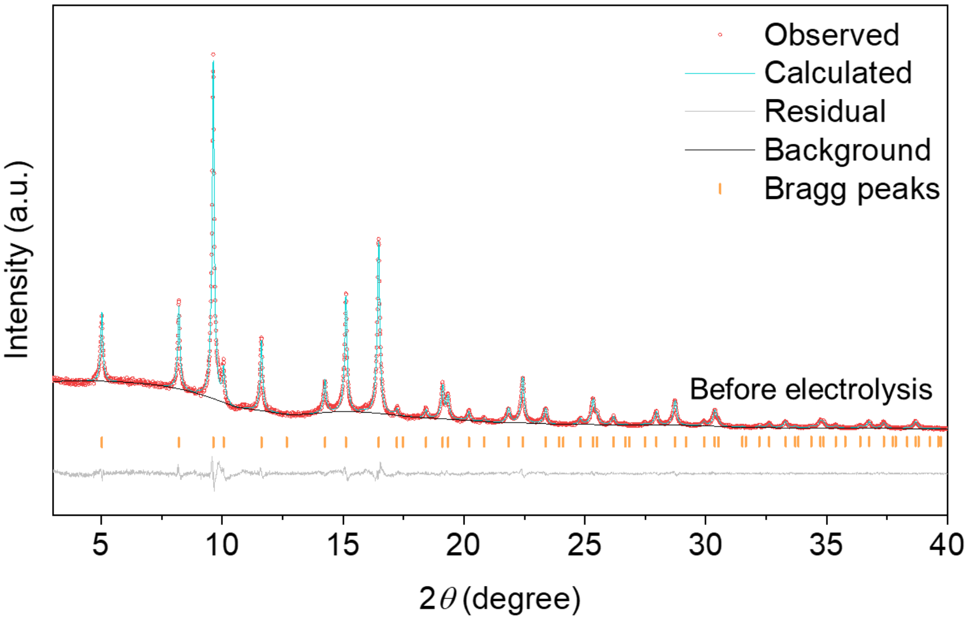

Supplementary Figure 1. Rietveld refinement for Co_2MnO_4 before electrolysis. Rietveld refinement for the synchrotron radiation powder X-ray diffraction (SR-PXRD) profile of Co_2MnO_4 before electrolysis. The experimental data are shown in red. The fitted curve, residual, and Bragg peaks are shown in light blue, grey, and brown, respectively. The structural parameters derived from Rietveld refinement were given in Supplementary Table 1. Detailed procedures for Rietveld refinement are provided in the Supplementary Note 1.

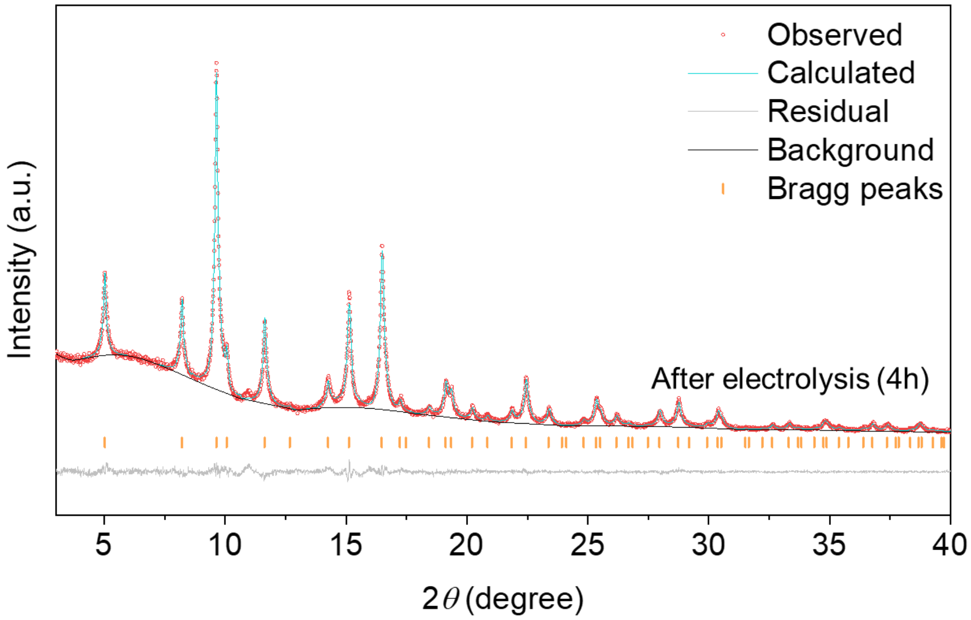

Supplementary Figure 2. Rietveld refinement for Co_2MnO_4 after electrolysis for 4 hours. Rietveld refinement for the SR-PXRD profile of Co_2MnO_4 after electrolysis at 100 mA cm^{-2}_{geo} (pH 1 H_2SO_4, 25 °C) for 4 hours. The experimental data are shown in red. The fitted curve, residual, and Bragg peaks are shown in light blue, grey, and brown, respectively. The structural parameters derived from Rietveld refinement were given in Supplementary Table 2. Detailed procedures for Rietveld refinement are provided in the Supplementary Note 1.

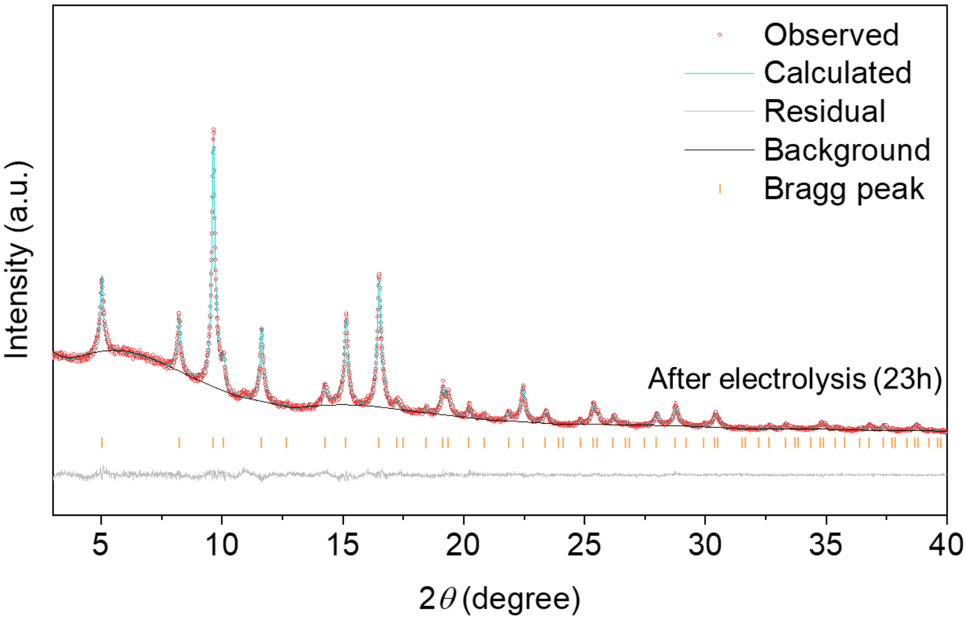

Supplementary Figure 3. Rietveld refinement for Co_2MnO_4 after electrolysis for 23 hours. Rietveld refinement for the SR-PXRD profile of Co_2MnO_4 after electrolysis at 100 mA cm^{-2}_{geo} (pH 1 H_2SO_4, 25 °C) for 23 hours. The experimental data are shown in red. The fitted curve, residual, and Bragg peaks are shown in light blue, grey, and brown, respectively. The structural parameters derived from Rietveld refinement were given in Supplementary Table 3. Detailed procedures for Rietveld refinement are provided in the Supplementary Note 1.

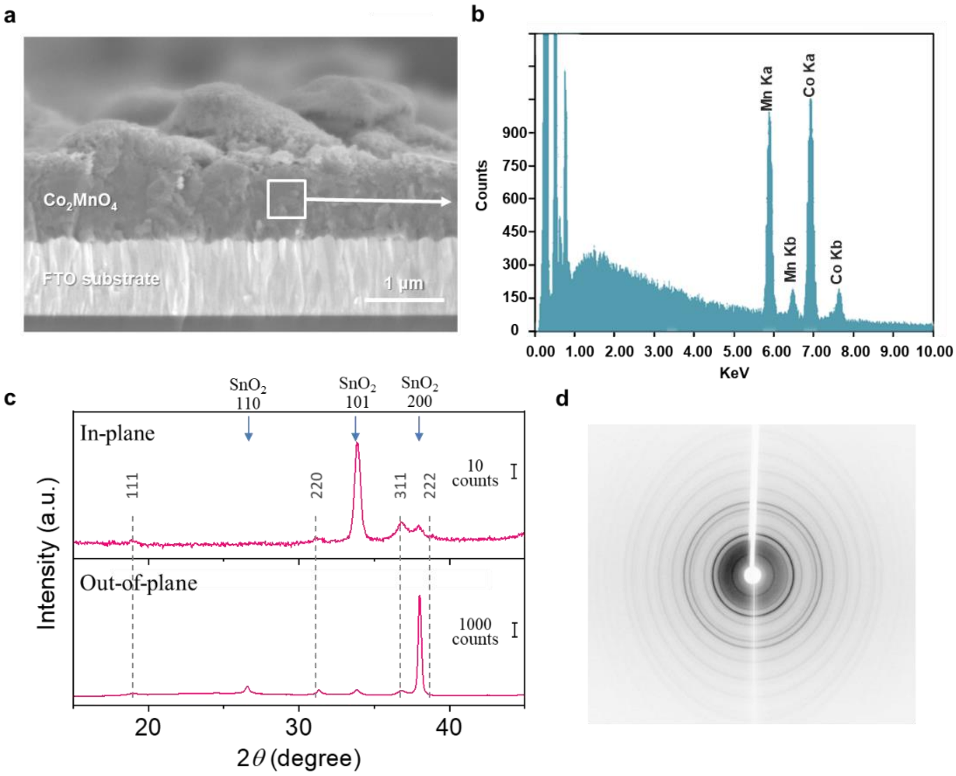

e Comparison of area ratio for each reflection peak (assume the strongest line 311 is 100%)

2θ (degree)	Reflection Index *hkl*	Relative intensity (%) SR-PXRD	Relative intensity (%) Out-of-plane	Relative intensity (%) In-plane
19.1	111	25	33	20
31.3	220	26	35	26
36.8	311	100	100	100
38.5	222	10	0	3

Supplementary Figure 4. Characterization of Co_2MnO_4 on FTO. a, Cross-sectional SEM image of Co_2MnO_4 on the FTO substrate. Scale bar, 1 µm. **b,** Energy-dispersive X-ray spectroscopy (EDX) spectrum of Co_2MnO_4 corresponding to the square region in (**a**), suggesting the atomic ratio of Co:Mn was 2:1. The Co:Mn atomic ratio of 2:1 was also confirmed by inductively coupled plasma mass spectrometry (ICP-MS) (Agilent7700). **c**, In-plane and out-of-plane XRD patterns of Co_2MnO_4 on FTO substrates. The positions and intensity ratios of these peaks were in good agreement with the diffraction pattern of the sample in an unoriented capillary measured by synchrotron radiation, suggesting the Co_2MnO_4 has no specific orientation (**e**). The lack of orientation can be confirmed based on the uniform Debye-Scherrer rings (**d**). For samples with strong preferred orientation, discrete spots (or arcs) will be observed.

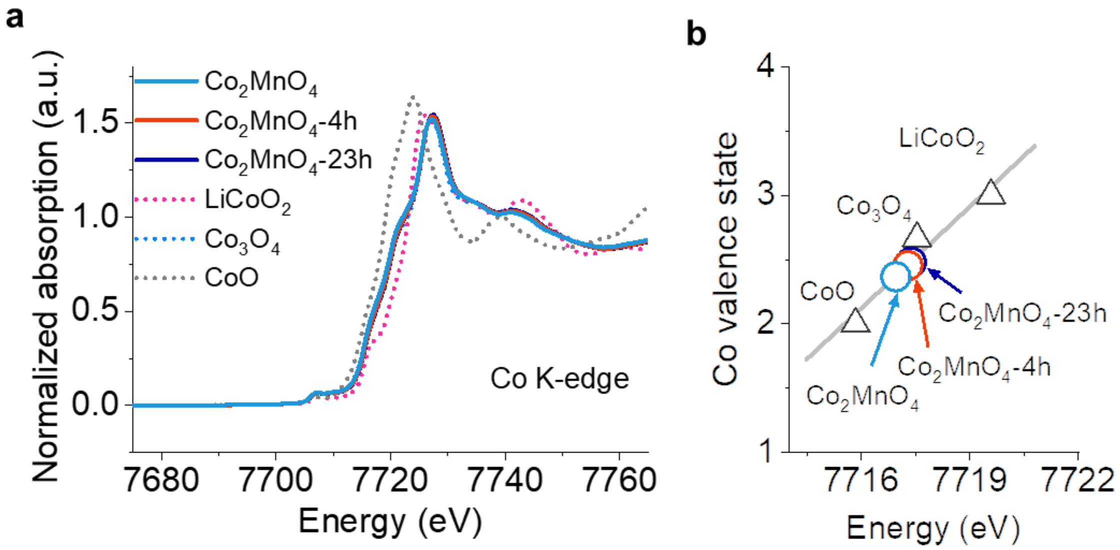

Supplementary Figure 5. Normalized Co K-edge XANES spectra of Co_2MnO_4. a, Normalized Co K-edge XANES spectra of Co_2MnO_4 before and after electrolysis at 100 mA cm^{-2}_{geo} (pH 1 H_2SO_4, 25 °C) for 4 hours (Co_2MnO_4-4h) and 23 hours (Co_2MnO_4-23h). The XANES spectra for Co_2MnO_4 before and after electrolysis for 23 hours were also presented in the main text. **b,** The K-edge position (defined as the energy where the normalized absorption is 0.5) vs Co oxidation states. CoO, Co_3O_4 and $LiCoO_2$ were tested as reference samples with known Co valence. The valence states of Co were determined to be 2.37, 2.45 and 2.48 for Co_2MnO_4 (before electrolysis), Co_2MnO_4-4h and Co_2MnO_4-23h, respectively.

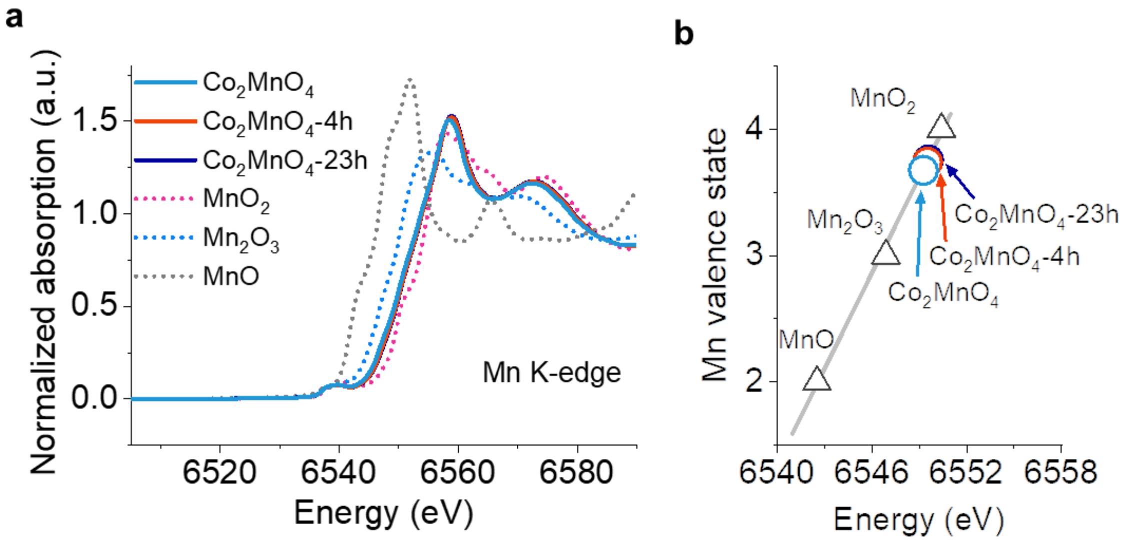

Supplementary Figure 6. Normalized Mn K-edge XANES spectra of Co_2MnO_4. Normalized Mn K-edge XANES spectra of Co_2MnO_4 before and after electrolysis at 100 mA cm^{-2}_{geo} (pH 1 H_2SO_4, 25 °C) for 4 hours (Co_2MnO_4-4h) and 23 hours (Co_2MnO_4-23h). The XANES spectra for Co_2MnO_4 before and after electrolysis for 23 hours were also presented in the main text. **b,** The K-edge position (defined as the energy where the normalized absorption is 0.5) Mn oxidation states. MnO, Mn_2O_3 and MnO_2 were tested as reference samples with known Mn valence. The valence states of Mn were determined to be 3.67, 3.74 and 3.76 for Co_2MnO_4 (before electrolysis), Co_2MnO_4-4h and Co_2MnO_4-23h, respectively.

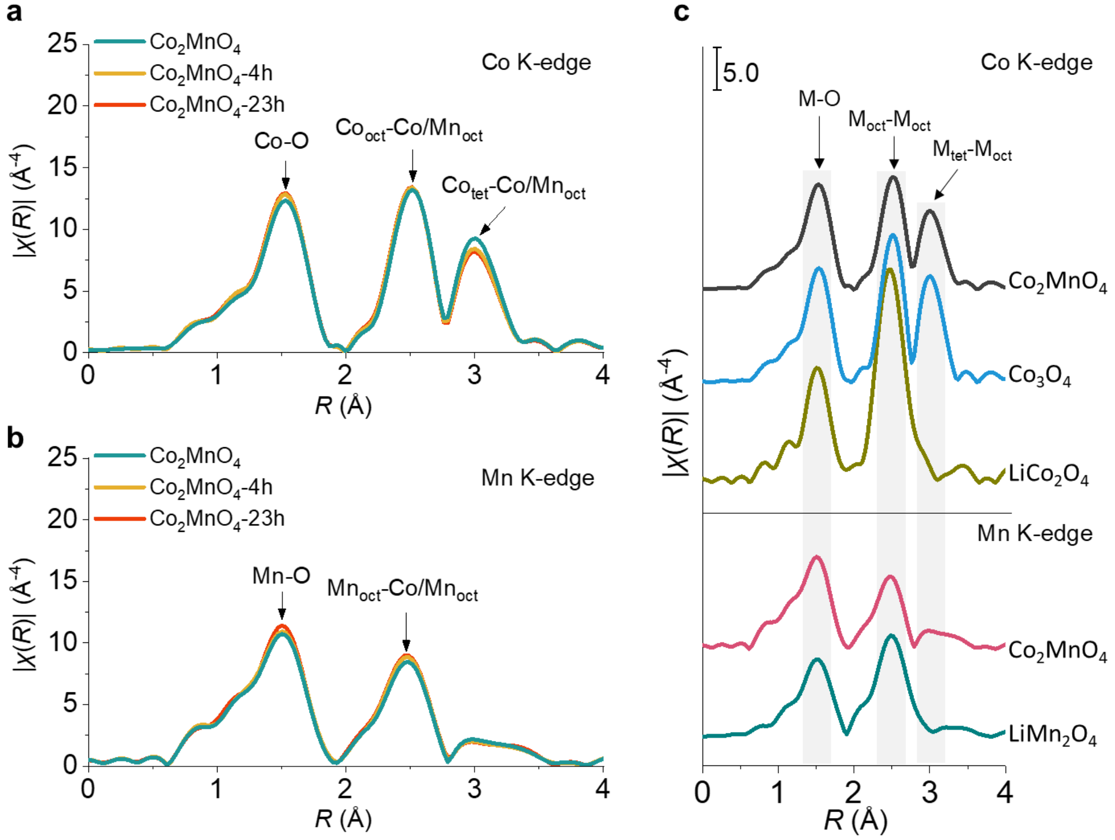

Supplementary Figure 7. Fourier transforms of Co K-edge and Mn K-edge EXAFS of Co_2MnO_4. Fourier transforms of Co K-edge (**a**) and Mn K-edge (**b**) EXAFS data for the Co_2MnO_4 before and after electrolysis at 100 mA cm^{-2}_{geo} (pH 1 H_2SO_4, 25 °C) for 4 hours (Co_2MnO_4-4h) and 23 hours (Co_2MnO_4-23h). “tet” and “oct” represent tetrahedral site (A-site) and octahedral site (B-site) in a spinel structure (AB_2O_4), respectively. The EXAFS results for Co_2MnO_4 before and after electrolysis for 23 hours were also present in the main text. **c,** A comparison of EXAFS data for the Co_2MnO_4 and reference spinel oxides with known Co and Mn coordination environment, such as Co_3O_4 (Co on both octahedral and tetragonal sites), $LiCo_2O_4$ (Co on octahedral sites) and $LiMn_2O_4$ (Mn on octahedral sites). Standard samples of Co_3O_4 and $LiCo_2O_4$ were test in this study. XAFS spectrum of standard sample $LiMn_2O_4$ is utilized by SPring-8 BL14B2 XAFS database.

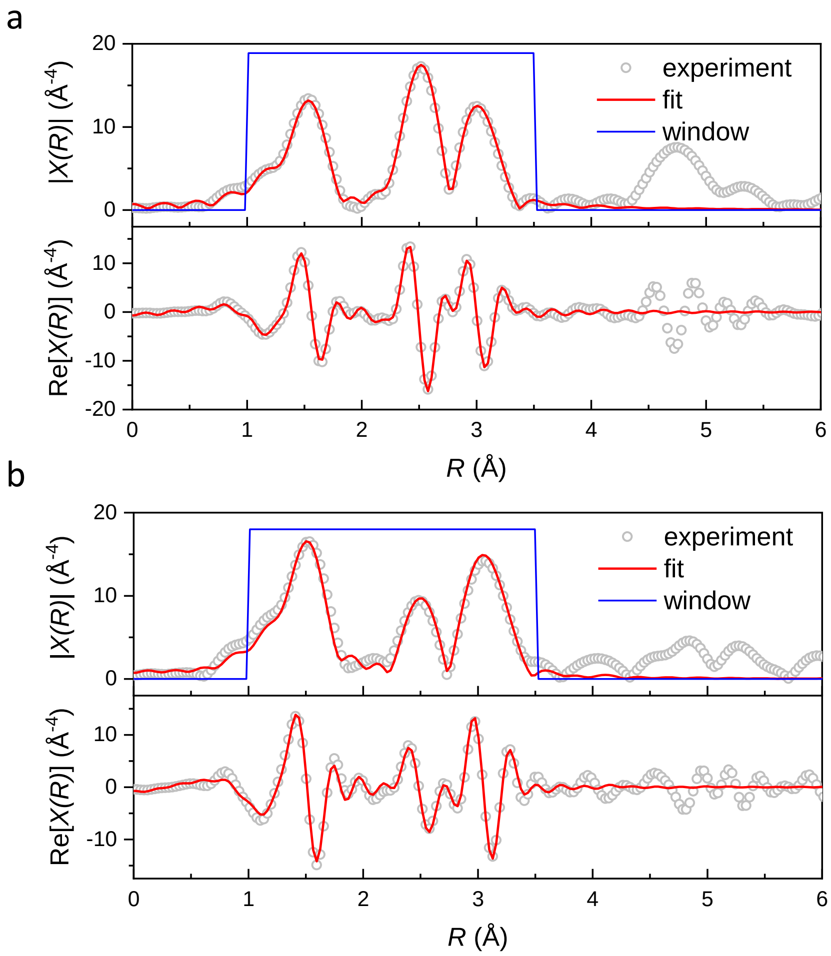

Supplementary Figure 8. EXAFS fitting for standard samples of Co$_3$O$_4$ and β-MnO$_2$. Fitting analysis of Fourier-transformed k^3-weighted Co K-edge EXAFS measurement of Co$_3$O$_4$ (**a**) and Mn K-edge EXAFS measurement of MnO$_2$ (**b**). The fitting was conducted within the *R* range of 1-3.5 Å, and optimized parameters can be found in Supplementary Table 4 (Co K-edge of Co$_3$O$_4$) and Supplementary Table 5 (Mn K-edge of MnO$_2$). In both (a) and (b), the upper panel shows the magnitude of FT-EXAFS, and the lower panel shows its real part. Detailed procedures for fitting are provided in the Supplementary Note 2.

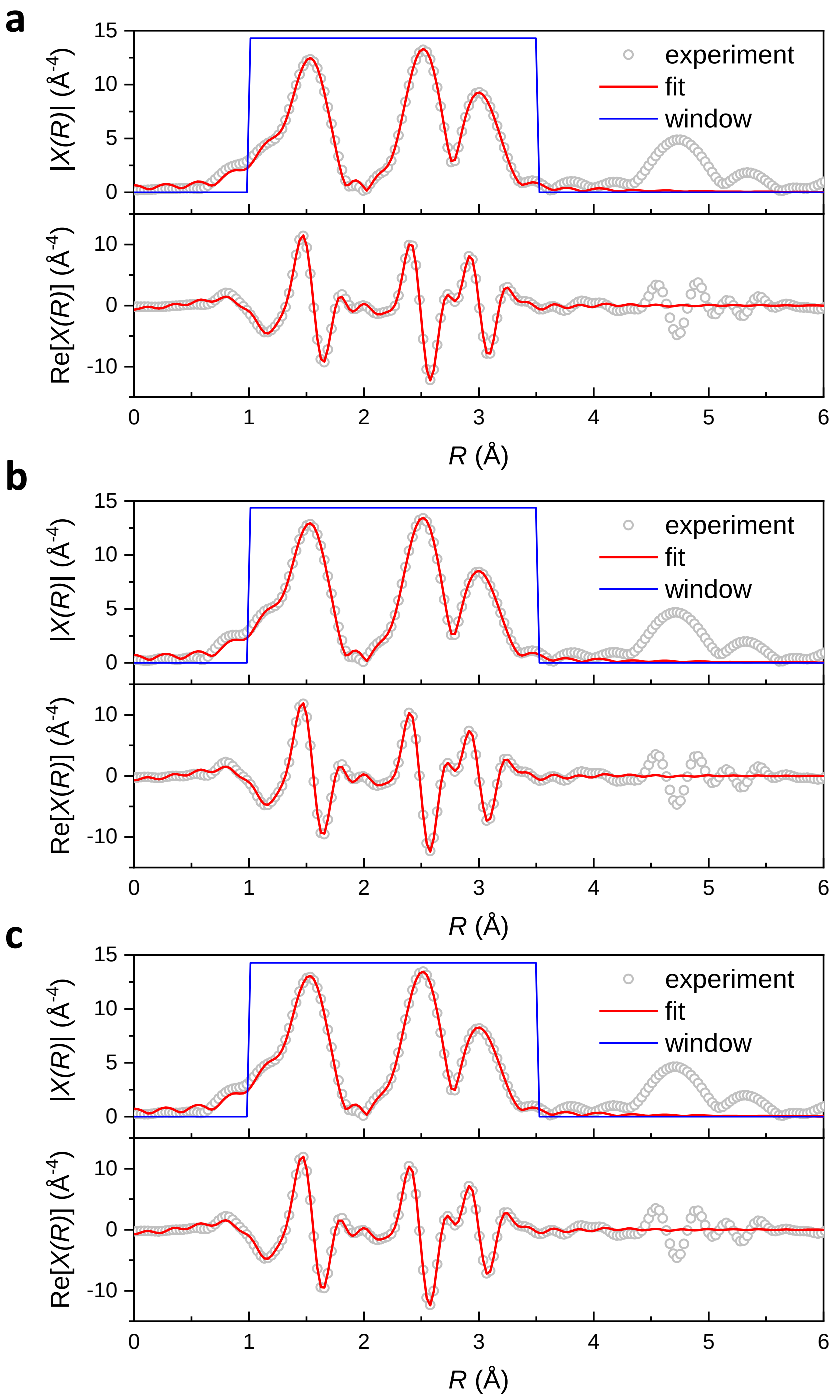

Supplementary Figure 9. Co K-edge EXAFS fitting for Co$_2$MnO$_4$. Fitting analysis of Fourier-transformed k^3-weighted Co K-edge EXAFS measurements before (**a**) and after electrolysis for 4 hours (**b**) and 23 hours (**c**). Electrolysis was conducted at 100 mA cm$^{-2}_{geo}$ in pH 1 H$_2$SO$_4$ at 25 °C. The fitting was conducted within the *R* range of 1-3.5 Å, and optimized parameters can be found in Supplementary Table 6. In (**a**), (**b**) and (**c**), the upper panel shows the magnitude of FT-EXAFS, and the lower panel shows its real part. Detailed procedures for fitting are provided in the Supplementary Note 2.

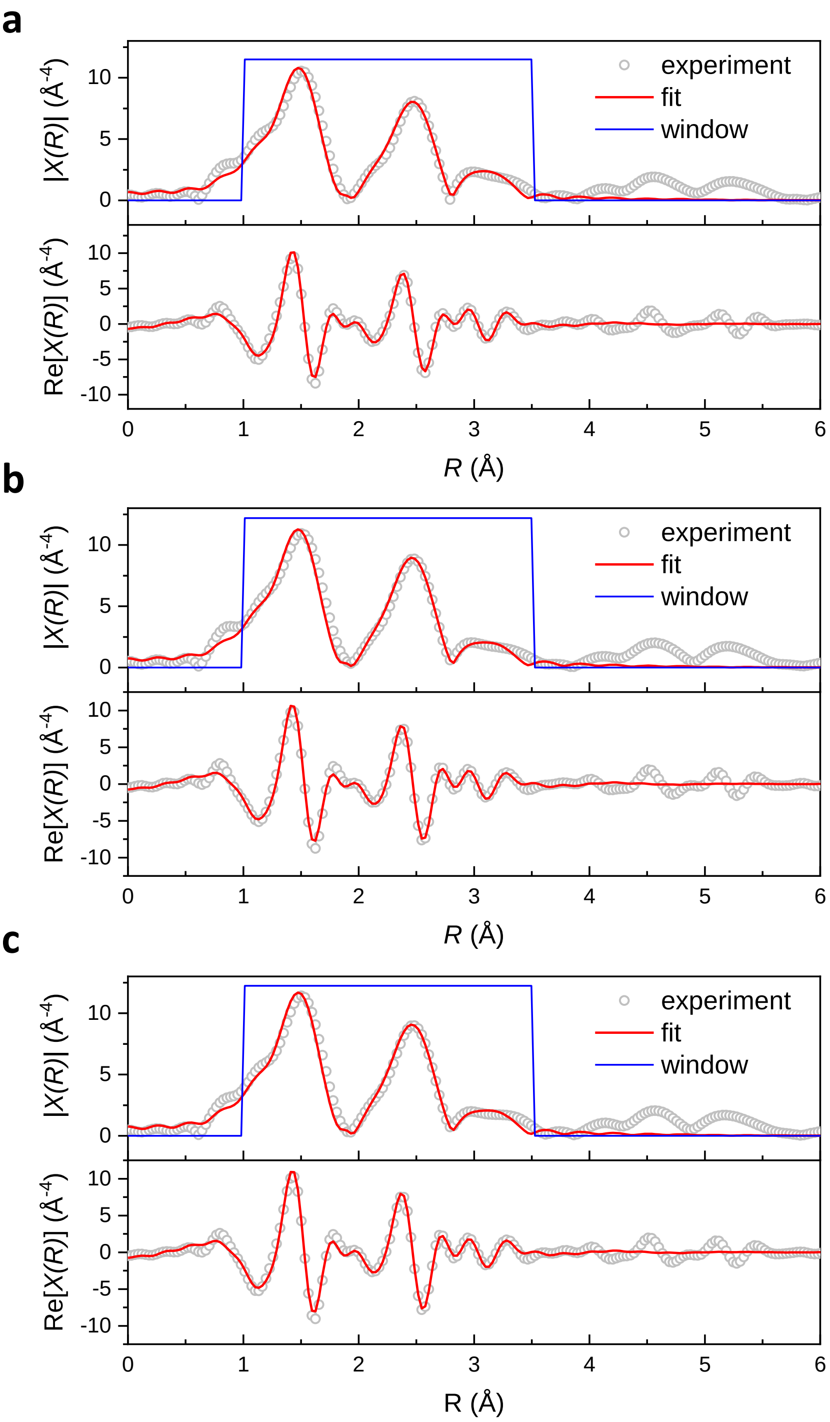

Supplementary Figure 10. Mn K-edge EXAFS fitting for Co_2MnO_4. Fitting analysis of Fourier-transformed k^3-weighted Mn K-edge EXAFS measurements before (**a**) and after electrolysis for 4 hours (**b**) and 23 hours (**c**). Electrolysis was conducted at 100 mA cm$^{-2}_{geo}$ in pH 1 H_2SO_4 at 25 °C. The fitting was conducted within the *R* range of 1-3.5 Å, and optimized parameters can be found in Supplementary Table 7. In (**a**), (**b**) and (**c**), the upper panel shows the magnitude of FT-EXAFS, and the lower panel shows its real part. Detailed procedures for fitting are provided in the Supplementary Note 2.

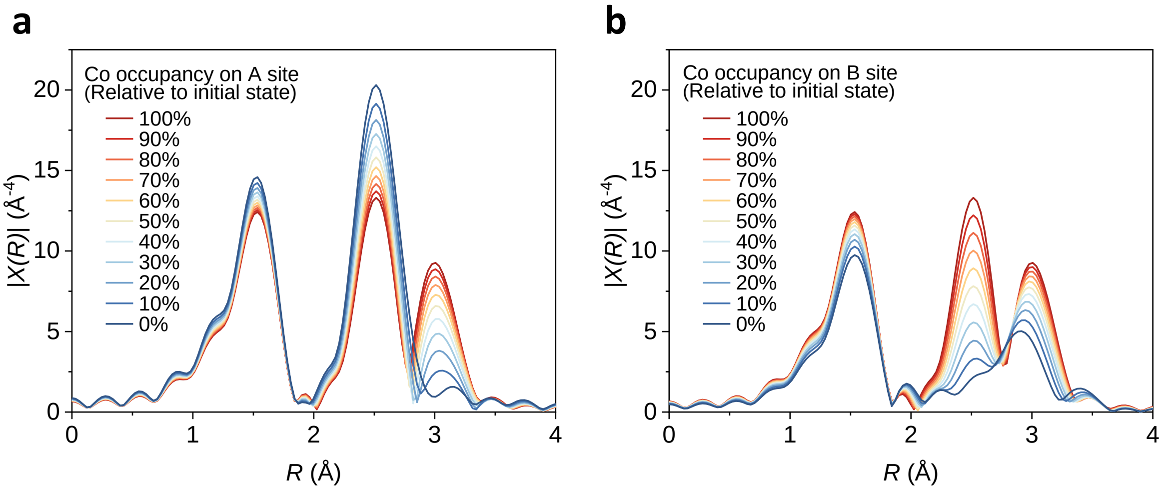

Supplementary Figure 11. EXAFS simulation for Co_2MnO_4 with various occupancies. Simulated EXAFS data of spinel Co_2MnO_4 at various occupancies at the Co A-site **(a)** and B-site **(b)**. No structural parameters other than the occupancy was changed across the simulations. Detailed procedures for simulation are provided in the Supplementary Note 2. The occupancies indicated are relative to the occupancies of the as-synthesized material (84% for the A-site, 53% for the B-site).

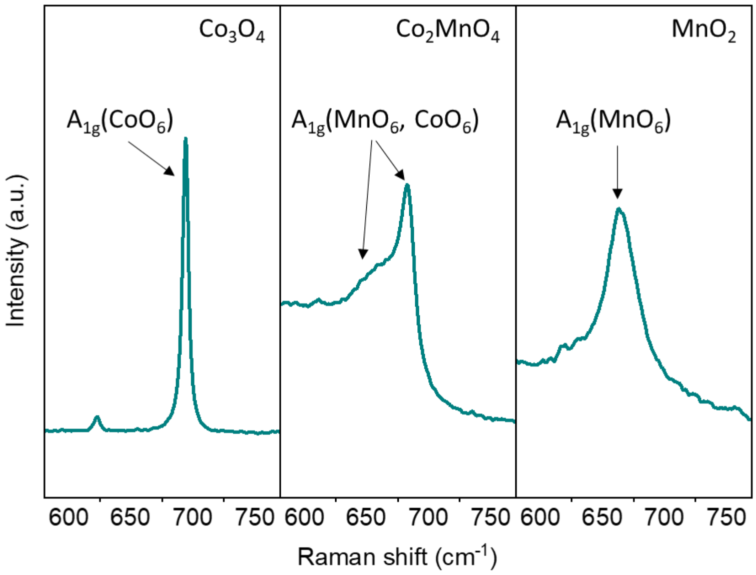

Supplementary Figure 12. Raman spectra of Co_2MnO_4. Raman spectra revealed characteristic symmetric stretching vibration bands (A_{1g}) of octahedral sites at 650-700 cm^{-1} (refs.[1-3]). This is a single peak in spinel Co_3O_4 and rutile MnO_2, whereas it splits into two components in the case of Co_2MnO_4 due to the coexistence of octahedral based on both MnO_6 (ref. [1]) and CoO_6 (refs. [2,3]). The Raman modes at 620 cm^{-1} (F_{2g}) are assigned to combined vibrations of tetrahedral site and octahedral oxygen motions[4].

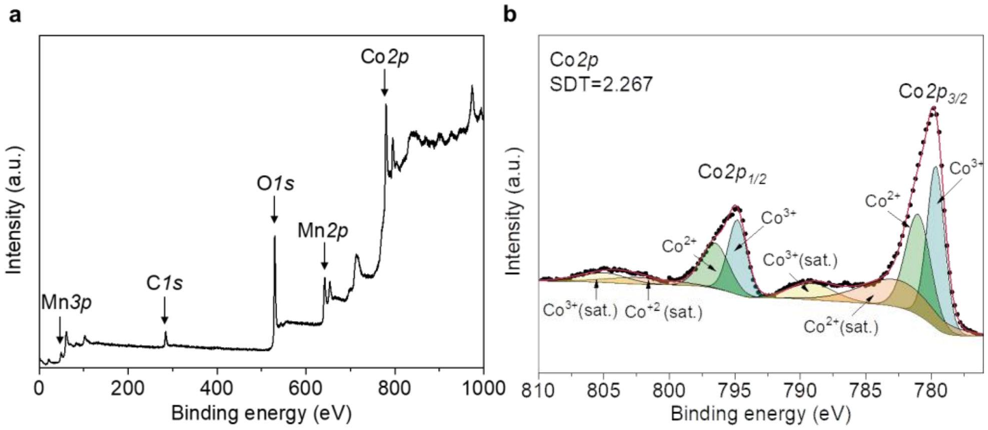

Supplementary Figure 13. XPS Co*2p* spectrum of Co_2MnO_4. a, XPS survey spectrum of the Co_2MnO_4 catalyst. **b**, High resolution spectrum of Co*2p* region. The Co*2p* spectrum was fitted by considering two spin-orbit doublets characteristic of Co^{2+} (refs. [5,6]), Co^{3+} (ref. [7]) and shakeup satellites. XPS fitting[5-7] analysis shows that the ratio of Co^{2+}:Co^{3+} is approximate 1:1, indicating the average valence state of Co is about 2.50. All high-resolution spectra were collected using a pass energy of 23.5 eV and calibrated using the C*1s* peak at 284.6 eV. Co*2p* spectral fitting parameters are presented in the Supplementary Table 8**.**

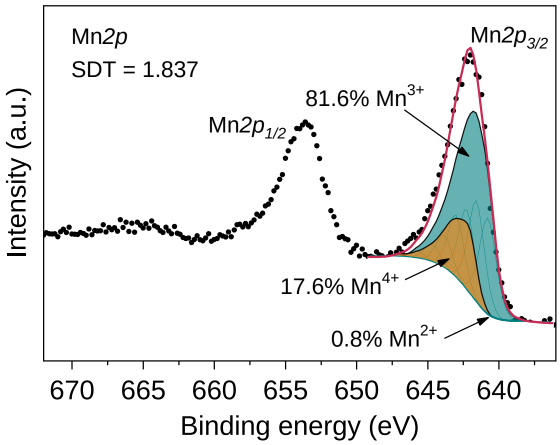

Supplementary Figure 14. XPS Mn*2p* spectrum of Co_2MnO_4. XPS spectra of Mn*2p* in Co_2MnO_4 catalyst. An determination of Mn oxidation states can be obtained by Mn$2p_{3/2}$ fitting[8]. The predominant oxidation states are Mn^{3+} (81.6%) and Mn^{4+} (17.6%), indicating the average valence state of Mn is about 3.16. Mn^{2+} (0.8%) is within the detection limit of XPS (1 at.%) and is ignored in the analysis. The spectra were obtained using a pass energy of 23.5 eV and calibrated using the C*1s* peak at 284.6 eV. The absolute octahedral site preference energies from the literature[9,10] increase in the order Co^{2+} (31.0 kJ mol^{-1}) < Co^{3+} (79.5 kJ mol^{-1}) < Mn^{3+}/Mn^{4+} (95.2 kJ mol^{-1}), indicating that Mn^{3+}/Mn^{4+} together with Co^{3+} prefer to occupy the octahedral sites while Co^{2+} tends to occupy the tetrahedral sites in the spinel structure of Co_2MnO_4. The site preference is also consistent with our EXAFS data (Supplementary Fig. 7) and Rietveld refinements (Supplementary Figs. 1-3). Mn*2p* spectral fitting parameters are presented in the Supplementary Table 11.

Electrochemical Analysis

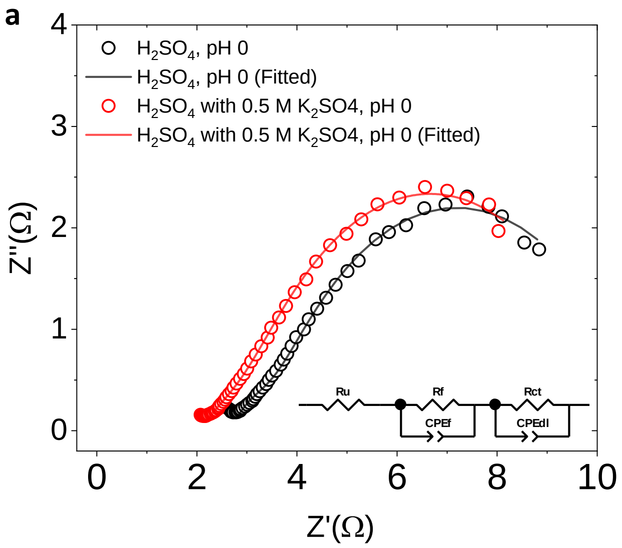

b

	H_2SO_4 pH 0	**H_2SO_4 with 0.5 M K_2SO_4, pH 0**
R/Ω	2.6	2.2
R_f/Ω	1.36	0.66
CPE_f/F	0.06	0.04
R_{ct}/Ω	6.8	7.84
CPE_{dl}/F	0.1	0.1

Supplementary Figure 15. EIS plots of Co_2MnO_4. a, EIS profiles of Co_2MnO_4 on the FTO substrate in H_2SO_4 (pH 0) and H_2SO_4 with 0.5 M K_2SO_4 (pH 0), measured at 1.7 V vs. RHE, from 100 kHz to 0.1 Hz. Geometric area, 0.28 cm^2. The equivalent circuit used to model the data is shown as an inset. The electrical circuit[11] consists of the solution resistance (R), film resistance (R_f), and charge transfer resistance (R_{ct}). The capacitive elements used, CPE_f and CPE_{dl}, represent the constant phase element of the film and the electrical double layer, respectively. The fitting parameters are presented in (**b**). The ohmic resistance was suppressed by adding 0.5 M K_2SO_4 to the electrolyte. Therefore, we added K_2SO_4 for all experiments unless otherwise specified.

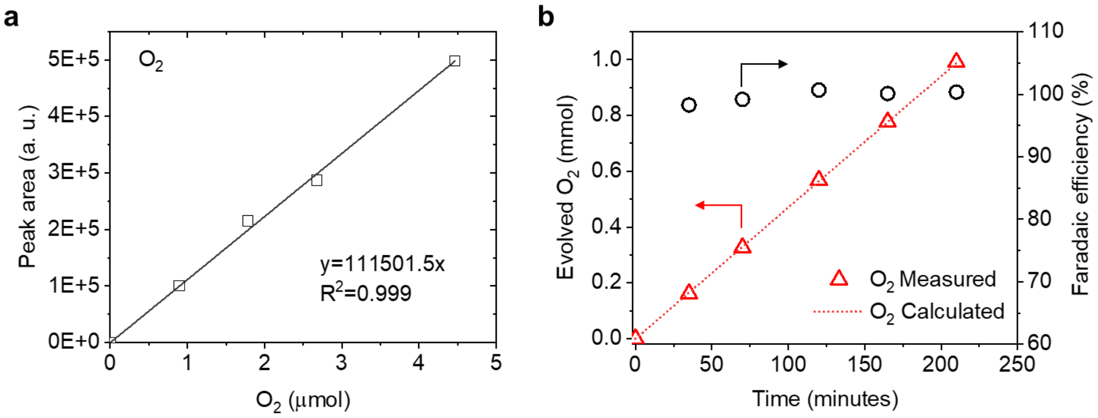

Supplementary Figure 16. Faradaic efficiency measurement. a, GC-MS calibration curve for O_2. **b**, Faradaic efficiency (black circles) of OER on Co_2MnO_4 deposited on FTO at a constant current density of 100 mA cm^{-2}_{geo} in pH 1 H_2SO_4 at 25 °C. The Faradaic efficiency was calculated by dividing the amount of evolved oxygen observed from GC measurements (red triangles) with the amount of oxygen expected from the charge passing through the working electrode. The red dotted line corresponds to 100% Faradaic efficiency.

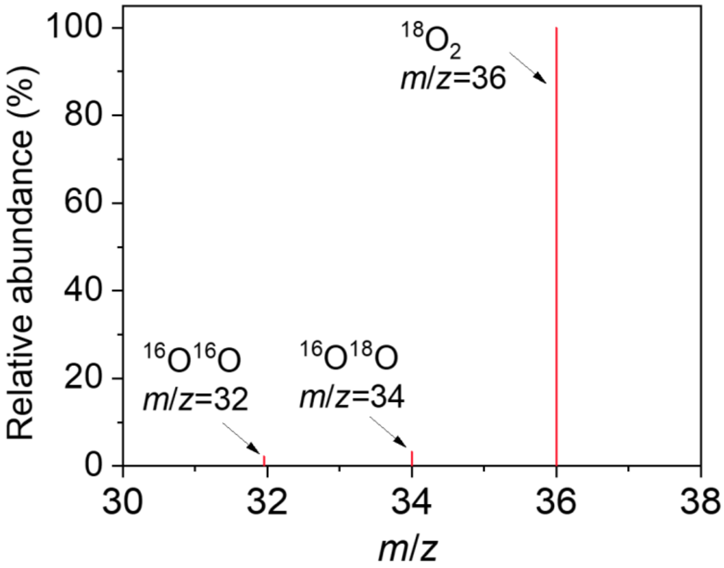

Supplementary Figure 17. Isotope distribution of dioxygen measured by GC-MS. OER was conducted in $H_2{}^{18}O$ (^{18}O purity ≥ 98 atom%) using $H_2S^{16}O_4$ as the electrolyte at pH 0, at 100 mA $cm^{-2}{}_{geo}$ (roughly 1.72 V vs RHE, after iR correction) for 23 h. The peak at $m/z = 32$ is due to atmospheric contamination, as it can be observed at similar levels even if pure He was injected (O_2 injection: 31269 counts, He injection: 30012 counts).

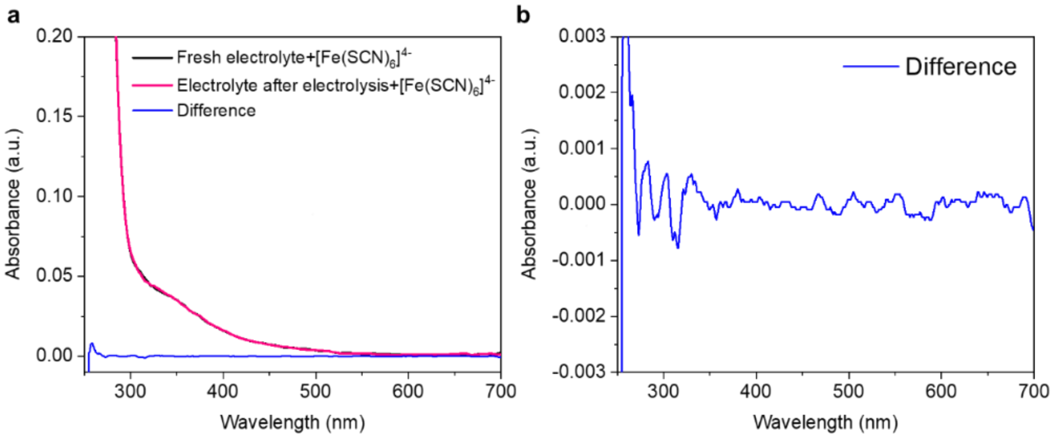

Supplementary Figure 18. Evaluation of H_2SO_4 oxidation by colorimetry. a, UV-Vis spectra of the electrolyte with 5 mM $[Fe(SCN)_6]^{4-}$. The electrolyte was sampled before and after electrolysis at 100 mA cm^{-2}_{geo} (1.72 V vs RHE after *iR* correction) for 23 hours. The subtracted spectrum was enlarged and shown in (**b**). No peak assignable to $[Fe(CN)_6]^{3-}$ could be observed (molar extinction coefficient = 6120 $M^{-1}cm^{-1}$ at 470 nm), showing that the possibility of $[Fe(SCN)_6]^{3-}$ formation by the oxidation of $[Fe(CN)_6]^{4-}$ by $S_2O_8^{2-}$ is below the detection limit (1.6×10^{-4} mM). These results indicate H_2SO_4 oxidation is negligible during the OER process on Co_2MnO_4. Furthermore, we have added a discussion section in Supplementary Note 3 to deny the possibility of H_2SO_4 oxidation during electrolysis.

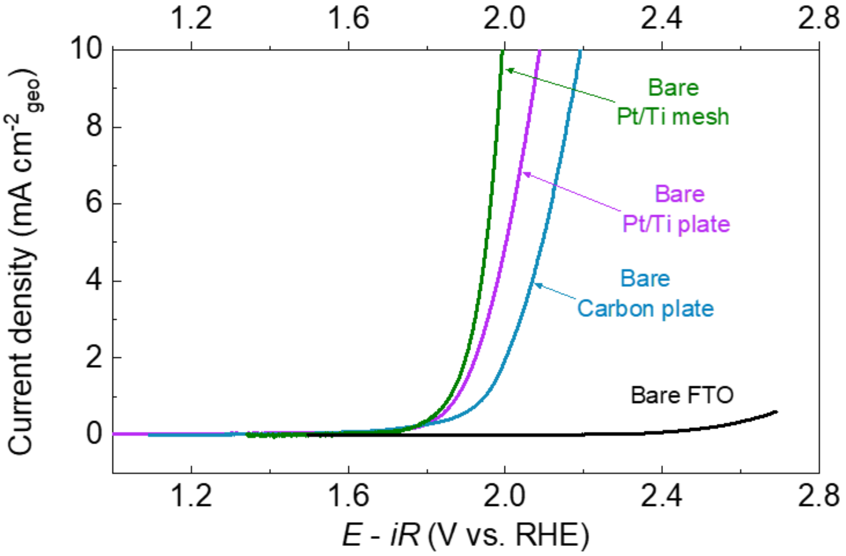

Supplementary Figure 19. LSVs of FTO, carbon plate, Pt/Ti plate and Pt/Ti mesh. Linear sweep voltammograms (LSVs) of bare FTO substrate, bare carbon plate, bare Pt/Ti plate and bare Pt/Ti mesh in H_2SO_4 (pH 0) at 25 °C after *iR* correction. Scan rate, 10 mV s^{-1}.

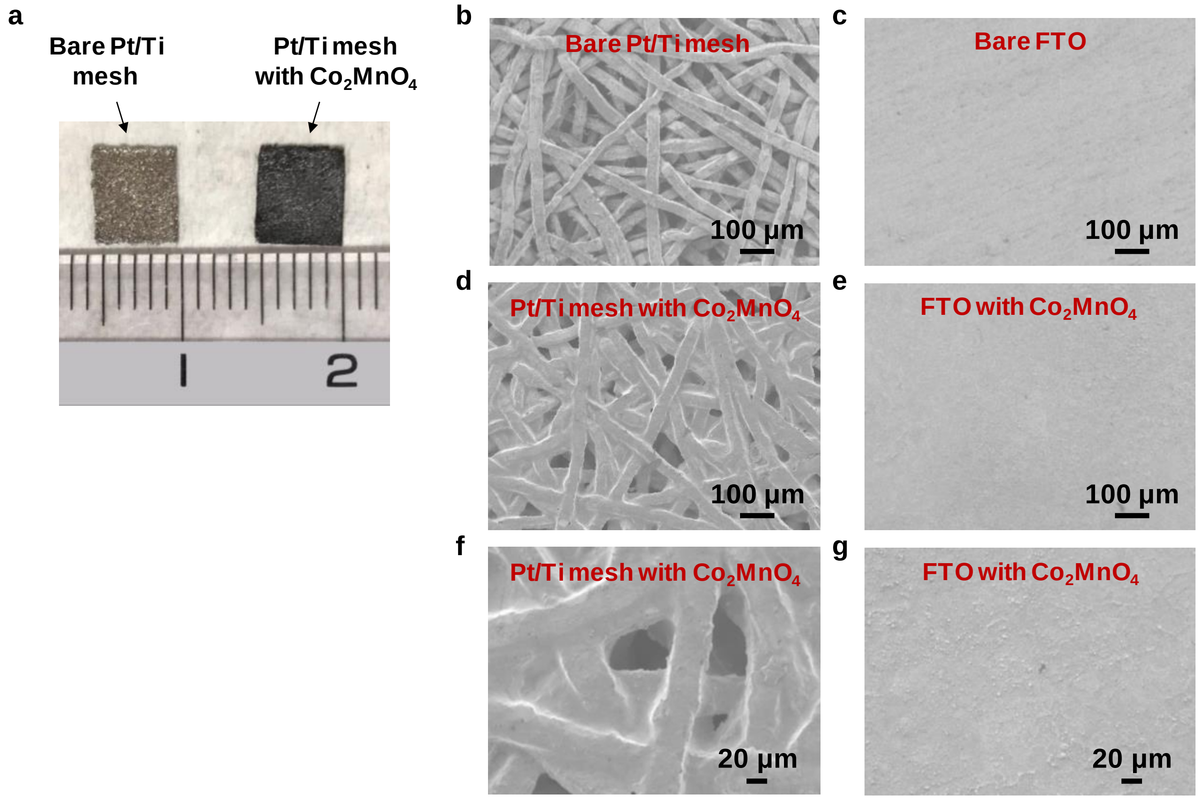

Supplementary Figure 20. Images of electrodes with Co_2MnO_4 on FTO and Pt/Ti mesh. **a,** Photos of the Pt/Ti mesh before and after deposition of Co_2MnO_4. The SEM images of Pt/Ti mesh and FTO, before and after deposition of Co_2MnO_4 are shown in panels (**b**) to (**g**). The bare substrates are shown in (**b**) and (**c**). The images after deposition of Co_2MnO_4 are shown in (**d**) and (**e**). Magnified images are shown in (**f**) and (**g**). Scale bars are shown in the figures. The electrochemical surface area (ECSA)[12] of Co_2MnO_4 on Pt/Ti mesh was measured to be 8-10 times higher than that of Co_2MnO_4 on FTO substrate per geometric area (Supplementary Figs. 21 and 22).

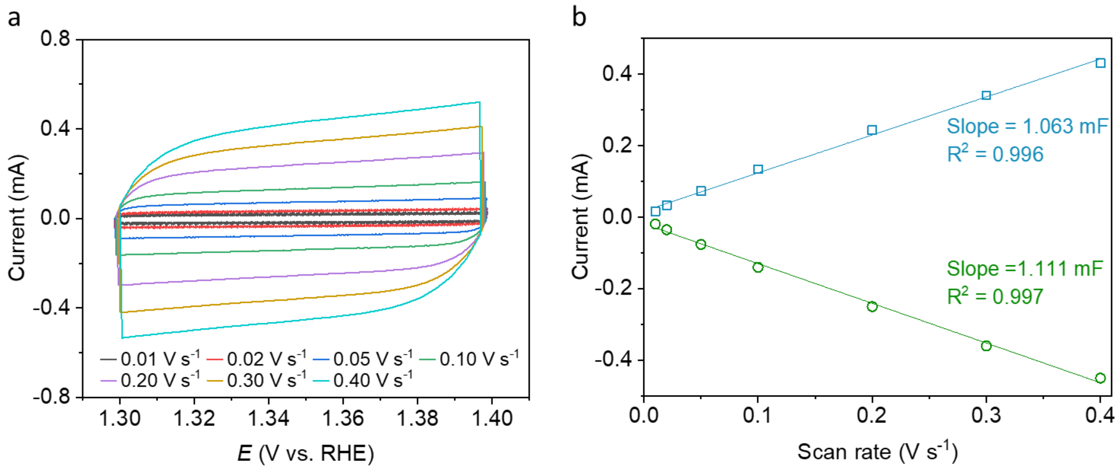

Supplementary Figure 21. ECSA measurement of Co_2MnO_4 on FTO. Double-layer capacitance measurements for determining the electrochemical surface area (ECSA)[12] of Co_2MnO_4 deposited on FTO in pH 0 H_2SO_4 at 25 °C. **a,** Cyclic voltammograms were measured in a non-Faradaic region of the voltammogram at the following scan rates: 0.01, 0.02, 0.05, 0.10, 0.20, 0.30, and 0.40 V s^{-1}. The working electrode was held at each potential vertex for 10 s before beginning the next sweep. All currents were assumed to be due to capacitive charging. **b,** The cathodic and anodic charging currents measured at 1.35 V vs. RHE plotted as a function of scan rate. The potentials have not been *iR* corrected due to the low currents of the ECSA measurements. The double-layer capacitance of the system is taken as the average of the absolute value of the slope of the linear fits to the data. The ECSA of the catalyst can be calculated by dividing double layer by the specific capacitance of Co (0.035 mF cm^{-2})[12].

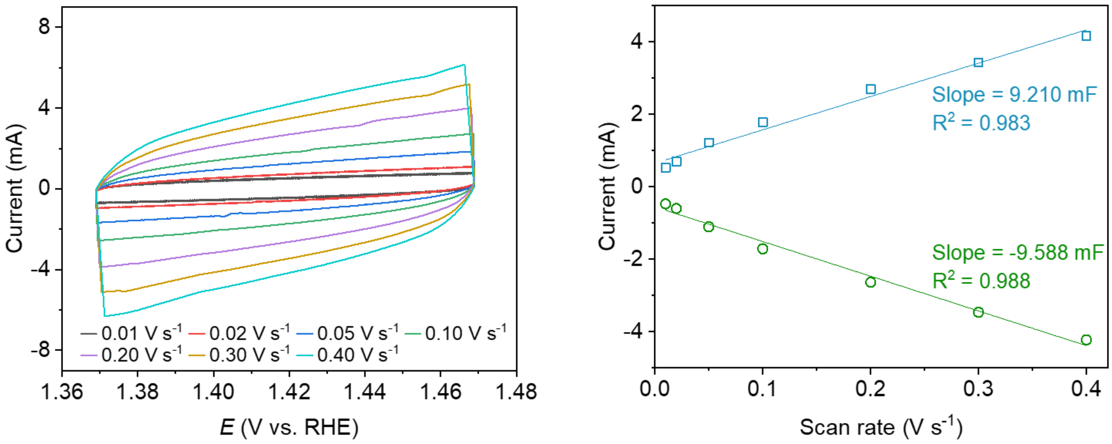

Supplementary Figure 22. ECSA measurement of Co_2MnO_4 on Pt/Ti mesh. Double-layer capacitance measurements for determining the ECSA[12] of Co_2MnO_4 deposited on Pt/Ti mesh in pH 0 H_2SO_4 at 25 °C. **a,** Cyclic voltammograms were measured in a non-Faradaic region of the voltammogram at the following scan rate: 0.01, 0.02, 0.05, 0.10, 0.20, 0.30, and 0.40 V s^{-1}. The working electrode was held at each potential vertex for 10 s before beginning the next sweep. All currents were assumed to be due to capacitive charging. **b,** The cathodic and anodic charging currents measured at 1.42 V vs. RHE plotted as a function of scan rate. The potentials have not been *iR* corrected due to the low currents of the ECSA measurements. The double-layer capacitance of the system is taken as the average of the absolute value of the slope of the linear fits to the data. The ECSA of the catalyst can be calculated by dividing double layer by the specific capacitance of Co (0.035 mF cm^{-2})[12].

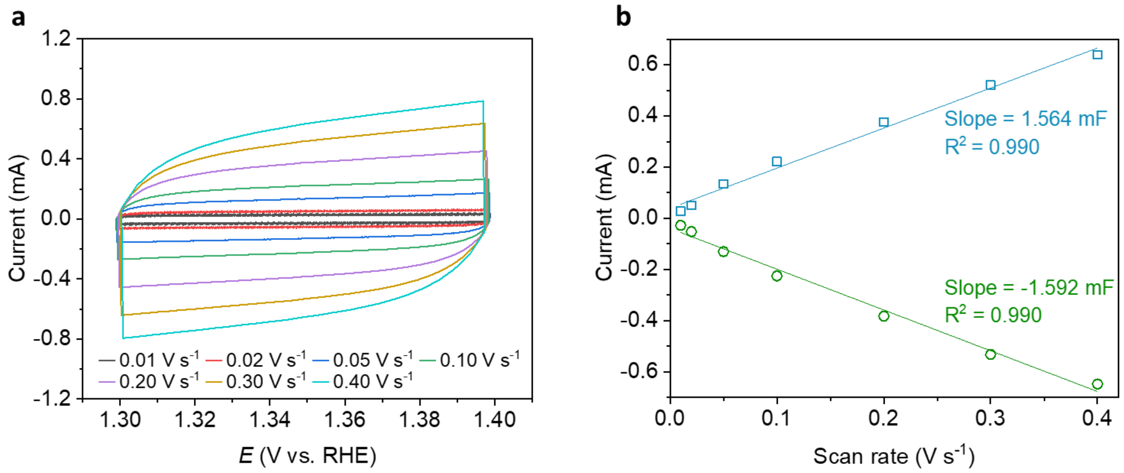

Supplementary Figure 23. ECSA measurement of Co_2MnO_4 on carbon plate. Double-layer capacitance measurements for determining the ECSA[12] of Co_2MnO_4 deposited on carbon plate in pH 0 H_2SO_4 at 25 °C. **a,** Cyclic voltammograms were measured in a non-Faradaic region of the voltammogram at the following scan rate: 0.01, 0.02, 0.05, 0.10, 0.20, 0.30, and 0.40 V s^{-1}. The working electrode was held at each potential vertex for 10 s before beginning the next sweep. All currents were assumed to be due to capacitive charging. **b,** The cathodic and anodic charging currents measured at 1.35 V vs. RHE plotted as a function of scan rate. The potentials have not been *iR* corrected due to the low currents of the ECSA measurements. The double-layer capacitance of the system is taken as the average of the absolute value of the slope of the linear fits to the data. The ECSA of the catalyst can be calculated by dividing double layer by the specific capacitance of Co (0.035 mF cm^{-2})[12].

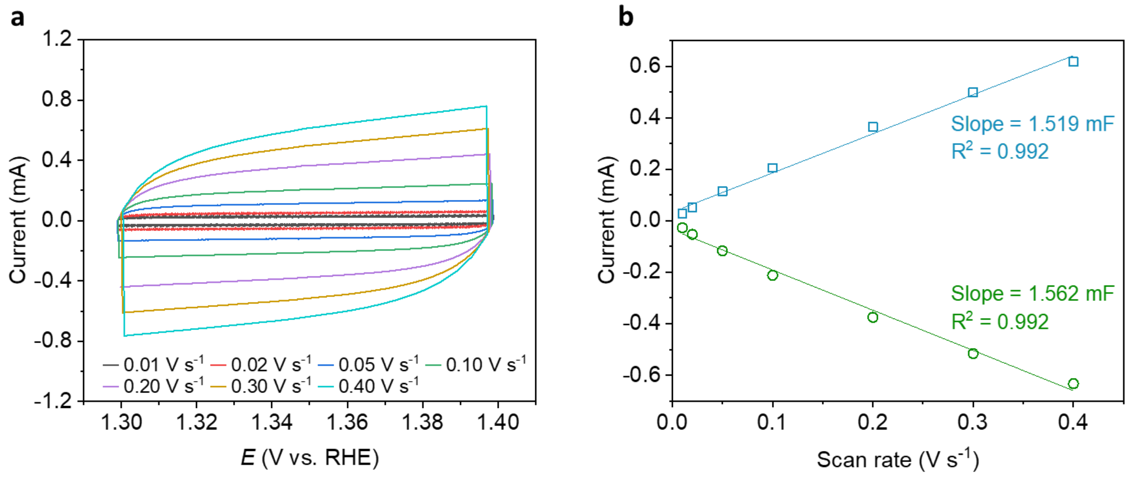

Supplementary Figure 24. ECSA measurement of Co_2MnO_4 on Pt/Ti plate. Double-layer capacitance measurements for determining the ECSA[12] of Co_2MnO_4 deposited on Pt/Ti plate in pH 0 H_2SO_4 at 25 °C. **a,** Cyclic voltammograms were measured in a non-Faradaic region of the voltammogram at the following scan rate: 0.01, 0.02, 0.05, 0.10, 0.20, 0.30, and 0.40 V s^{-1}. The working electrode was held at each potential vertex for 10 s before beginning the next sweep. All currents are assumed to be due to capacitive charging. **b,** The cathodic and anodic charging currents measured at 1.35 V vs. RHE plotted as a function of scan rate. The potentials have not been *iR* corrected due to the low currents of the ECSA measurements. The double-layer capacitance of the system is taken as the average of the absolute value of the slope of the linear fits to the data. The ECSA of the catalyst can be calculated by dividing double layer by the specific capacitance of Co (0.035 mF cm^{-2})[12].

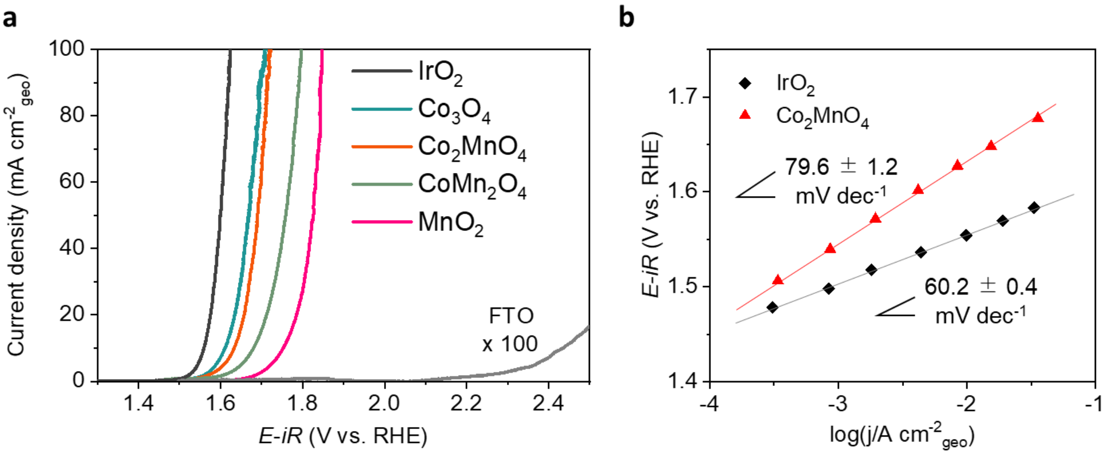

Supplementary Figure 25. LSVs of Co_3O_4, Co_2MnO_4, $CoMn_2O_4$, γ-MnO_2 and IrO_2. a, Linear sweep voltammograms of Co_3O_4, Co_2MnO_4, $CoMn_2O_4$, γ-MnO_2 and IrO_2 (Elyst Ir75 0480, metal purity 99.95%) deposited on FTO in pH 0 H_2SO_4 at 25 °C. Geometric area, 0.28 cm^2. Inset is the linear sweep voltammogram of a bare FTO substrate, magnified by 100 times. **b,** Tafel plots of Co_2MnO_4 and IrO_2. Geometric area, 0.28 cm^2.

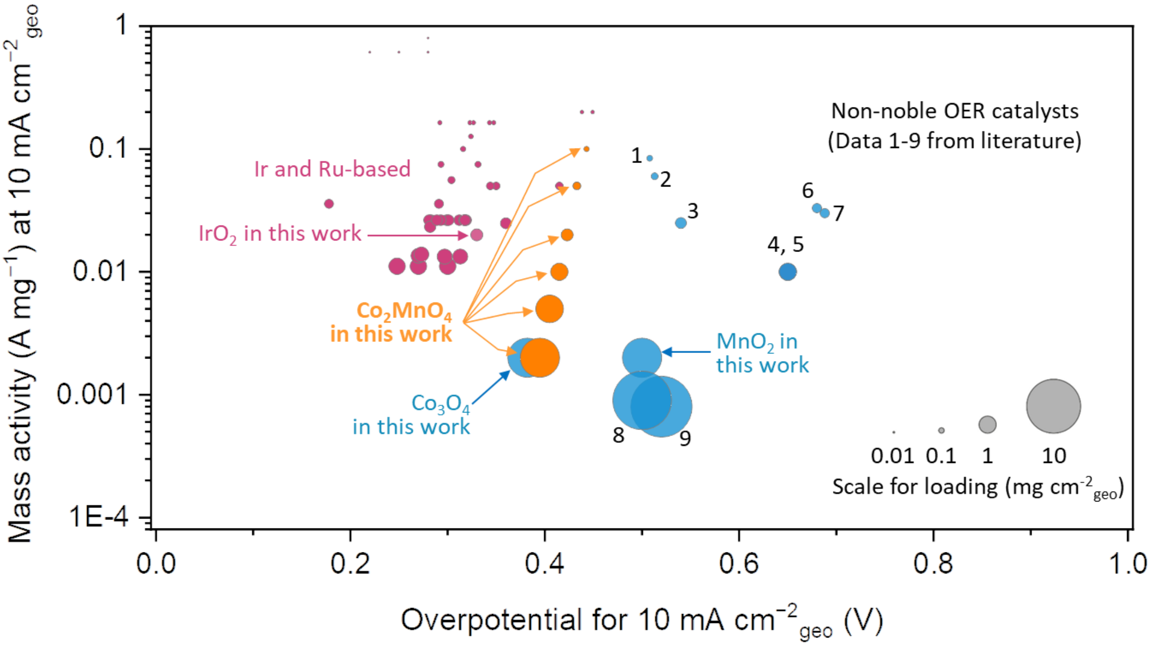

Supplementary Figure 26. Comparisons of overpotential and mass activity with literature. The overpotential and the mass activity at 10 mA cm$^{-2}_{geo}$ in acid for Co_2MnO_4 on FTO (orange), Ir- and Ru-based catalysts (pink), and non-noble OER catalysts in the literature (blue). The figure has been adapted from *Nat. Energy 2019, 4, 430*. (ref. [13]). The areas of the data points are proportional to the mass loading per cm$^{2}_{geo}$. Electrodes with Co_3O_4, γ-MnO_2, and IrO_2 (Elyst Ir75 0480, metal purity 99.95%) prepared in this work were also compared here. For the numerical data and additional material information, see Supplementary Table 15 (Ir- and Ru-based OER catalysts) and Supplementary Table 16 (non-noble OER catalysts).

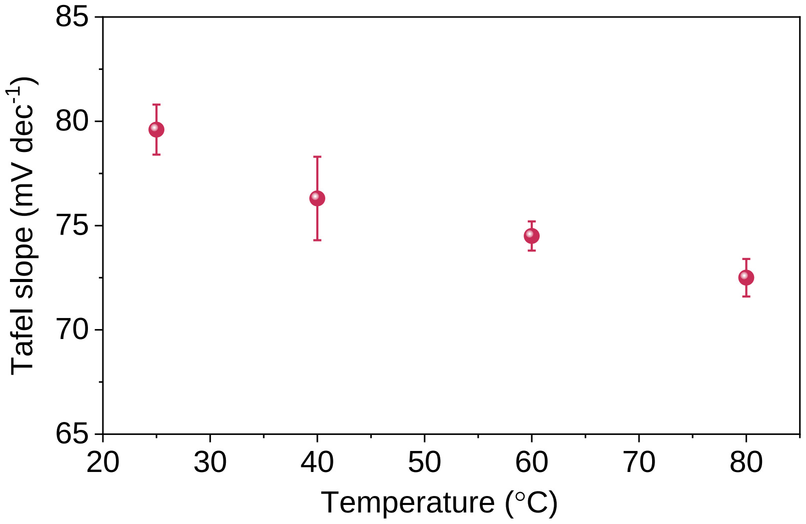

Supplementary Figure 27. Tafel slopes of Co_2MnO_4 deposited on FTO. Tafel slopes of Co_2MnO_4 deposited on FTO, measured by chronopotentiometry in H_2SO_4 (pH 0) at temperatures of 25, 40, 60, and 80 °C. Error bars indicate the standard deviation from four separate experiments.

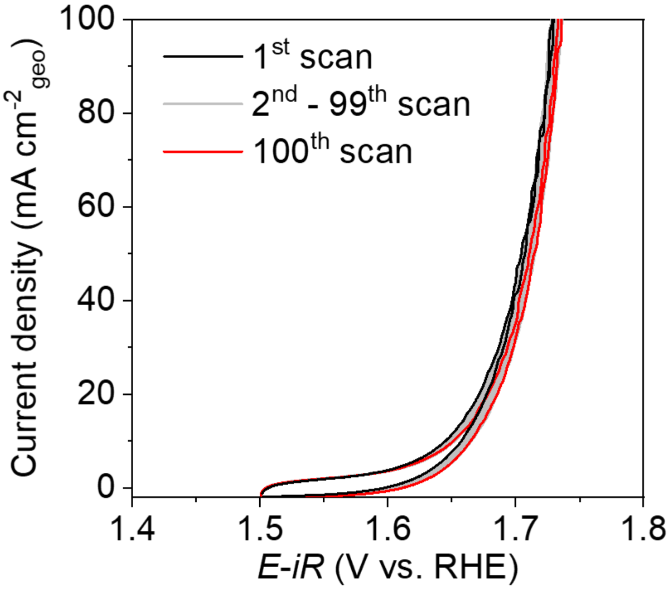

Supplementary Figure 28. Cyclic voltammogram of Co_2MnO_4 on FTO. The scan rate was 2 mV s^{-1} and the potential range was 1.50 - 1.74 V vs. RHE after *iR* correction in H_2SO_4 (pH 0) at 25 °C.

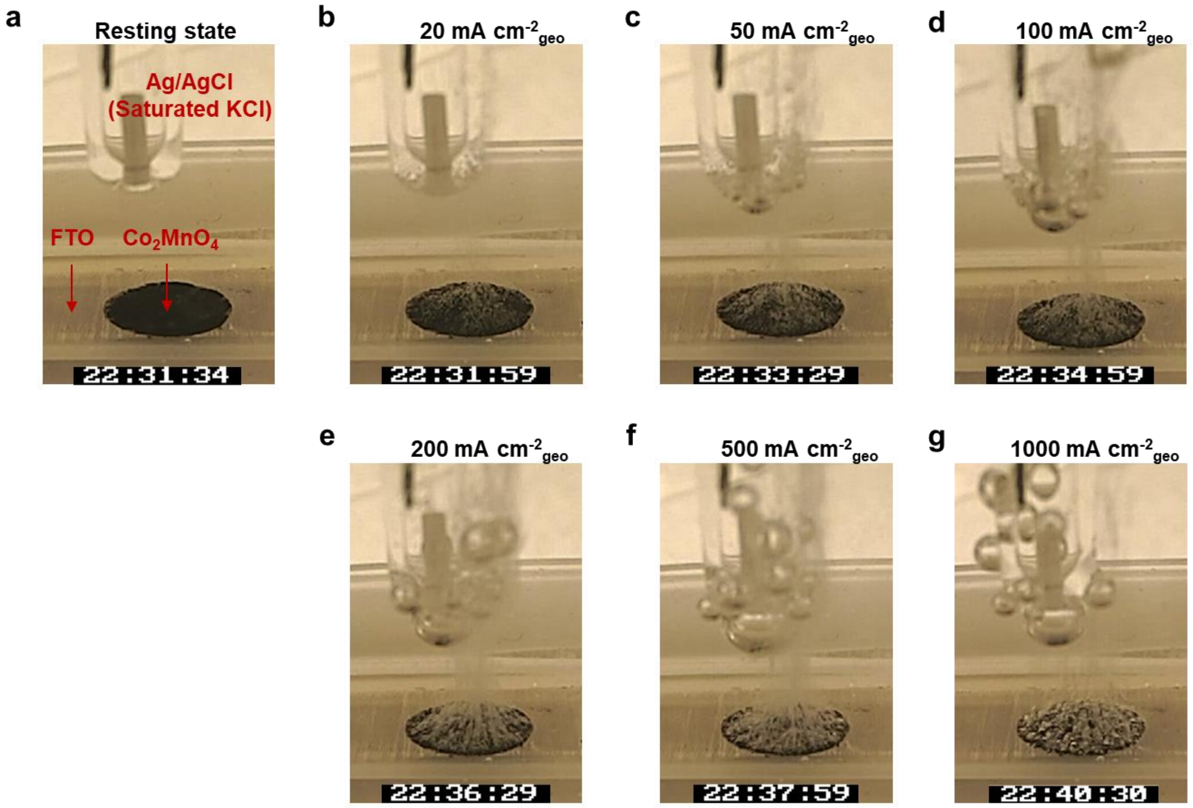

Supplementary Figure 29. Photos of bubble generation on the Co_2MnO_4 electrode. Photos of the Co_2MnO_4 electrode on FTO during OER in H_2SO_4 (pH 0) at 25 °C, showing the gas-bubble generation at the resting state (**a**) and after applying current densities of (**b**) 20 mA cm$^{-2}{}_{geo}$, (**c**) 50 mA cm$^{-2}{}_{geo}$, (**d**) 100 mA cm$^{-2}{}_{geo}$, (**e**) 200 mA cm$^{-2}{}_{geo}$, (**f**) 500 mA cm$^{-2}{}_{geo}$, and (**g**) 1000 mA cm$^{-2}{}_{geo}$.

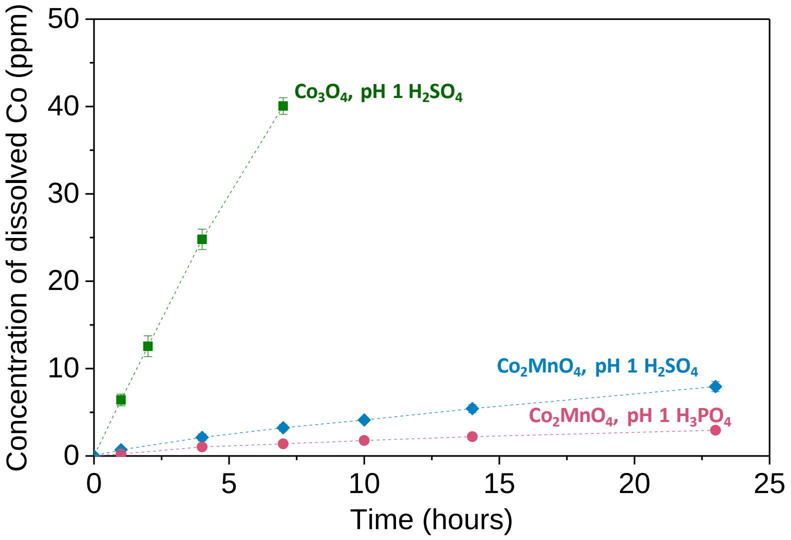

Supplementary Figure 30. Time dependence of Co dissolution. Time dependence of Co dissolution during chronopotentiometric (CP) experiments on Co_3O_4 and Co_2MnO_4 at 100 mA cm^{-2}_{geo}. FTO was used as the substrate. The dissolution rate of Co_2MnO_4 is 10 times lower when compared to that of Co_3O_4 in pH 1 H_2SO_4 at 25 °C. Changing the electrolyte to pH 1 H_3PO_4 further decreases the dissolution rate by over 60%. The stability number[14] (S-number) was calculated to be 70, 3600 and 16000 (n_{oxygen}/n_{cobalt}) for Co_3O_4 (pH 1 H_2SO_4, 100 mA cm^{-2}_{geo} for 7 hours), Co_2MnO_4 (pH 1 H_2SO_4, 100 mA cm^{-2}_{geo} for 330 hours) and Co_2MnO_4 (pH 1 H_3PO_4, 100 mA cm^{-2}_{geo} for 1400 hours), respectively. The difference in electrolyte must also be considered, as phosphate is well known to suppress Co dissolution[15]. Using ICP-MS, we observe Co leaching is 60 % slower in phosphate compared to sulfate, which leads to a discrepancy in the lifetime depending on the electrolysis condition.

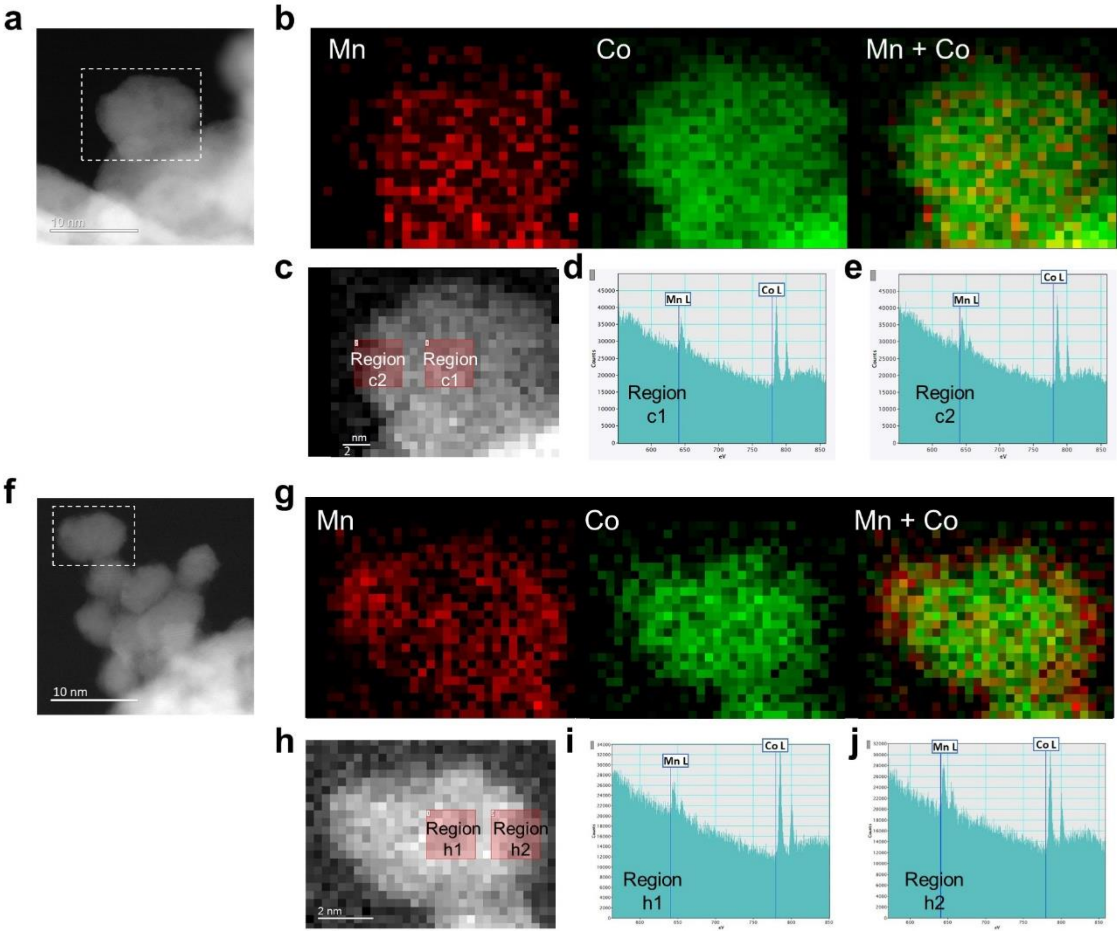

Supplementary Figure 31. STEM-EELS analysis of Co_2MnO_4 before and after electrolysis at 100 mA cm^{-2}_{geo} for 23 hours in H_2SO_4 (pH 1) at 25 °C. STEM-EELS elementary analysis of Co_2MnO_4 before (**a-e**) and after (**f-j**) electrolysis at 100 mA cm^{-2}_{geo} for 23 hours in H_2SO_4 (pH 1) at 25 °C. (**a**) and (**f**) show the High-Angle Annular Dark Field Scanning (HAADF)-STEM images. The region surrounded by the dashed lines were used for the EELS elementary mapping in (**b**) and (**g**). Mn and Co are shown in red and green, respectively, for all images. EELS spectra of Mn L-edge and Co L-edge for the sample before and after electrolysis were shown in (**c, d, e**) and (**h, i, j**), respectively. The spectra were taken from the core and surface regions of nanoparticles (region **c1, c2** and region **h1, h2**). Elemental mapping of the as-synthesized Co_2MnO_4 nanoparticles showed that Co and Mn are uniformly distributed. The Co/Mn ratios estimated by Mn L-edge and Co L-edge spectra were 2.0:1 in both the core (region **c1**) and near surface (region **c2**) regions of the nanoparticle (error estimated from spectral signal is 5~10 %). After electrolysis however, the distribution of Co and Mn in the nanoparticles became less uniform, due to the formation of Mn-rich regions near the surface. Namely, the Co/Mn ratio in the core part of the nanoparticles (region **f1**) is 1.9:1, while it is 1.5:1 in the region closer to the surfaces (region **f2**). The formation of Mn-rich regions at the surface is consistent with our ICP and DFT calculations, showing that Co is dissolved preferentially compared to Mn.

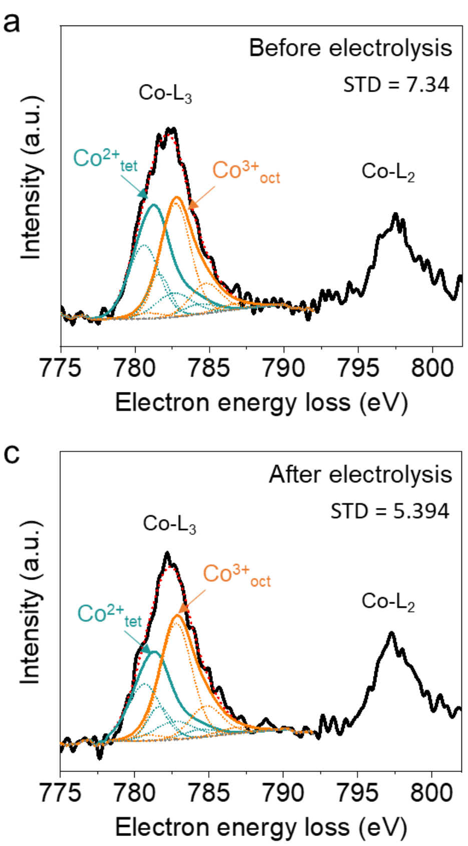

b

No	Name	Position	FWHM	Line shape	%At
1	Co$^{2+}_{tet}$-Peak 1	780.65	2.40	GL(30)	25.78
2	Co$^{2+}_{tet}$-Peak 2	781.65	1.72	GL(30)	11.08
3	Co$^{2+}_{tet}$-Peak 3	782.65	2.81	GL(30)	9.79
4	Co$^{2+}_{tet}$-Peak 4	784.35	2.63	GL(30)	3.87
5	Co$^{3+}_{oct}$-Peak 1	780.88	2.36	GL(30)	1.80
6	Co$^{3+}_{oct}$-Peak 2	782.78	2.30	GL(30)	35.82
7	Co$^{3+}_{oct}$-Peak 3	784.79	2.38	GL(30)	9.77
8	Co$^{3+}_{oct}$-Peak 4	786.81	2.63	GL(30)	2.09

d

No	Name	Position	FWHM	Line shape	%At
1	Co$^{2+}_{tet}$-Peak 1	780.65	2.59	GL(30)	21.37
2	Co$^{2+}_{tet}$-Peak 2	781.65	1.85	GL(30)	9.19
3	Co$^{2+}_{tet}$-Peak 3	782.65	3.03	GL(30)	8.12
4	Co$^{2+}_{tet}$-Peak 4	784.35	2.84	GL(30)	3.21
5	Co$^{3+}_{oct}$-Peak 1	780.88	2.54	GL(30)	2.11
6	Co$^{3+}_{oct}$-Peak 2	782.78	2.48	GL(30)	42.07
7	Co$^{3+}_{oct}$-Peak 3	784.79	2.57	GL(30)	11.48
8	Co$^{3+}_{oct}$-Peak 4	786.81	2.84	GL(30)	2.46

Supplementary Figure 32. Co L$_3$ edge fitting before and after electrolysis. Co L$_3$ edge fitting in the edge regions of Co_2MnO_4 before (a, b) and after electrolysis at 100 mA cm$^{-2}_{geo}$ for 23 hours (c, d). The spectra were fitted by considering tetrahedral Co^{2+} (Co$^{2+}_{tet}$) and octahedral Co^{3+} (Co$^{3+}_{oct}$), reproduced from the literature[16]. The full width at half maximum (FWHM) was not fixed, although other parameters such as peak position and line ships were fixed during the spectra fitting.

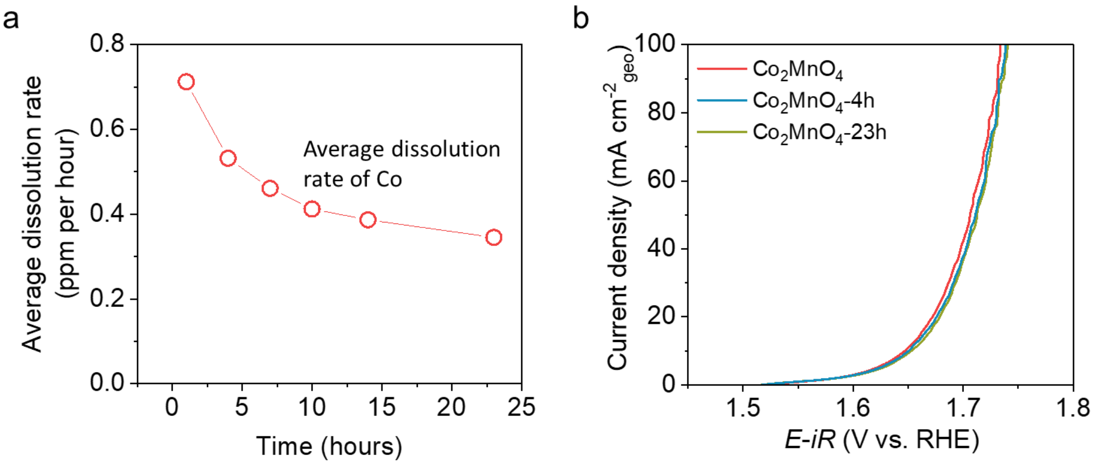

Supplementary Figure 33. LSVs of Co_2MnO_4 after electrolysis for 4 hours and 23 hours. **a,** Dissolution rate of Co during CP experiments on Co_2MnO_4 at 100 mA cm^{-2}_{geo}. The average dissolution rate is calculated by dividing the total dissolution by the operation time in Supplementary Fig. 30. **b,** Linear sweep voltammograms of Co_2MnO_4 deposited on FTO before (red) and after electrolysis (blue, green) in H_2SO_4 (pH 0) at 25 °C. Geometric area, 0.28 cm^2. Electrolysis was conducted in H_2SO_4 (pH 0) at 25 °C for 4 hours (blue) and 23 hours (green).

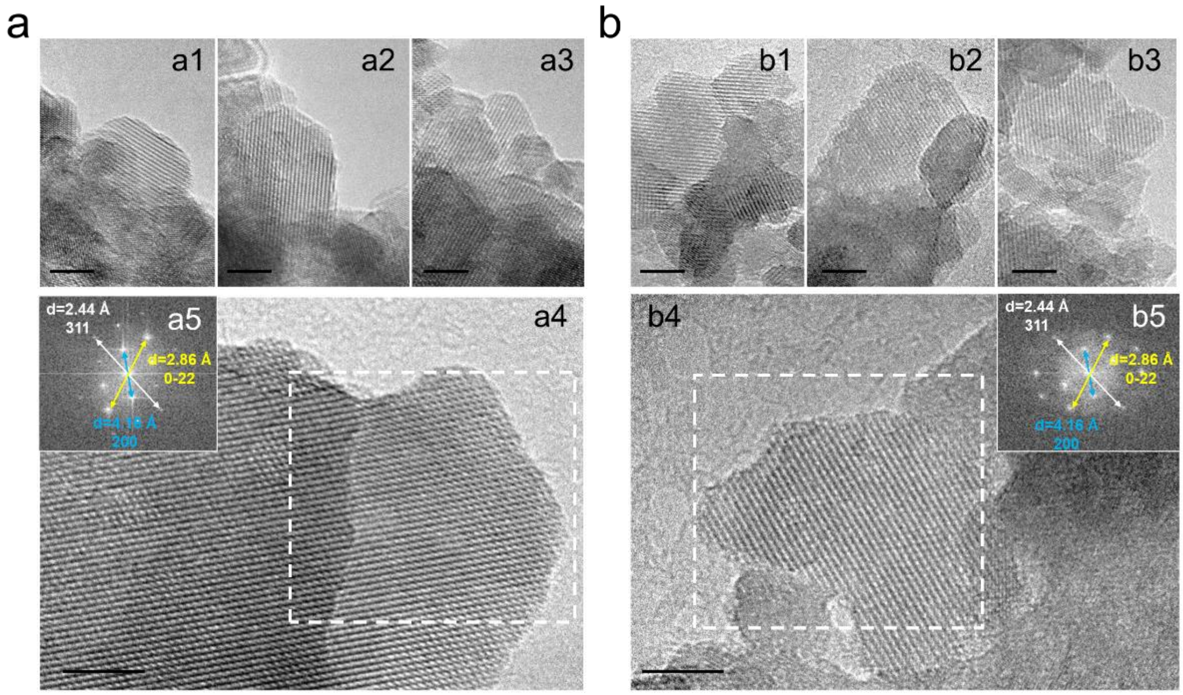

Supplementary Figure 34. HRTEM images of Co$_2$MnO$_4$ before and after electrolysis at 100 mA cm$^{-2}_{geo}$ for 23 hours in H$_2$SO$_4$ (pH 1) at 25 °C. HRTEM images of Co$_2$MnO$_4$ before (**a**) and after electrolysis at 100 mA cm$^{-2}_{geo}$ for 23 hours in H$_2$SO$_4$ (pH 1) at 25 °C (**b**). Multiple images are presented, with low (**a1-3** and **b1-3**) and high (**a4** and **b4**) magnifications. Scale bar, 5 nm. The FFT patterns shown in (**a5** and **b5**) were obtained from the framed area in **a4** and **b4**. There was no clear change in the surface structures of the nanoparticles, confirming that neither amorphization nor new crystalline phase formation proceeds at the catalyst surface during electrolysis. Namely, the continuous lattice fringes extending through the whole nanoparticles were maintained even after electrolysis. Additionally, the lattice spacing of 4.16 Å, 2.86 Å and 2.44 Å, which corresponds to the (200), (220) and (311) planes of spinel-type Co$_2$MnO$_4$, respectively, were also retained after electrolysis.

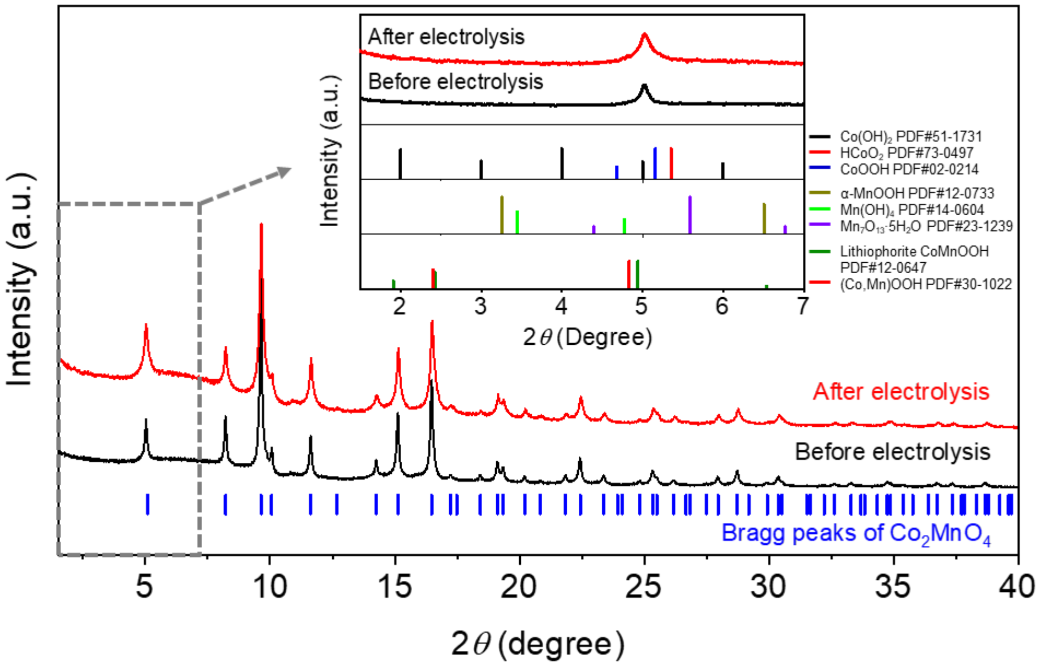

Supplementary Figure 35. SR-PXRD patterns of Co_2MnO_4 before and after electrolysis. SR-PXRD patterns of Co_2MnO_4 before and after electrolysis at 100 mA cm^{-2}_{geo} for 23 hours in pH 1 H_2SO_4 at 25 °C, corresponding Rietveld refinement results are shown in Supplementary Figs. 1 and 3, respectively. The SR-PXRD patterns between 1.5 - 7° are enlarged in the inset. Bragg peaks of Co_2MnO_4 and the powder diffraction file (PDF) cards for representative Co- and Mn- based (oxy)hydroxides are also presented for comparison.

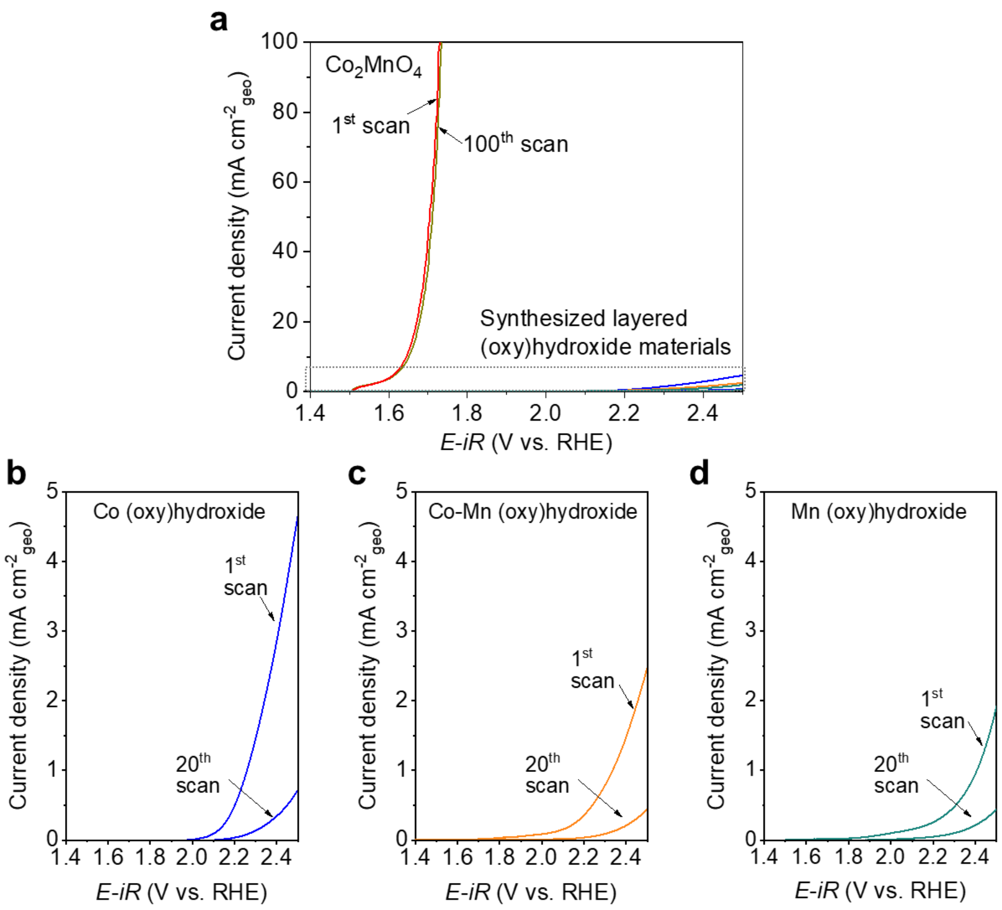

Supplementary Figure 36. OER performance of (oxy)hydroxides in acid. a, LSVs showing the activity and stability of Co_2MnO_4, cobalt (oxy)hydroxides, manganese (oxy)hydroxides and cobalt-manganese (oxy)hydroxides deposited on FTO in pH 0 H_2SO_4 at 25 °C. The LSVs of (oxy)hydroxides materials are enlarged in (**b, c, d**). The (oxy)hydroxides materials were electrodeposited on FTO based on the previously reported procedures[17,18]. The Pourbaix diagram shows that Co/Mn oxyhydroxides are stable under alkaline conditions, but unstable under strong acidic conditions, and therefore, their formation during our electrolysis experiments in acid is unlikely. Therefore, we believe that the spinel-type Co_2MnO_4 is the actual catalyst, and not a pre-catalyst for the formation of layered oxyhydroxides.

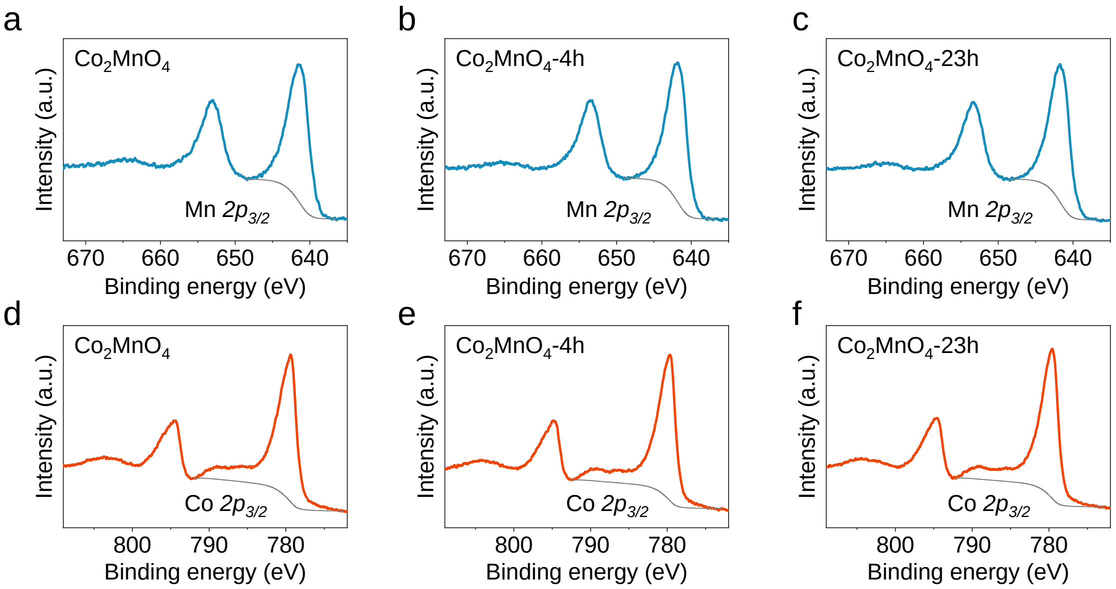

g

Samples	Peak Area of Co $2p_{3/2}$	Sensitivity factor of Co $2p_{3/2}$	Peak area of Mn $2p_{3/2}$	Sensitivity factor of Mn $2p_{3/2}$	Co:Mn atomic ratio
Co_2MnO_4	498.75	2.5	166.40	1.7	2.04:1
Co_2MnO_4-4h	554.50	2.5	206.95	1.7	1.82: 1
Co_2MnO_4-23h	579.35	2.5	224.70	1.7	1.75: 1

Supplementary Figure 37. XPS quantitative analysis of Co_2MnO_4 before and after electrolysis. XPS spectra of Mn*2p* (**a-c**) and Co*2p* (**d-f**) in Co_2MnO_4 before electrolysis (Co_2MnO_4) and Co_2MnO_4 after electrolysis at 100 mA cm^{-2}_{geo} for 4 hours (Co_2MnO_4-4h) and 23 hours (Co_2MnO_4-23h). (pH 1 H_2SO_4, 25 °C). The Co:Mn atom ratios determined by XPS were presented in (**g**), following the fitting procedure of Wagner et al.[19]. The ratio of Co:Mn on the surface was estimated to change from 2.04:1 to 1.75:1 during the first 23 hours of electrolysis at 100 mA cm^{-2}_{geo}. The decrease in the surface Co:Mn ratio is consistent with the ICP-MS measurements which indicate Co leaching, and implies the formation of a Mn-rich surface after electrolysis.

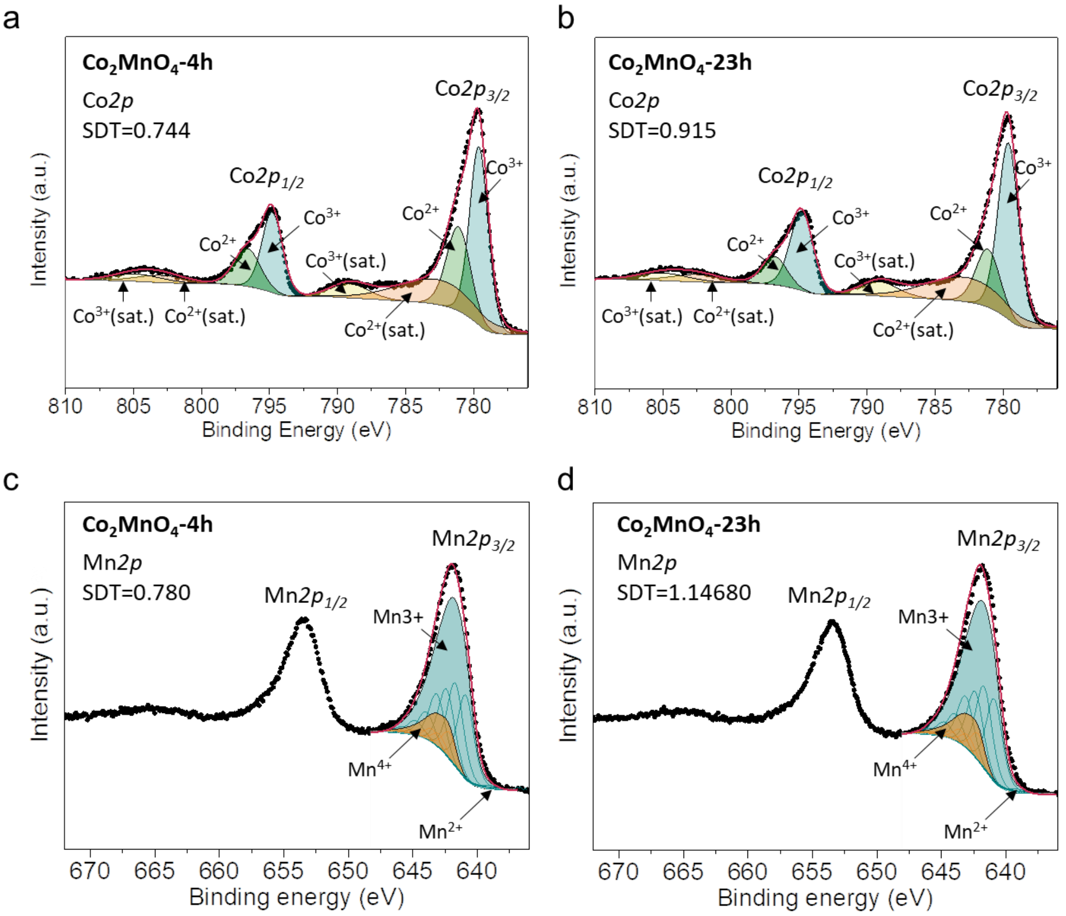

Supplementary Figure 38. XPS fitting of Co_2MnO_4 after electrolysis. XPS spectra fitting of Co*2p* (**a, b**) and Mn*2p* (**c, d**) in Co_2MnO_4 after electrolysis at 100 mA cm^{-2}_{geo} for 4 hours (Co_2MnO_4-4h) and 23 hours (Co_2MnO_4-23h). The spectra were fitted by considering Co^{2+} (refs.[5,6]), Co^{3+} (ref. [7]) and shakeup satellites for Co*2p*, and Mn^{2+}, Mn^{3+} and Mn^{4+} (ref.[8]) for Mn*2p*. All high-resolution spectra were collected using a pass energy of 23.5 eV and calibrated using the C*1s* peak at 284.6 eV. The spectral fitting parameters are presented in the Supplementary Tables 9 and 10 (Co*2p*), Supplementary Tables 12 and 13 (Mn*2p*).

Evaluation of Catalyst Lifetime

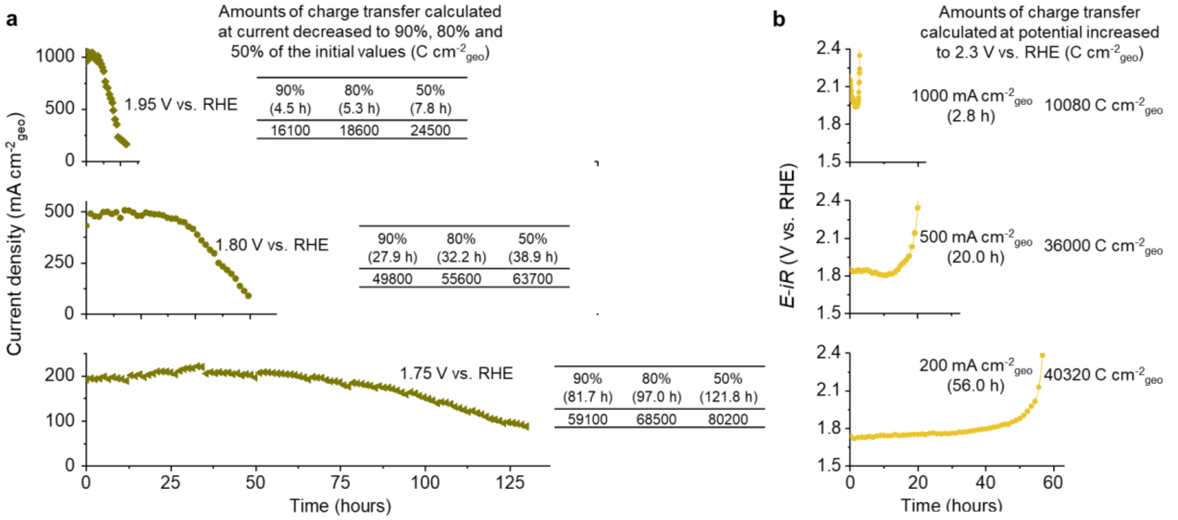

Supplementary Figure 39. CA measurements of Co_2MnO_4 on FTO. a, Chronoamperometry (CA) measurements of Co_2MnO_4 on FTO in H_2SO_4 (pH 1) at 25 °C. The applied potentials were 1.95 V, 1.80 V and 1.75 V vs. RHE after *iR* correction. The total amount of charge transferred at each potential was calculated when the current densities decreased to 90%, 80% and 50% of the initial values as shown in the inset. **b,** CP measurements of Co_2MnO_4 on FTO in H_2SO_4 (pH 1, at 25 °C) at 1000 mA cm^{-2}_{geo}, 500 mA cm^{-2}_{geo} and 200 mA cm^{-2}_{geo}. The total amount of charge transferred was calculated when the potential exceeded 2.3 V vs. RHE after *iR* correction.

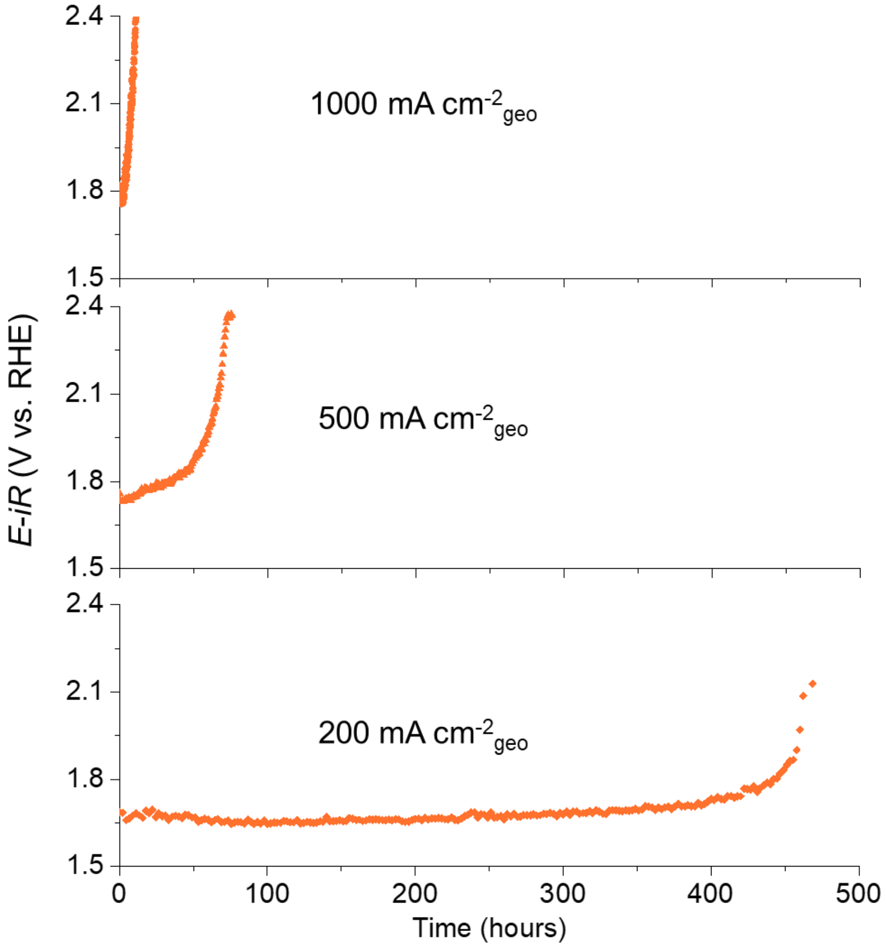

Supplementary Figure 40. CP measurements of Co_2MnO_4 on Pt/Ti mesh in H_2SO_4. CP measurements of Co_2MnO_4 on Pt/Ti mesh at current densities of 1000 mA cm^{-2}$_{geo}$, 500 mA cm^{-2}$_{geo}$ and 200 mA cm^{-2}$_{geo}$ in H_2SO_4 (pH 1, at 25 °C). Potentials are corrected for ohmic losses.

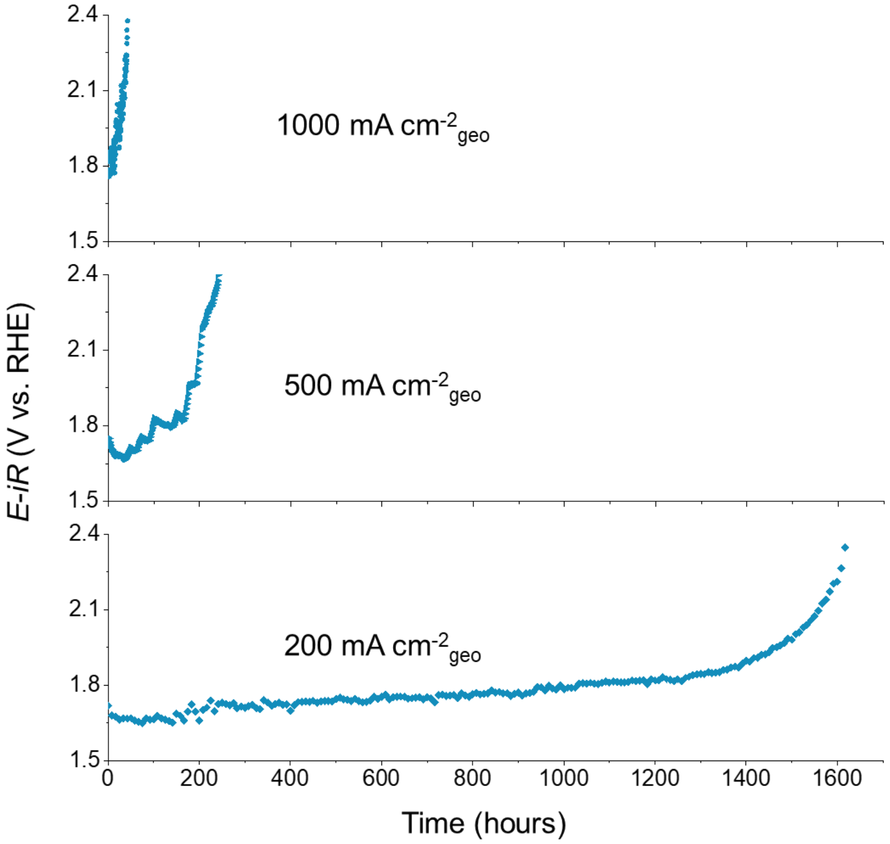

Supplementary Figure 41. CP measurements of Co_2MnO_4 on Pt/Ti mesh in H_3PO_4. CP measurements of Co_2MnO_4 on Pt/Ti mesh at current densities of 1000 mA cm$^{-2}_{geo}$, 500 mA cm$^{-2}_{geo}$ and 200 mA cm$^{-2}_{geo}$ in H_3PO_4 (pH 1, at 25 °C). Potentials have been corrected for ohmic losses.

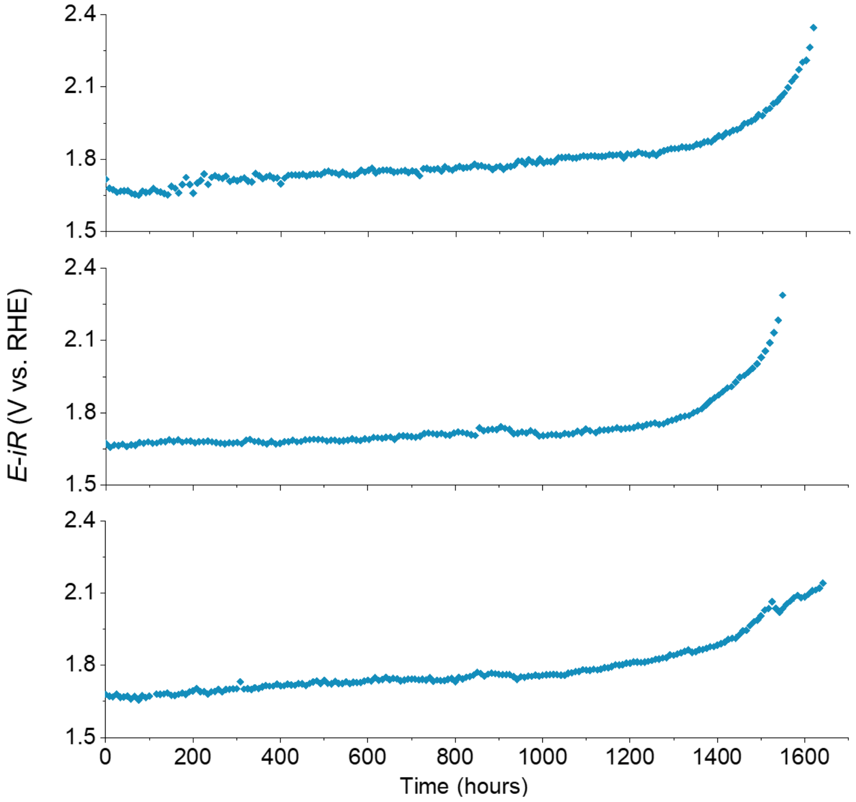

Supplementary Figure 42. Repeated CP measurements at 200 mA cm^{-2}$_{geo}$. Three individual CP measurements of Co_2MnO_4 on Pt/Ti mesh at 200 mA cm^{-2}$_{geo}$ in H_3PO_4 (pH 1, at 25 °C). All measurements indicate electrolysis can be performed for about 1500 hours, indicating high reproducibility. Potentials are corrected for ohmic losses.

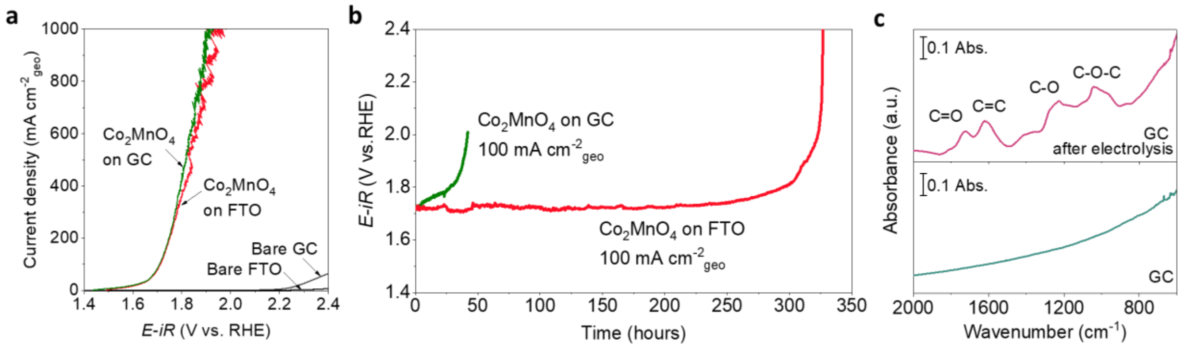

Supplementary Figure 43. OER comparison of Co_2MnO_4 on FTO and glassy carbon. LSVs of Co_2MnO_4 on glassy carbon (GC) and FTO, as well as bare glassy carbon and FTO after *iR* correction. The electrolyte was H_2SO_4 (pH 0) at 25 °C. Scan rate, 10 mV s^{-1}. **b,** The long-term stability of Co_2MnO_4 on glassy carbon and FTO at 100 mA cm^{-2}_{geo} in pH 1 H_2SO_4 at 25 °C. **c,** ATR-FTIR spectrum of glassy carbon before and after electrolysis at 1.7 V vs. RHE after *iR* correction for 1 hour. ATR-FTIR measurements were performed on PerkinElmer Spotlight 400 equipped with a liquid nitrogen-cooled MCT detector and an ATR accessory.

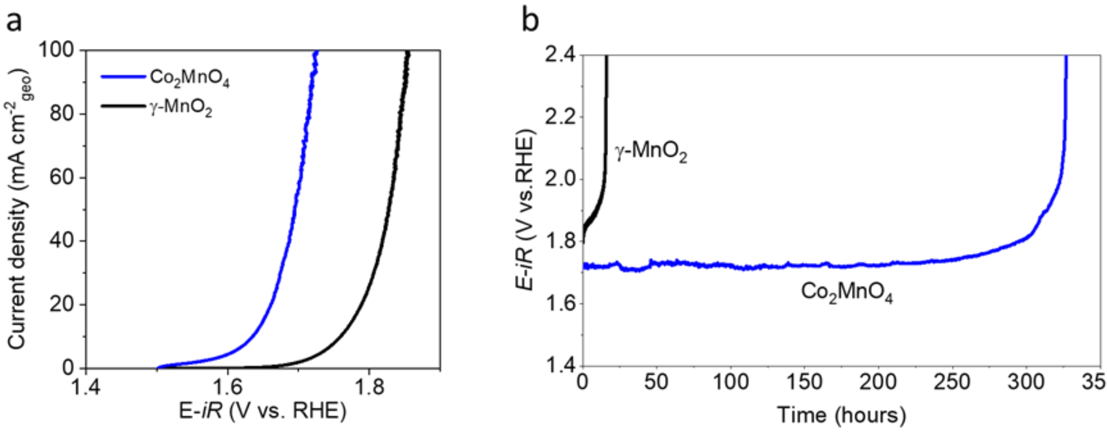

Supplementary Figure 44. OER comparison between Co_2MnO_4 and MnO_2. LSVs of Co_2MnO_4 and γ-MnO_2 on FTO with the same amount of Mn loading (2.3 mg_{Mn} cm^{-2}_{geo}) in pH 0 H_2SO_4 at 25 °C. **b,** The long-term stability of Co_2MnO_4 and γ-MnO_2 on FTO at 100 mA cm^{-2}_{geo} in pH 1 H_2SO_4 at 25 °C.

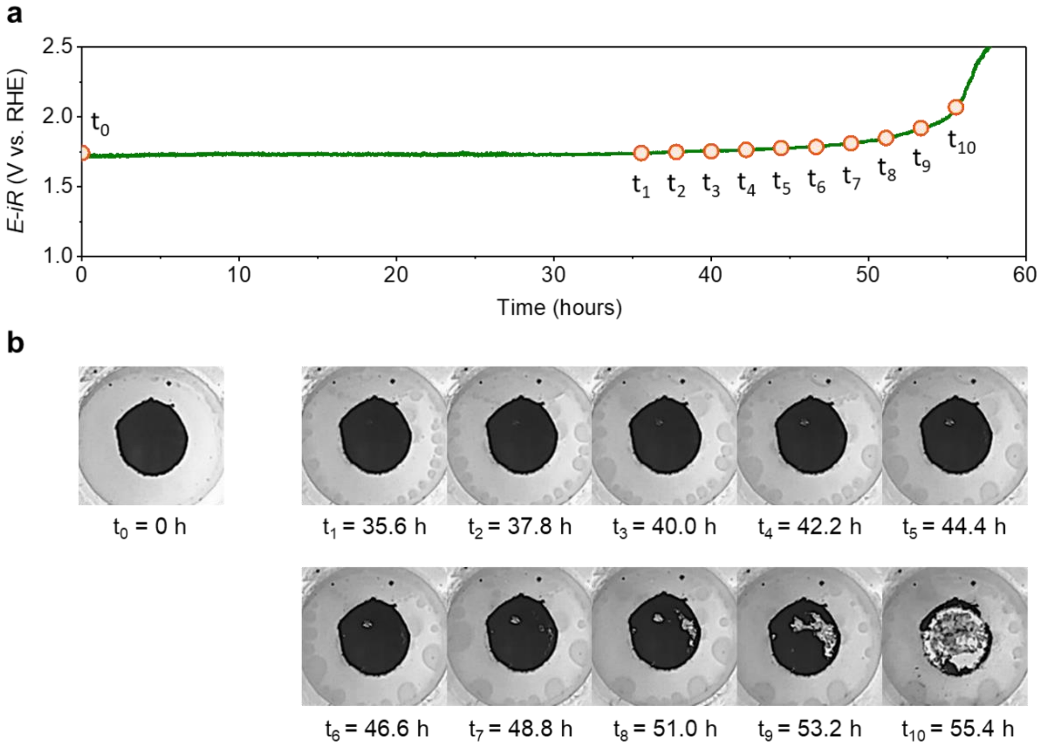

Supplementary Figure 45. Time course of catalyst detachment during electrolysis. a, Chronopotentiometry at 200 mA cm^{-2}_{geo} with Co_2MnO_4 on FTO substrate at 25 °C in pH 1 H_2SO_4. **b**, Photographs showing how the appearance of the electrode changes over time. Photographs were obtained at t_0 = 0 h, t_1 = 35.6 h, t_2 = 37.8 h, t_3 = 40.0 h, t_4 = 42.2 h, t_5 = 44.4 h, t_6 = 46.6 h, t_7 = 48.8 h, t_8 = 51.0 h, t_9 = 53.2 h and t_{10} = 55.4 h. The time stamps are the same as in (**a**), and show how large particles of the catalyst are detached from the surface with time.

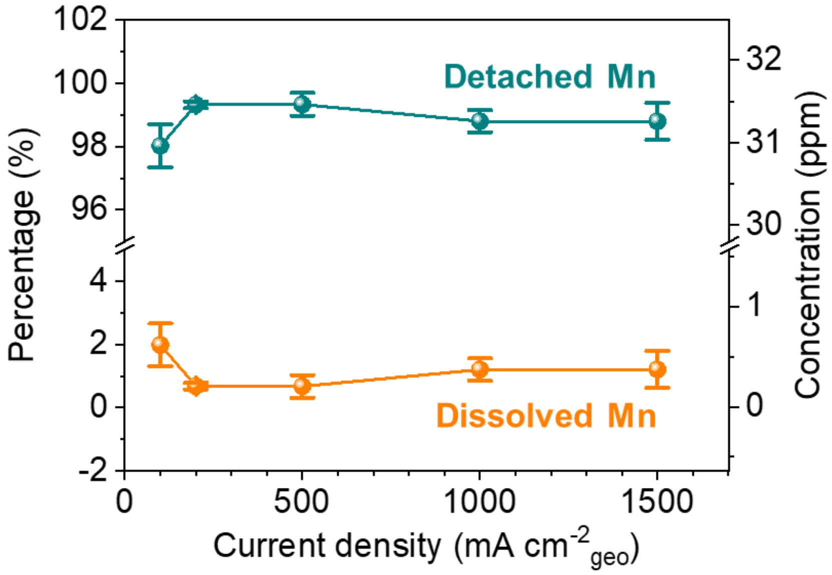

Supplementary Figure 46. ICP-MS quantification of Mn detachment and dissolution. The percentage (left Y-axis) and concentration (right Y-axis) of Mn which was detached in solid form or dissolved from the catalyst after electrolysis in H_2SO_4 (pH 1). The X axis indicates the current density at which electrolysis was performed, and quantification was performed using ICP-MS only after the catalyst was fully deactivated.

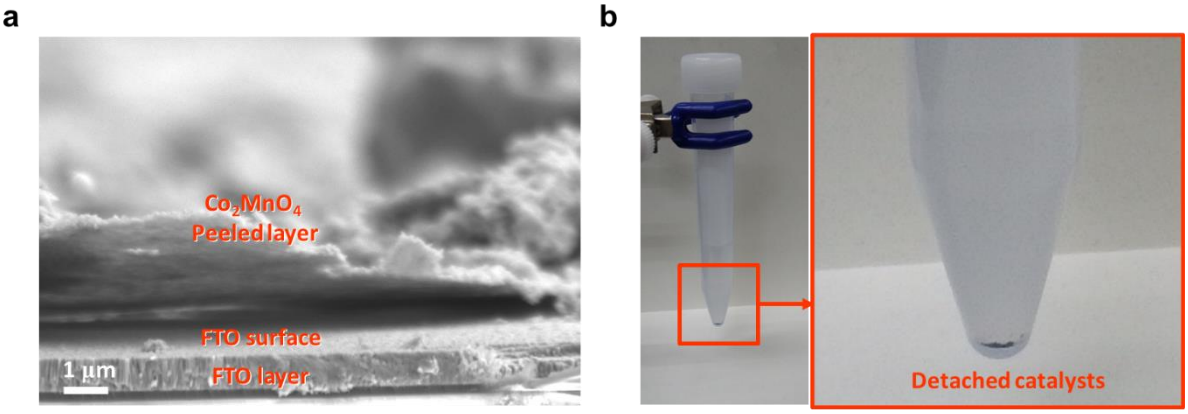

Supplementary Figure 47. SEM observation of catalyst detachment. a, Cross-sectional SEM image of the electrode on FTO after electrolysis at 200 mA $cm^{-2}{}_{geo}$ for 50 hours (pH 1 H_2SO_4, 25 °C). A large void between the surface of the FTO substrate and the Co_2MnO_4 can be observed, suggesting the catalyst is detached due to the mechanical stress. Scale bar, 1 µm. **b**, Catalyst particles released into the electrolyte after the same electrolysis conditions, collected by centrifugation.

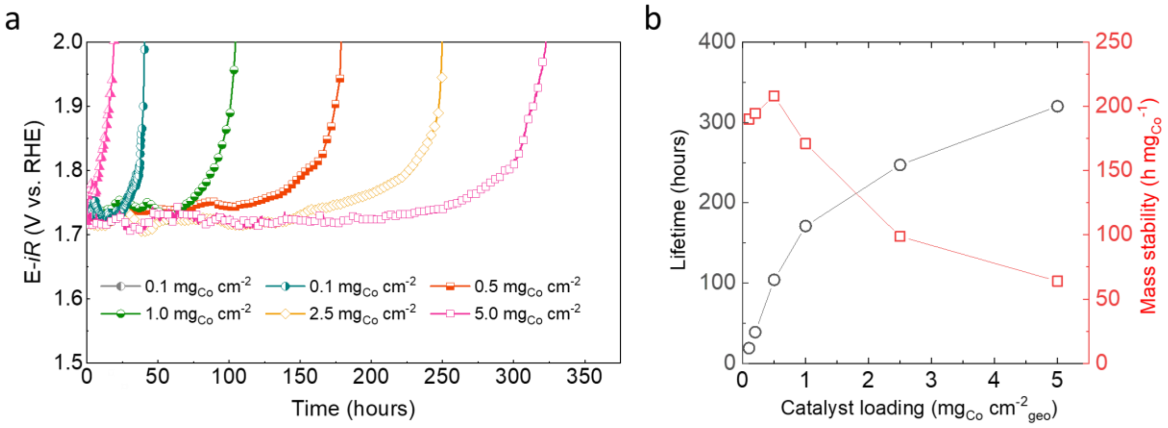

Supplementary Figure 48. Mass dependent stability measurements. a, Chronopotentiometry measurements of Co_2MnO_4 on FTO at 100 mA cm^{-2}_{geo} in H_2SO_4 (pH 1, 25 °C) with different catalyst loading (0.1, 0.2, 0.5, 1.0, 2.5 and 5.0 mg_{Co} cm^{-2}_{geo}). **b,** The lifetime and mass stability (lifetime divided by catalyst loading) plotted versus loading amount, measured at 100 mA cm^{-2}_{geo} in H_2SO_4 (pH 1, 25 °C).

DFT Calculation

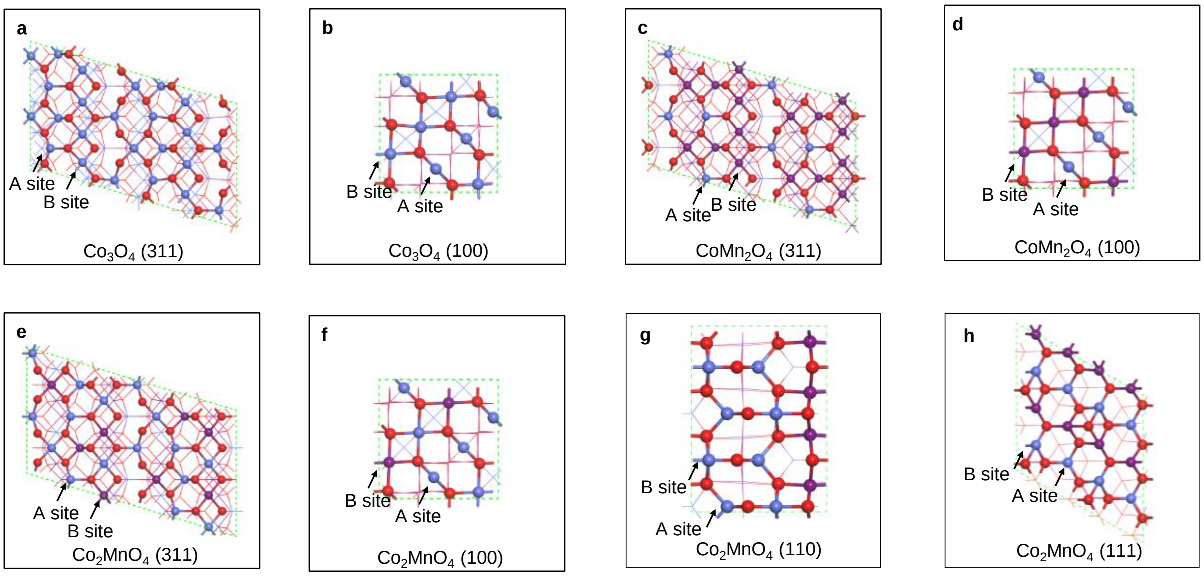

Supplementary Figure 49. Surface structures of Co_3O_4, $CoMn_2O_4$ and Co_2MnO_4. (311) and (100) surface structures of Co_3O_4 (**a, b**) and $CoMn_2O_4$ (**c, d**). (311), (100), (110) and (111) surface structures of Co_2MnO_4 (**e - h**). Monkhorst-Pack k-points of 1×2×1 was applied for (311) surfaces, and 4×4×1 was applied for spinel (100), (111) and (110) surfaces, respectively. The blue, purple and red atoms refer to Co, Mn and O, respectively. The arrows labeled by A and B site present the tetrahedral and octahedral site in spinel structures, respectively. In $CoMn_2O_4$, A site and B site were considered to be occupied by Co and Mn respectively. All A site metals and half of the B site metals were considered to be Co in Co_2MnO_4. In Co_2MnO_4, the (311) surface shows the lowest surface formation energy (140 meV/Å^2), followed by the (100) surface (171 meV/Å^2), (011) surface (196 meV/Å^2). In addition, the lowest cleavage energy for oxygen-terminated (111) surfaces is 247 meV/Å^2.

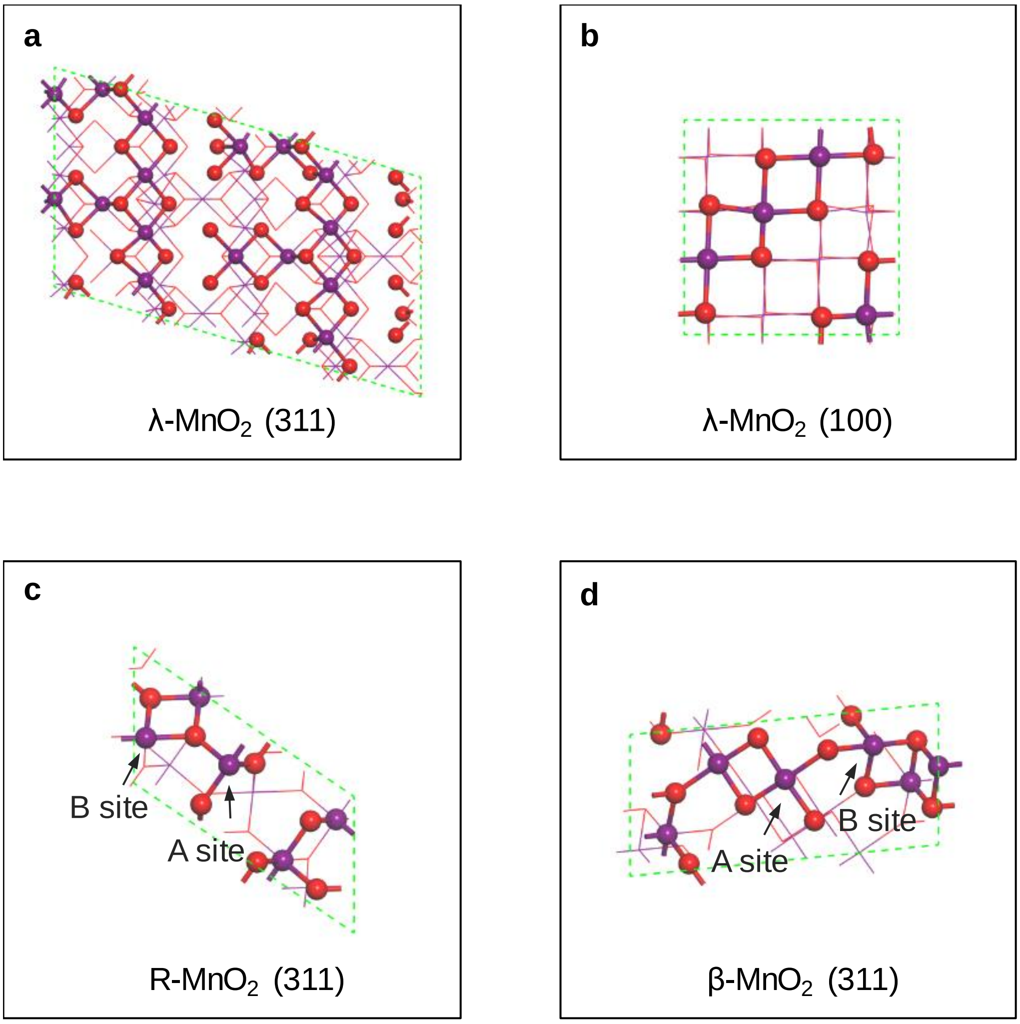

Supplementary Figure 50. Surface structures of λ-MnO_2, β-MnO_2 and R-MnO_2. (311) and (100) surface structures of λ-MnO_2 **(a, b)**. λ-MnO_2 was constructed based on the structure of spinel size Mn_3O_4, where all A site Mn atoms were removed. (311) surface structure of R-MnO_2 **(c)** and β-MnO_2 **(d)** calculated separately with Monkhorst-Pack k-points of 2×5×1 and 2×4×1, respectively. A and B sites refer to the surface Mn with different O coordination number. The purple and red atoms refer to Mn and O, respectively.

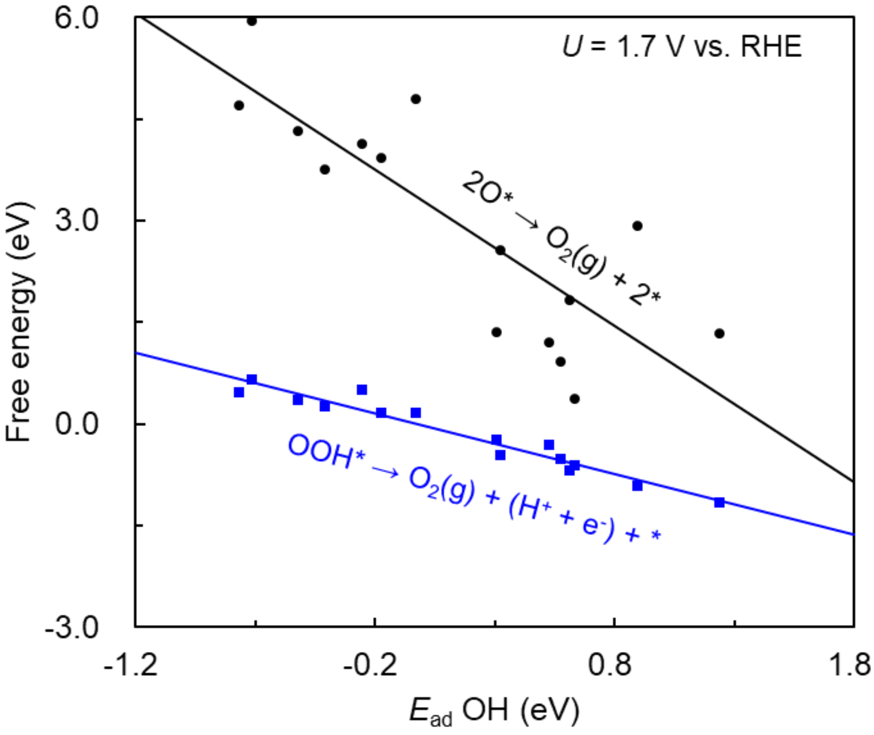

Supplementary Figure 51. A comparison between two O-O bond formation pathways. Reaction free energy comparison between two different O-O bond formation pathways in OER: O*-O* coupling and OOH* deprotonation at 1.7 V vs. RHE. OOH* deprotonation is more favorable than O*-O* direct coupling.

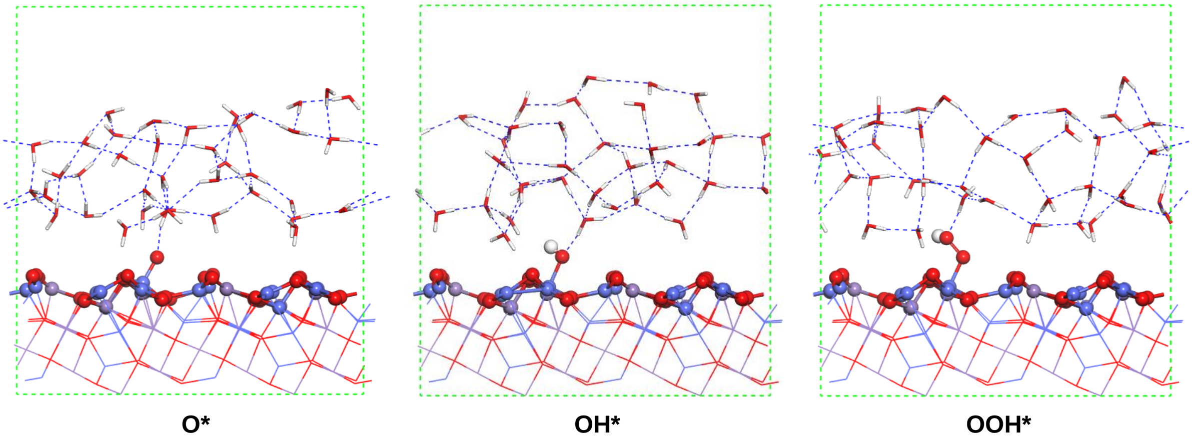

Supplementary Figure 52. Structures for solvent effect calculations. Four layers of water were applied on Co_2MnO_4 (311) surfaces. The calculations are based on explicit models.

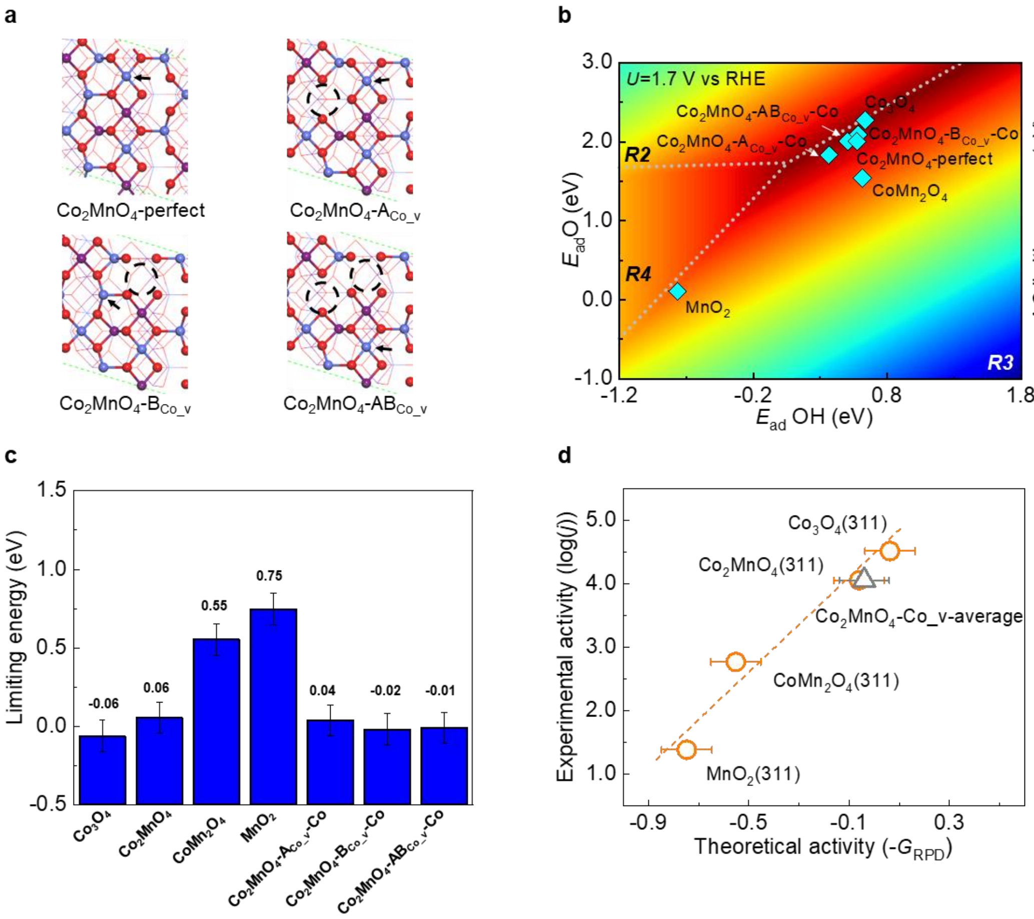

Supplementary Figure 53. Comparison of activity on Co-deficient (Mn-rich) surfaces of Co_2MnO_4. a, The local structures of the Co_2MnO_4 surfaces with Co vacancies in DFT calculations. The dashed circles describe the location of the Co vacancies (1 vacancy among the 12 Co sites within the unit cell, see Supplementary Figure 54). In order to assess the influence of vacancies on the activity, calculations were performed assuming that the Co site nearest to the vacancy is the active site (black arrows). For details of the structure, see Supplementary Table 21. **b**, Two-dimensional activity map showing the OER activity on different Mn-rich surfaces. **c**, Δ*G*-limiting energies for Co_3O_4, Co_2MnO_4, $CoMn_2O_4$, MnO_2 and different Mn-rich surfaces of Co_2MnO_4. The limiting energies were calculated following $\Delta G_{lim} = \max(\Delta G_1, \Delta G_2, \Delta G_3, \Delta G_4)$, where G_1 - G_4 refers to the reaction free energies of relevant elementary steps (see equations (1)-(4) in main text). Committing to a comparison with the limiting energies from the original calculations, the binding energies of O* and OH* were calculated explicitly, while the OOH* adsorption energies were obtained from the scaling relation vs. OH* (**Fig. 5a** in main text). **d**, The correlation between experimental activities (log(*j*)) and theoretical ones ($-\Delta G_{lim}$) derived from the Δ*G*-limiting energies. The triangle shows the theoretical result based on the average of all calculated limiting energies of Co-deficient Co_2MnO_4 surfaces shown in (a).

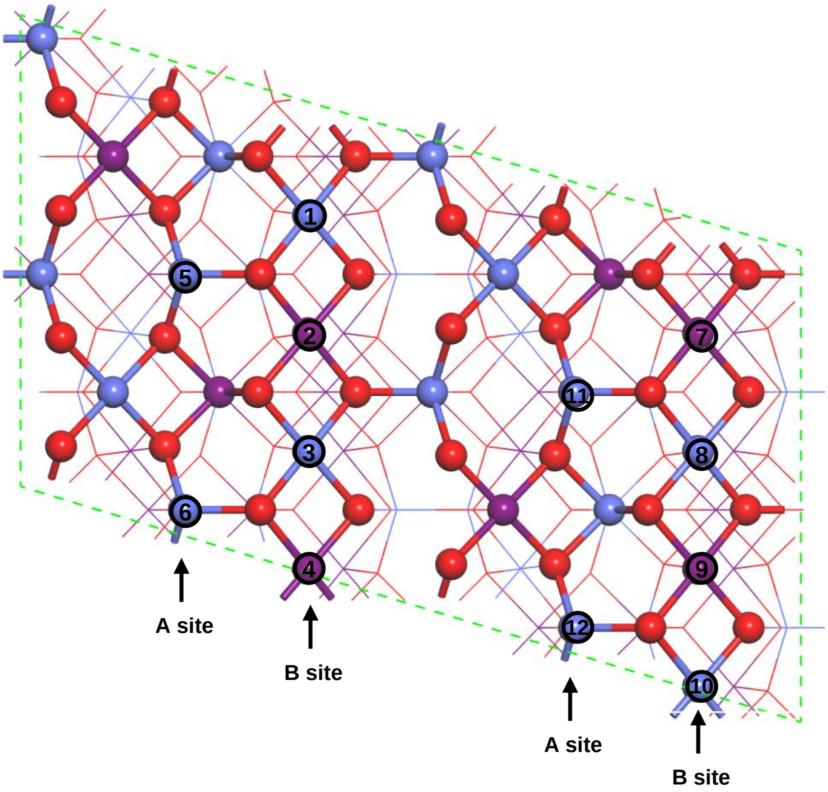

Supplementary Figure 54. The whole unit cell structure of Co_2MnO_4. The whole unit cell of Co_2MnO_4 with 4 A sites and 8 B sites on the surface.

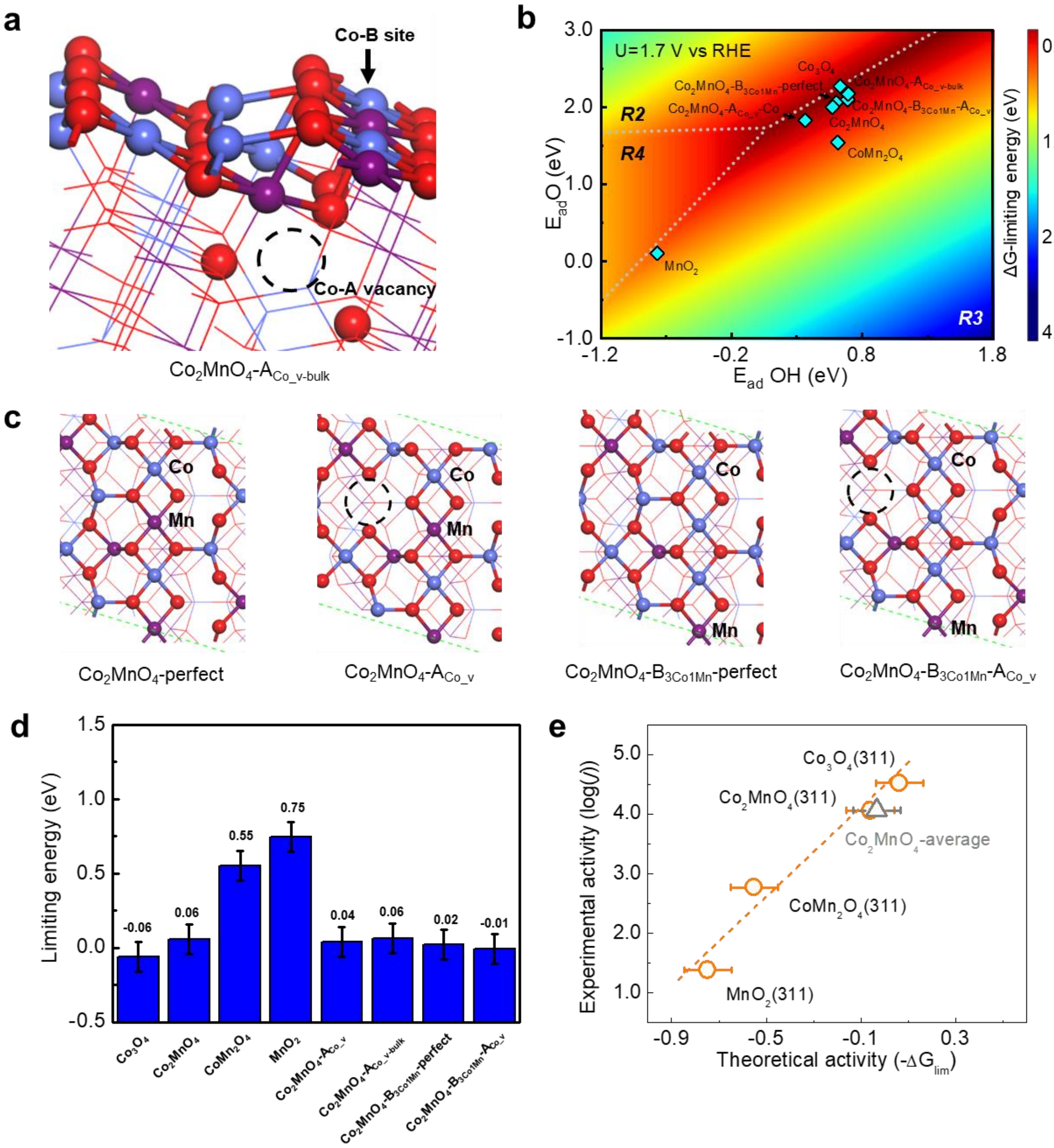

Supplementary Figure 55. Comparison of activity on Co_2MnO_4 with bulk defects. a, Surface structures of Mn-rich surface and surfaces with high Co:Mn ratio at the B site. The dashed circles describe the location of Co vacancies (Details of structure descriptions see Supplementary Table 21). **b**, Two-dimensional activity map showing the activity of OER on different surfaces. **c**, Limiting energies of OER on different surfaces. **d**, The correlation between experimental activities (log(j)) and theoretical ones ($-\Delta G_{lim}$) derived from the ΔG-limiting energies. The triangle shows the theoretical result based on the average of all calculated limiting energies of Co_2MnO_4 shown in (**c**).

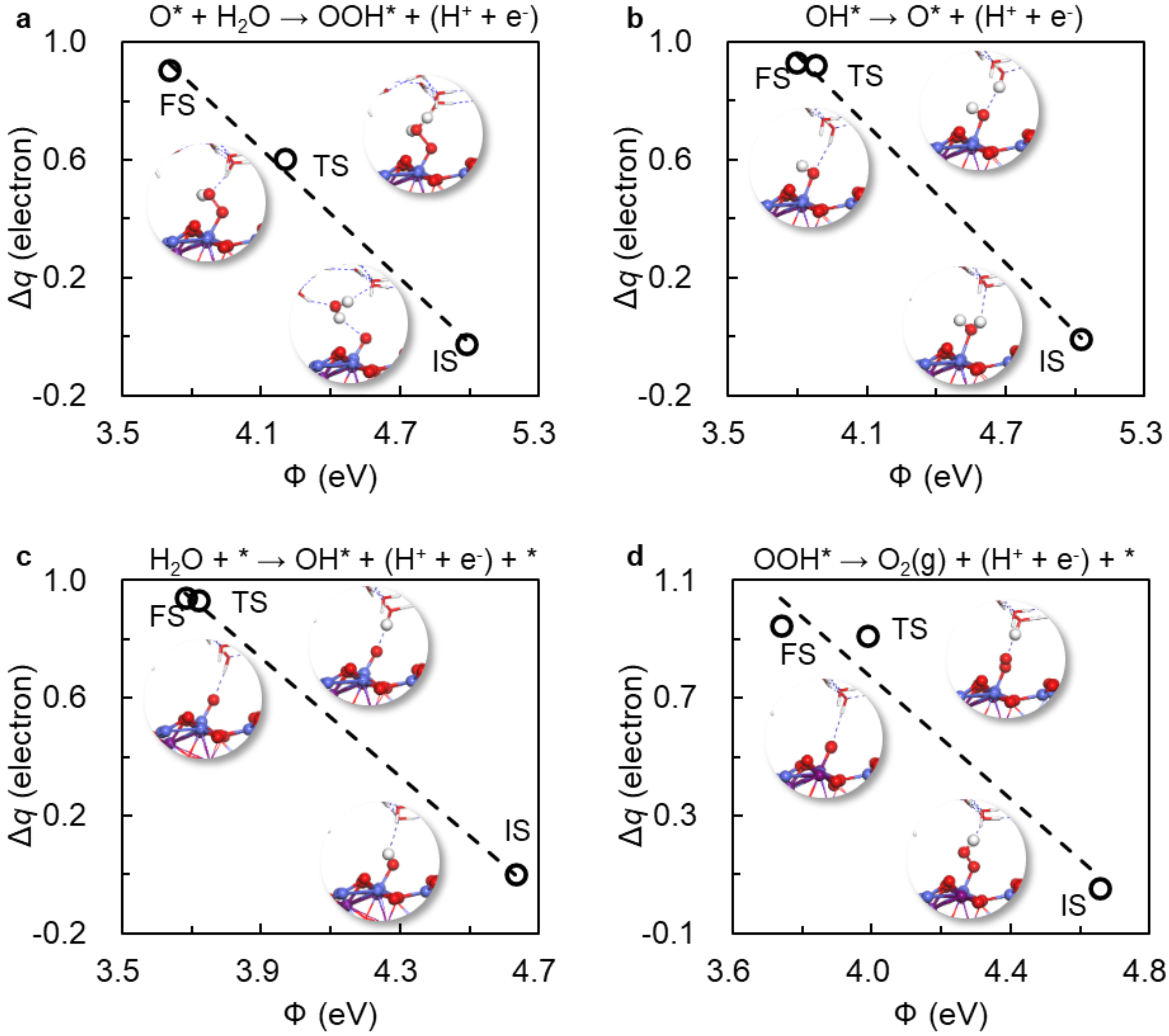

Supplementary Figure 56. Calculated charge transfer and work function. Calculated charge transfer (Δq) from water to electrode surface and work function (Φ) on the surfaces at surfaces at initial (IS), transition (TS) and final (FS) states for electrochemical processes in OER. The observed linear correlation between the amount of electron transfer and relative work functions supports the validity of the capacitor model.

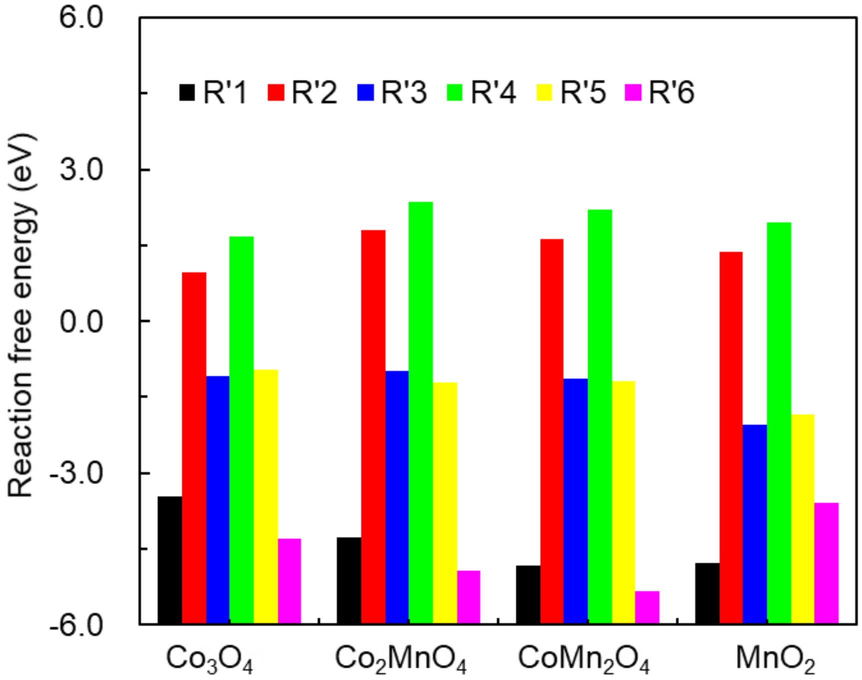

Supplementary Figure 57. Free energies of elementary steps in dissolution reaction. Reaction free energies of elementary steps in catalyst dissolution. Two different pathways were studied based on the priority of dissolution from either metal or oxygen. R’1 – R’3 is the M-path which prioritizes metal dissolution. R’4 – R’6 is the O-path which prioritizes oxygen dissolution. (See the detailed elementary steps in in Supplementary Table 23).

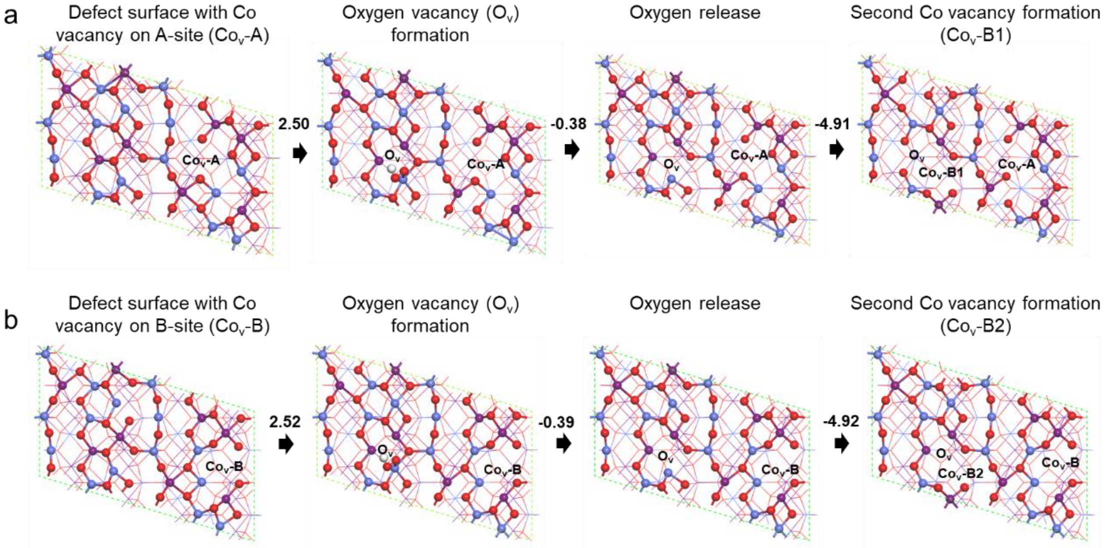

Supplementary Figure 58. Dissolution of O and Co on Co_2MnO_4 from a defect surface. Dissolution of O and Co on Co_2MnO_4 from a surface with a Co vacancy at the A-site (a) and B-site (b), based on the O-path in which oxygen dissolution precedes metal dissolution.

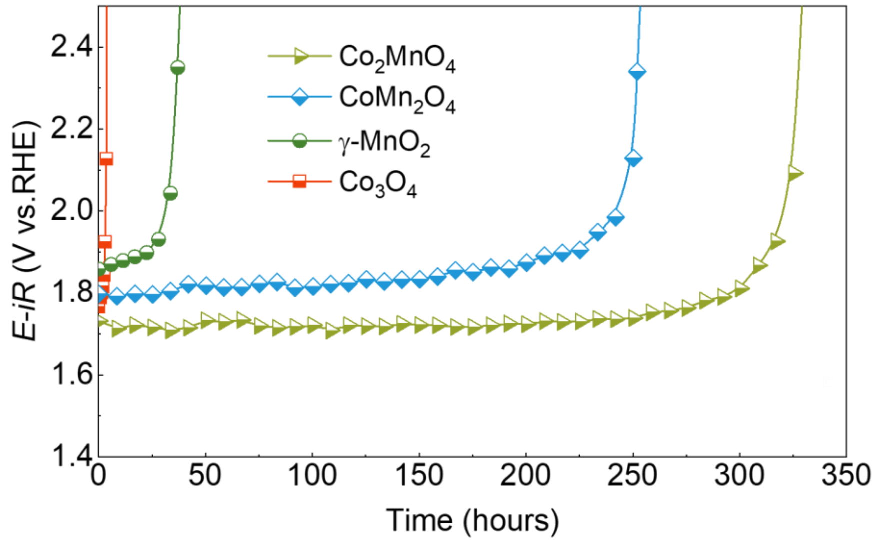

Supplementary Figure 59. CP measurements of Co_3O_4, Co_2MnO_4, $CoMn_2O_4$ and γ-MnO_2. CP measurements at 100 mA cm^{-2}_{geo} of γ-MnO_2, $CoMn_2O_4$, Co_2MnO_4 and Co_3O_4 deposited on FTO in H_2SO_4 (pH 0) at 25 °C. Geometric area, 0.28 cm^2.

Supplementary Tables

Supplementary Table 1. Structural parameters of Co_2MnO_4 from SR-PXRD Rietveld refinements.

Atom	**Site**	***g***	***x***	***y***	***z***	***B*(Å^2)**	***U*(Å^2)**
Co1	8*a*	0.841(3)	1/8	1/8	1/8	0.17(3)	0.0022(4)
Co2	16*d*	0.527(1)	1/2	1/2	1/2	0.28(2)	0.0036(3)
Mn	16*d*	0.473(1)	1/2	1/2	1/2	0.28(2)	0.0036(3)
O	32*e*	1	0.2628(3)	0.2628(3)	0.2628(3)	0.72(6)	0.0091(8)

Space group: Fd-3m space group; lattice parameters: a = 8.0866(3) Å, V = 528.80(4) Å^3*,* R_{wp} *= 3.76%,* R_p *= 2.90%,* R_e *= 2.66%, S = 1.41,* R_B *= 4.39%,* R_F *= 2.36%; 3718 profile points (2θ = 3.0091°-39.9979°); 43 refined variables; 10 restraints. g, occupancy; B, U, equivalent isotropic atomic displacement parameters calculated from anisotropic atomic displacement parameters; x, y, and z, atomic coordinates.* The structure was available from the Cambridge Crystal Structure Data Centre via internet (https://www.ccdc.cam.ac.uk/) with the deposition codes: CSD 2098166.

Supplementary Table 2. Structural parameters of Co_2MnO_4-4h from SR-PXRD Rietveld refinements.

Atom	**Site**	***g***	***x***	***y***	***z***	***B*(Å^2)**	***U*(Å^2)**
Co1	8*a*	0.771(3)	1/8	1/8	1/8	0.33(3)	0.0041(4)
Co2	16*d*	0.538(1)	1/2	1/2	1/2	0.31(2)	0.0040(3)
Mn	16*d*	0.462(1)	1/2	1/2	1/2	0.31(4)	0.0040(3)
O	32*e*	1	0.2643(2)	0.2643(2)	0.2643(2)	0.60(2)	0.0076(8)

Space group: Fd-3m space group; lattice parameters a = 8.0744(4) Å, V = 526.43(4) Å^3, R_{wp} = 2.98%, R_p = 2.33%, R_e = 2.29%, S = 1.30, R_B = 1.39%, R_F = 0.92%; 3718 profile points (2θ = 3.0091°-39.9979°); 47 refined variables; 10 restraints. g, occupancy; B, U, equivalent isotropic atomic displacement parameters calculated from anisotropic atomic displacement parameters; x, y, and z, atomic coordinates. The structure was available from the Cambridge Crystal Structure Data Centre via internet (https://www.ccdc.cam.ac.uk/) with the deposition codes: CSD 2098164.

Supplementary Table 3. Structural parameters of Co_2MnO_4-23h from SR-PXRD Rietveld refinements.

Atom	**Site**	***g***	***x***	***y***	***z***	**B(Å^2)**	**U(Å^2)**
Co1	8*a*	0.715(4)	1/8	1/8	1/8	0.31(4)	0.0039(5)
Co2	16*d*	0.547(1)	1/2	1/2	1/2	0.35(3)	0.0044(3)
Mn	16*d*	0.453(1)	1/2	1/2	1/2	0.35(3)	0.0044(3)
O	32*e*	1	0.2635(3)	0.2635(3)	0.2635(3)	0.71(7)	0.0090(9)

Space group: Fd-3m space group; lattice parameters: a = 8.0723(4) Å, V = 526.02(5) Å^3*,* R_{wp} *= 2.88%,* R_p *= 2.28%,* R_e *= 2.31%, S = 1.25,* R_B *= 2.11%,* R_F *= 1.32%; 3718 profile points (2θ = 3.0091°-39.9979°); 47 refined variables; 10 restraints. g, occupancy; B, U, equivalent isotropic atomic displacement parameters calculated from anisotropic atomic displacement parameters; x, y, and z, atomic coordinates.* The structure was available from the Cambridge Crystal Structure Data Centre via internet (https://www.ccdc.cam.ac.uk/) with the deposition codes: CSD 2098165. The Rietveld refinements show the occupancy of cobalt on tetragonal sites (8a) was decreased from 0.841(3) to 0.771(3) and 0.715(4) after electrolysis for 4 and 23 hours, respectively, suggesting that cobalt leaches predominantly from the tetragonal sites during electrolysis.

Supplementary Table 4. Fitting parameters of the Fourier-transformed k^3-weighted Co K-edge EXAFS spectra of Co_3O_4. The uncertainty is given in parentheses. Two commonly used parameters of *R*-factor and reduced chi-square were shown validating the rational fitting.

	Path	N^a	ΔR(Å)	R(Å)	σ^2(Å^2)	S_0^2	ΔE_0(eV)
A site[b]	Co_A-O	4	-0.002 (0.002)	1.941 (0.002)	0.0037 (0.0003)	0.85 (0.03)	1.6 (0.4)
	Co_A-Co_B	12	0.013 (0.004)	3.359 (0.004)	0.0054 (0.0004)		
	Co_A-Co_A	4	0.01 (0.02)	3.51 (0.02)	0.003 (0.001)		
B site[b]	Co_B-O	6	-0.002 (0.002)	1.909 (0.002)	0.0037 (0.0003)		
	Co_B-Co_B	6	0.005 (0.002)	2.859 (0.002)	0.0036 (0.0002)		
	Co_B-Co_A	6	0.013 (0.004)	3.359 (0.004)	0.0054 (0.0004)		
Reduced chi-square: 87; *R*-factor: 0.0018							

[a] *Coordination numbers were fixed to the crystallography values.*

[b] *A site represents the tetrahedral site and B site represents the octahedral site in the spinel structure (AB_2O_4). Same for Supplementary Tables 5-7.*

Supplementary Table 5. Fitting parameters of the Fourier-transformed k^3-weighted Mn K-edge EXAFS spectra of MnO_2. The uncertainty is given in parentheses. Two commonly used parameters of *R*-factor and reduced chi-square were shown validating the rational fitting.

Path	N^a	ΔR(Å)	R(Å)	σ^2(Å^2)	S_0^2	ΔE_0(eV)
Mn-O	6	-0.004 (0.005)	1.882 (0.005)	0.0028 (0.0006)	0.78 (0.07)	0.2 (0.9)
Mn-Mn.1 (second shell)	2	0.008 (0.007)	2.881 (0.007)	0.0021 (0.0007)		
Mn-Mn.2 (third shell)	8	0.011 (0.006)	3.437 (0.006)	0.0041 (0.0005)		
Reduced chi-square: 433; *R*-factor: 0.020						

[a] *Coordination numbers were fixed to crystallography values.*

Supplementary Table 6. Fitting parameters of Fourier-transformed k^3-weighted Co K-edge EXAFS spectra of Co_2MnO_4 before electrolysis and Co_2MnO_4 after electrolysis at 100 mA cm^{-2}$_{geo}$ (pH 1 H_2SO_4, 25 °C) for 4 hours (Co_2MnO_4-4h) and 23 hours (Co_2MnO_4-23h). The uncertainty is given in parentheses. Two commonly used parameters of *R*-factor and reduced chi-square were shown validating the rational fitting[a].

		A site				B site			
		Co$_A$-O	Co$_A$-Co$_B$	Co$_A$-Mn$_B$	Co$_A$-Co$_A$	Co$_B$-O	Co$_B$-Co$_B$	Co$_B$-Mn$_B$	Co$_B$-Co$_A$
Co_2MnO_4	N^b	4.1(0.5)	6.3	5.7	3.4	6.1(0.5)	3.2	2.8	5.0
	σ^2(Å^2)	0.0041 (0.0003)	0.0074 (0.0003)	0.0074 (0.0003)	0.008 (0.002)	0.0041 (0.0003)	0.0039 (0.0001)	0.0039 (0.0001)	0.0074 (0.0003)
	ΔR(Å)	-0.007 (0.002)	0.020 (0.003)	0.020 (0.003)	0.03 (0.02)	-0.007 (0.002)	0.006 (0.001)	0.006 (0.001)	0.020 (0.003)
	R(Å)	1.923 (0.002)	3.372 (0.003)	3.372 (0.003)	3.53 (0.02)	1.916 (0.002)	2.865 (0.001)	2.865 (0.001)	3.372 (0.003)
Co_2MnO_4-4h	N^b	4.1(0.5)	6.5	5.5	3.1	6.2(0.4)	3.2	2.8	4.6
	σ^2(Å^2)	0.0040 (0.0002)	0.0076 (0.0003)	0.0076 (0.0003)	0.007 (0.002)	0.0040 (0.0002)	0.0041 (0.0001)	0.0041 (0.0001)	0.0076 (0.0003)
	ΔR(Å)	-0.010 (0.001)	0.017 (0.003)	0.017 (0.003)	0.03 (0.02)	-0.010 (0.001)	0.002 (0.001)	0.002 (0.001)	0.017 (0.003)
	R(Å)	1.920 (0.001)	3.370 (0.003)	3.370 (0.003)	3.53 (0.02)	1.914 (0.001)	2.861 (0.001)	2.861 (0.001)	3.370 (0.003)
Co_2MnO_4-23h	N^b	4.1(0.6)	6.6	5.4	2.9	6.2(0.4)	3.3	2.7	4.3
	σ^2(Å^2)	0.0040 (0.0003)	0.0076 (0.0004)	0.0076 (0.0004)	0.007 (0.003)	0.0040 (0.0003)	0.0043 (0.0002)	0.0043 (0.0002)	0.0076 (0.0004)
	ΔR(Å)	-0.011 (0.002)	0.017 (0.003)	0.017 (0.003)	0.03 (0.02)	-0.011 (0.002)	0.001 (0.002)	0.001 (0.002)	0.017 (0.003)
	R(Å)	1.919 (0.002)	3.370 (0.003)	3.370 (0.003)	3.54 (0.02)	1.913 (0.002)	2.860 (0.002)	2.860 (0.002)	3.370 (0.003)
S_0^2 = 0.85; ΔE_0 = 1.6 eV[c]									
Reduced chi-square: 167; *R*-factor: 0.0015[d]									

[a] *The average Co-O coordination number was calculated by weighting the fitted results of Co$_A$-O and Co$_B$-O in relative proportions of Co in A site and B site obtained from SR-PXRD Rietveld refinement. The results are 5.2, 5.3 and 5.4 for Co_2MnO_4, Co_2MnO_4-4h and Co_2MnO_4-23h, respectively.*

[b] *The coordination numbers of Co$_A$-O and Co$_B$-O were let free, others were fixed. Particularly, the coordination numbers of Co$_A$-Co$_B$, Co$_A$-Mn$_B$, Co$_A$-Co$_A$, Co$_B$-Co$_B$, Co$_B$-Mn$_B$ and Co$_B$-Co$_A$ were calculated by multiplying corresponding occupancy obtained from SR-PXRD Rietveld refinements to the crystallography coordination number values.*

[c] *The S_0^2 and ΔE_0 was obtained by fitting of standard Co_3O_4 sample.*

[d] *Three data set of Co_2MnO_4 before and after electrolysis were fitted together. Therefore, they shared the same reduced chi-square and R-factor.*

Supplementary Table 7. Fitting parameters of the Fourier-transformed k^3-weighted Mn K-edge EXAFS spectra of Co_2MnO_4 before electrolysis and Co_2MnO_4 after electrolysis at 100 mA cm^{-2}_{geo} (pH 1 H_2SO_4, 25 °C) for 4 hours (Co_2MnO_4-4h) and 23 hours (Co_2MnO_4-23h). The uncertainty is given in parentheses. Two commonly used parameters of *R*-factor and reduced chi-square were shown validating the rational fitting.

Samples	Path	N^a	ΔR(Å)	R(Å)	σ^2(Å^2)
Co_2MnO_4	Mn_B-O.1	5.5 (0.4)	-0.043 (0.003)	1.880 (0.003)	0.0050 (0.0005)
	Mn_B-Mn_B	3.2	-0.003 (0.003)	2.856 (0.003)	0.0095 (0.0004)
	Mn_B-Co_B	2.8	-0.003 (0.003)	2.856 (0.003)	0.0095 (0.0004)
	Mn_B-Co_A	5.0	0.07 (0.01)	3.42 (0.01)	0.010 (0.001)
	Mn_B-O.3	6	0.05 (0.03)	3.61 (0.03)	0.006 (0.002)
Co_2MnO_4-4h	Mn_B-O.1	6.0 (0.6)	-0.044 (0.005)	1.880 (0.005)	0.0054 (0.0009)
	Mn_B-Mn_B	3.2	-0.014 (0.006)	2.845 (0.006)	0.0087 (0.0006)
	Mn_B-Co_B	2.8	-0.014 (0.006)	2.845 (0.006)	0.0087 (0.0006)
	Mn_B-Co_A	4.6	0.07 (0.03)	3.42 (0.03)	0.010 (0.002)
	Mn_B-O.3	6	0.04 (0.05)	3.61 (0.05)	0.005 (0.004)
Co_2MnO_4-23h	Mn_B-O.1	5.9 (0.8)	-0.045 (0.005)	1.878 (0.005)	0.005 (0.001)
	Mn_B-Mn_B	3.3	-0.016 (0.006)	2.843 (0.006)	0.0086 (0.0007)
	Mn_B-Co_B	2.7	-0.016 (0.006)	2.843 (0.006)	0.0086 (0.0007)
	Mn_B-Co_A	4.3	0.07 (0.03)	3.42 (0.03)	0.009 (0.002)
	Mn_B-O.3	6	0.05 (0.06)	3.61 (0.06)	0.006 (0.005)
$S_0^2 = 0.78$; $\Delta E_0 = 0.2$ eV^b					
Reduced chi-square: 714; *R*-factor: 0.014^c					

[a] *The coordination number of Mn_B-O.1 was let free, others were fixed. Particularly, the coordination numbers of Mn_B-Mn_B, Mn_B-Co_B and Mn_B-Co_A were calculated by multiplying corresponding occupancy obtained from SR-PXRD Rietveld refinements to the crystallography coordination number values.*

[b] *The S_0^2 and ΔE_0 was obtained by fitting of standard β-MnO_2 sample.*

[c] *Three data set of Co_2MnO_4 before and after electrolysis were fitted together. Therefore, they shared the same reduced chi-square and R-factor.*

Supplementary Table 8. Fitting parameters of XPS Co*2p* spectrum of Co_2MnO_4 before electrolysis.

No	Name	Position	FWHM	Line shape	%At
1	Co^{3+} $2p_{3/2}$	779.64	1.58	GL(30)	25.5%
2	Co^{3+} $2p_{3/2}$ satellite	789.00	4.18	GL(30)	7.2%
3	Co^{3+} $2p_{1/2}$	794.81	1.70	GL(30)	12.8%
4	Co^{3+} $2p_{1/2}$ satellite	805.02	4.71	GL(30)	4.7%
5	Co^{2+} $2p_{3/2}$	781.00	2.08	GL(30)	19.6%
6	Co^{2+} $2p_{3/2}$ satellite	782.45	5.78	GL(30)	17.4%
7	Co^{2+} $2p_{1/2}$	796.55	2.20	GL(30)	9.8%
8	Co^{2+} $2p_{1/2}$ satellite	801.78	4.71	GL(30)	3.1%

Supplementary Table 9. Fitting parameters of XPS Co$2p$ spectrum of Co_2MnO_4-4h (after electrolysis for 4 hours at 100 mA cm$^{-2}{}_{geo}$, pH 1 H_2SO_4, 25 °C).

No	Name	Position	FWHM	Line shape	%At
1	Co^{3+} $2p_{3/2}$	779.64	1.65	GL(30)	30.07
2	Co^{3+} $2p_{3/2}$ satellite	789	3.82	GL(30)	6.48
3	Co^{3+} $2p_{1/2}$	794.81	1.78	GL(30)	15.03
4	Co^{3+} $2p_{1/2}$ satellite	805.02	4.07	GL(30)	4.21
5	Co^{2+} $2p_{3/2}$	781	2.14	GL(30)	16.73
6	Co^{2+} $2p_{3/2}$ satellite	782.45	5.21	GL(30)	16.3
7	Co^{2+} $2p_{1/2}$	796.55	2.13	GL(30)	8.37
8	Co^{2+} $2p_{1/2}$ satellite	801.78	4.07	GL(30)	2.81

Supplementary Table 10. Fitting parameters of XPS Co*2p* spectrum of Co_2MnO_4-23h (after electrolysis for 23 hours at 100 mA cm^{-2}_{geo}, pH 1 H_2SO_4, 25 °C).

No	Name	Position	FWHM	Line shape	%At
1	Co^{3+} $2p_{3/2}$	779.64	1.86	GL(30)	36.42
2	Co^{3+} $2p_{3/2}$ satellite	789	3.8	GL(30)	7.14
3	Co^{3+} $2p_{1/2}$	794.81	2.07	GL(30)	18.21
4	Co^{3+} $2p_{1/2}$ satellite	805.02	4.29	GL(30)	0.23
5	Co^{2+} $2p_{3/2}$	781	2.54	GL(30)	14.17
6	Co^{2+} $2p_{3/2}$ satellite	782.45	5.40	GL(30)	16.59
7	Co^{2+} $2p_{1/2}$	796.55	2.32	GL(30)	7.08
8	Co^{2+} $2p_{1/2}$ satellite	801.78	4.29	GL(30)	0.15

Supplementary Table 11. Fitting parameters of XPS Mn*2p* spectrum of Co_2MnO_4 before electrolysis.

No	Name	Position	FWHM	Line shape	%At
1	Mn^{4+}-Peak 1	642.03	1.45	GL(50)	6.7
2	Mn^{4+}-Peak 2	642.81	1.45	GL(50)	3.6
3	Mn^{4+}-Peak 3	643.40	1.45	GL(50)	3.3
4	Mn^{4+}-Peak 4	644.10	1.45	GL(50)	1.9
5	Mn^{4+}-Peak 5	644.88	1.45	GL(50)	1.1
6	Mn^{4+}-Peak 6	645.79	1.45	GL(50)	0.6
7	Mn^{4+}-Peak 7	646.88	1.45	GL(50)	0.2
8	Mn^{4+}-Peak 8	647.10	1.45	GL(50)	0.1
9	Mn^{3+}-Peak 1	640.78	1.60	GL(50)	20.2
10	Mn^{3+}-Peak 2	641.57	1.60	GL(50)	20.3
11	Mn^{3+}-Peak 3	642.25	1.60	GL(50)	16.2
12	Mn^{3+}-Peak 4	643.01	1.60	GL(50)	12.5
13	Mn^{3+}-Peak 5	643.83	1.60	GL(50)	6.6
14	Mn^{3+}-Peak 6	644.67	1.60	GL(50)	3.6
15	Mn^{3+}-Peak 7	645.69	1.60	GL(50)	1.5
16	Mn^{3+}-Peak 8	638.98	1.91	GL(50)	0.7
17	Mn^{2+}-Peak 1	639.28	1.70	GL(50)	0.3
18	Mn^{2+}-Peak 2	640.32	1.70	GL(30)	0.2
19	Mn^{2+}-Peak 3	641.08	1.70	GL(30)	0.1
20	Mn^{2+}-Peak 4	641.96	1.70	GL(30)	0.1
21	Mn^{2+}-Peak 5	643.04	1.70	GL(30)	0.0
22	Mn^{2+}-Peak 6	644.13	2.10	GL(30)	0.0
23	Mn^{2+}-Peak 7	646.16	3.12	GL(30)	0.1
24	Mn^{2+}-Peak 8	637.63	1.90	GL(30)	0.0

Supplementary Table 12. Fitting parameters of XPS Mn*2p* spectrum of Co_2MnO_4-4h (after electrolysis for 4 hours at 100 mA $cm^{-2}{}_{geo}$, pH 1 H_2SO_4, 25 °C).

No	Name	Position	FWHM	Line shape	%At
1	Mn^{4+}-Peak 1	642.03	1.33	GL(50)	6.43
2	Mn^{4+}-Peak 2	642.81	1.33	GL(50)	4.08
3	Mn^{4+}-Peak 3	643.4	1.33	GL(50)	3.94
4	Mn^{4+}-Peak 4	644.1	1.33	GL(50)	1.7
5	Mn^{4+}-Peak 5	644.88	1.33	GL(50)	1.02
6	Mn^{4+}-Peak 6	645.79	1.33	GL(50)	0.53
7	Mn^{4+}-Peak 7	646.88	1.33	GL(50)	0.22
8	Mn^{4+}-Peak 8	647.1	1.33	GL(50)	0.08
9	Mn^{3+}-Peak 1	640.78	1.48	GL(50)	20.47
10	Mn^{3+}-Peak 2	641.57	1.48	GL(50)	20.58
11	Mn^{3+}-Peak 3	642.25	1.48	GL(50)	15.42
12	Mn^{3+}-Peak 4	643.01	1.48	GL(50)	11.72
13	Mn^{3+}-Peak 5	643.83	1.48	GL(50)	6.71
14	Mn^{3+}-Peak 6	644.67	1.48	GL(50)	3.6
15	Mn^{3+}-Peak 7	645.69	1.48	GL(50)	1.5
16	Mn^{3+}-Peak 8	638.98	1.48	GL(50)	0.74
17	Mn^{2+}-Peak 1	639.28	1.58	GL(50)	0.42
18	Mn^{2+}-Peak 2	640.32	1.58	GL(30)	0.21
19	Mn^{2+}-Peak 3	641.08	1.58	GL(30)	0.21
20	Mn^{2+}-Peak 4	641.96	1.58	GL(30)	0.15
21	Mn^{2+}-Peak 5	643.04	1.58	GL(30)	0.07
22	Mn^{2+}-Peak 6	644.13	1.58	GL(30)	0.03
23	Mn^{2+}-Peak 7	646.16	1.58	GL(30)	0.13
24	Mn^{2+}-Peak 8	637.63	1.98	GL(30)	0.02

Supplementary Table 13. Fitting parameters of XPS Mn*2p* spectrum of Co_2MnO_4-23h (after electrolysis for 23 hours at 100 mA cm^{-2}_{geo}, pH 1 H_2SO_4, 25 °C).

No	Name	Position	FWHM	Line shape	%At
1	Mn^{4+}-Peak 1	642.03	1.34	GL(50)	6.85
2	Mn^{4+}-Peak 2	642.81	1.34	GL(50)	3.89
3	Mn^{4+}-Peak 3	643.4	1.34	GL(50)	3.65
4	Mn^{4+}-Peak 4	644.1	1.34	GL(50)	2.01
5	Mn^{4+}-Peak 5	644.88	1.34	GL(50)	1.31
6	Mn^{4+}-Peak 6	645.79	1.34	GL(50)	0.55
7	Mn^{4+}-Peak 7	646.88	1.34	GL(50)	0.23
8	Mn^{4+}-Peak 8	647.1	1.34	GL(50)	0.08
9	Mn^{3+}-Peak 1	640.78	1.49	GL(50)	20.34
10	Mn^{3+}-Peak 2	641.57	1.49	GL(50)	20.44
11	Mn^{3+}-Peak 3	642.25	1.49	GL(50)	15.31
12	Mn^{3+}-Peak 4	643.01	1.49	GL(50)	12.13
13	Mn^{3+}-Peak 5	643.83	1.49	GL(50)	6.16
14	Mn^{3+}-Peak 6	644.67	1.49	GL(50)	3.58
15	Mn^{3+}-Peak 7	645.69	1.49	GL(50)	1.49
16	Mn^{3+}-Peak 8	638.98	1.49	GL(50)	0.74
17	Mn^{2+}-Peak 1	639.28	1.59	GL(50)	0.39
18	Mn^{2+}-Peak 2	640.32	1.59	GL(30)	0.27
19	Mn^{2+}-Peak 3	641.08	1.59	GL(30)	0.2
20	Mn^{2+}-Peak 4	641.96	1.59	GL(30)	0.14
21	Mn^{2+}-Peak 5	643.04	1.59	GL(30)	0.06
22	Mn^{2+}-Peak 6	644.13	1.59	GL(30)	0.03
23	Mn^{2+}-Peak 7	646.16	1.59	GL(30)	0.12
24	Mn^{2+}-Peak 8	637.63	1.99	GL(30)	0.02

Supplementary Table 14. Activity and stability comparison of 3d catalysts in literature. The activity is summarized in terms of the three metrics: (1) overpotential (η) at 10 mA cm$^{-2}_{geo}$, as a general metric in literature; (2) specific activity per electrochemical surface area (j_{ECSA}) at η = 0.35 V, following the protocol suggested by McCrory et al. (ref. [12]); (3) the activity per geometric area (j_{geo}) at η = 0.72 V, where Co_2MnO_4 on FTO reached 1000 mA cm$^{-2}_{geo}$ in this work. All overpotentials refer to the values after *iR* correction. As there is no consistent criteria to evaluate stability, the electrochemical conditions used for the stability evaluation is also included in the table. The most active material from each literature is shown in Fig. 4b, along with some other materials such as amorphous $CoMnO_x$, which was chosen due to its similar elemental composition with Co_2MnO_4.

Catalyst material	Preparation methods	η (V) at 10 mA cm$^{-2}_{geo}$	j_{ECSA} at η = 0.35 V (mA cm$^{-2}_{ECSA}$)	j_{geo} at η = 0.72 V (mA cm$^{-2}_{geo}$)	Electrolyte condition	Stability performance	Ref
Co_2MnO_4 on FTO	Thermal decomposition	0.395	0.027	1000	pH 1.0 H_2SO_4	320 h at 100 mA cm$^{-2}_{geo}$ (LT)	This work
Co_2MnO_4 on Pt/Ti mesh	Thermal decomposition	0.298	0.020	2000 at η = 0.63 V	pH 1.0 in Pi	1500 h at 200 mA cm$^{-2}_{geo}$ (LT)	This work
γ-MnO_2	Thermal decomposition	0.489 ± 0.005	NA	NA	1.0 M H_2SO_4	8000 h at 10 mA cm$^{-2}_{geo}$ (OT)	20
Co-(b)	Electrodeposition	1.12 ± 0.01^a	< 0.01	NA	1.0 M H_2SO_4	< 2 h at 10 mA cm$^{-2}_{geo}$ (LT)	12
Co/B	Electrodeposition	1.13 ± 0.01^a	< 0.01	NA	1.0 M H_2SO_4	< 2 h at 10 mA cm$^{-2}_{geo}$ (LT)	12
Co/P-(a)	Electrodeposition	1.12 ± 0.02^a	< 0.01	NA	1.0 M H_2SO_4	< 2 h at 10 mA cm$^{-2}_{geo}$ (LT)	12
Co/P-(b)	Electrodeposition	1.13 ± 0.01^a	< 0.01	NA	1.0 M H_2SO_4	< 2 h at 10 mA cm$^{-2}_{geo}$ (LT)	12
CoFe	Electrodeposition	1.11 ± 0.01^a	< 0.01	NA	1.0 M H_2SO_4	< 2 h at 10 mA cm$^{-2}_{geo}$ (LT)	12
Cu	Electrodeposition	1.12 ± 0.02^a	< 0.01	NA	1.0 M H_2SO_4	< 2 h at 10 mA cm$^{-2}_{geo}$ (LT)	12
Fe(b)	Electrodeposition	1.14 ± 0.01^a	< 0.01	NA	1.0 M H_2SO_4	< 2 h at 10 mA cm$^{-2}_{geo}$ (LT)	12
FeMn	Electrodeposition	1.14 ± 0.01^a	< 0.01	NA	1.0 M H_2SO_4	< 2 h at 10 mA cm$^{-2}_{geo}$ (LT)	12
Ni(b)	Electrodeposition	1.10 ± 0.04^a	< 0.01	NA	1.0 M H_2SO_4	< 2 h at 10 mA cm$^{-2}_{geo}$ (LT)	12
Ni/B	Electrodeposition	1.15 ± 0.04^a	< 0.01	NA	1.0 M H_2SO_4	< 2 h at 10 mA cm$^{-2}_{geo}$ (LT)	12
NiCe	Electrodeposition	1.12 ± 0.01^a	< 0.01	NA	1.0 M H_2SO_4	< 2 h at 10 mA cm$^{-2}_{geo}$ (LT)	12
NiCo-(b)	Electrodeposition	1.13 ± 0.01^a	< 0.01	NA	1.0 M H_2SO_4	< 2 h at 10 mA cm$^{-2}_{geo}$ (LT)	12
NiCo-(c)	Electrodeposition	1.12 ± 0.01^a	< 0.01	NA	1.0 M H_2SO_4	< 2 h at 10 mA cm$^{-2}_{geo}$ (LT)	12
NiCr	Electrodeposition	1.12 ± 0.01^a	< 0.01	NA	1.0 M H_2SO_4	< 2 h at 10 mA cm$^{-2}_{geo}$ (LT)	12
NiCu	Electrodeposition	1.12 ± 0.02^a	< 0.01	NA	1.0 M H_2SO_4	< 2 h at 10 mA cm$^{-2}_{geo}$ (LT)	12
NiFe-(b)	Electrodeposition	1.12 ± 0.01^a	< 0.01	NA	1.0 M H_2SO_4	< 2 h at 10 mA cm$^{-2}_{geo}$ (LT)	12
NiFe-(c)	Electrodeposition	1.12 ± 0.01^a	< 0.01	NA	1.0 M H_2SO_4	< 2 h at 10 mA cm$^{-2}_{geo}$ (LT)	12
NiLa	Electrodeposition	1.12 ± 0.01^a	< 0.01	NA	1.0 M H_2SO_4	< 2 h at 10 mA cm$^{-2}_{geo}$ (LT)	12
NiMoFe-(b)	Electrodeposition	1.12 ± 0.04^a	< 0.01	NA	1.0 M H_2SO_4	< 2 h at 10 mA cm$^{-2}_{geo}$ (LT)	12
NiSn-(b)	Electrodeposition	1.17 ± 0.07^a	< 0.01	NA	1.0 M H_2SO_4	< 2 h at 10 mA cm$^{-2}_{geo}$ (LT)	12
$Mn_{0.9}Nb_{0.1}O_2$	Wet impregnation	0.87	0.012	NA	0.5 M H_2SO_4	NA	21
$Mn_{0.9}Nb_{0.1}O_2$:10F	Wet impregnation	0.82	0.012	NA	0.5 M H_2SO_4	NA	21
$Mn_{0.8}Nb_{0.2}O_2$:10F	Wet impregnation	0.68	0.016	NA	0.5 M H_2SO_4	25 h at 1.9 V vs. RHE (OT) *j* from 8 to 5 mA cm$^{-2}_{geo}$	21
$(Mn_{0.8}Nb_{0.2})O_2$	Wet impregnation	0.77	0.014	NA	0.5 M H_2SO_4	25 h at 1.9 V vs. RHE (OT) *j* from 6 to 3 mA cm$^{-2}_{geo}$	21
$Ni_{0.5}Mn_{0.5}O_y$	Sputtering	0.7	NA	NA	1.0 M H_2SO_4	< 10 min at 10 mA cm$^{-2}_{geo}$ (LT)	22

$Ni_{0.5}Mn_{0.5}Sb_{1.7}O_y$	Sputtering	0.672 ± 0.009[a]	NA	< 10	1.0 M H_2SO_4	168 h at 10 mA cm^{-2}_{geo} (OT) η from 672 to 735 mV	22
Co_3O_4	Electron-beam evaporation	0.57	NA	NA	0.5 M H_2SO_4	15 h at 10 mA cm^{-2}_{geo} (LT)	23
Amorphous $Ti:MnO_2$	Sputtering deposition	> 0.67	NA	NA	0.5 M H_2SO_4	2 h at 1.9 V vs. RHE (OT) j from 7.2 to 6 mA cm^{-2}_{geo}	24
Amorphous $CoMnO_x$	Electrodeposition	~ 0.77[b]	NA	NA	pH 2.0 in Pi	< 1 h at 1 mA cm^{-2}_{geo} (LT)	15
Amorphous $CoFePbO_x$	Electrodeposition	~ 0.77[b]	NA	NA	pH 2.0 in Pi	50 h at 1 mA cm^{-2}_{geo} (OT) Operation time	15
Amorphous $CoPbO_x$	Electrodeposition	~ 0.62[b]	NA	NA	pH 2.5 in Pi	< 8 h at 1 mA cm^{-2}_{geo} (LT)	15
Amorphous $CoFeO_x$	Electrodeposition	~ 0.62[b]	NA	NA	pH 2.0 in Pi	< 2 h at 1 mA cm^{-2}_{geo} (LT)	15
MnO_x birnessite	Electrodeposition	NA	NA	NA	pH 1.0 in Pi	NA	25
Activated MnO_x	Voltage cycling Electrodeposition	~ 0.69[b]	NA	NA	pH 2.5 in Pi	8 h at 0.1 mA cm^{-2}_{geo} (OT)	26
Co-Fe Prussian blue-type films	Hydrothermal synthesis	0.688	NA	< 10	pH 2.0 in Pi	12 h at 0.3 mA cm^{-2}_{geo} (OT)	27
Ba[Co-POM]	Metathesis	0.5[c]	NA	NA	0.5 M H_2SO_4	0.5 h at 10 mA cm^{-2}_{geo} (OT)	28
Cs[Co-POM]	Metathesis	0.52[c]	NA	NA	0.5 M H_2SO_4	0.5 h at 10 mA cm^{-2}_{geo} (OT)	28
Ni_2Ta	Solid-state reactions	0.57	NA	NA	0.5 M H_2SO_4	66 h at 10 mA cm^{-2}_{geo} (OT) FE ~ 85%	29
MnMoCoO	Electrodeposition on IrO_2/Ti	0.305[d] at 100 mA cm^{-2}_{geo}	NA	NA	2 M H_2SO_4	NA	30
$Co_{0.05}Fe_{0.95}O_y$ on Ti foil	Spray-pyrolysis	0.65	NA	~30	pH 0.3 H_2SO_4	50 h at 10 mA cm^{-2}_{geo} (LT)	31
$Co_{0.05}Fe_{0.95}O_y$ on Ti foil	Spray-pyrolysis	0.65	NA	~30	pH 2 H_2SO_4	85 h at 10 mA cm^{-2}_{geo} (LT)	31
c-Fe_2O_3	Spray-pyrolysis	0.65	NA	NA	pH 0.3 H_2SO_4	24 h at 10 mA cm^{-2}_{geo} (OT)	32
m-Fe_2O_3	Spray-pyrolysis	~0.62	NA	NA	pH 0.3 H_2SO_4	6 h at 10 mA cm^{-2}_{geo} (LT)	32
$Ni_4Fe_5S_8$-1000	Coprecipitation	0.54	NA	NA	0.5 M H_2SO_4	NA	33
$CoFePbO_x$ on Pt/Ti mesh	Electrodeposition	0.7 at 500 mA cm^{-2}_{geo}, 60-80°C	NA	NA	pH 0 H_2SO_4	7 h at 500 mA cm^{-2}_{geo} (OT)	34
$CoFePbO_x$ on Pt/Ti mesh	Electrodeposition	~0.7 at 10 mA cm^{-2}_{geo}, 23 °C	NA	~30	pH 0 H_2SO_4	14 h at 10 mA cm^{-2}_{geo} (OT)	34
Ag-doped Co_3O_4 on FTO	Electrodeposition	0.68	NA	~12	0.5 M H_2SO_4	10 h at 6.5 mA cm^{-2}_{geo} (OT)	35
$Co_3(PO_4)_2$	Electrodeposition	~0.97 V at 1.8 mA cm^{-2}_{geo}	NA	NA	1 M H_3PO_4	30 h at 1.8 mA cm^{-2}_{geo} (OT)	36
NiFeP	Melting spinning	0.54	NA	NA	0.05 M H_2SO_4	30 h at 10 mA cm^{-2}_{geo} (OT)	37
F-doped $Cu_{1.5}Mn_{1.5}O_4$	Ball milling	0.32	NA	NA	pH 0.3 H_2SO_4	24 h at 16 mA cm^{-2}_{geo} (OT)	38
1T-MoS_2	Sonication of MoO_2	0.42	NA	NA	pH 0.3 H_2SO_4	2 h at 10 mA cm^{-2}_{geo} (OT)	39
Surface-modified Ni 42 steel sheet	Electro-oxidation in LiOH electrolyte	0.552	NA	NA	pH 1 H_2SO_4	42 h at 10 mA cm^{-2}_{geo} (OT)	40
$Mn_xSb_{1-x}O_z$	Magnetron co-sputtering	0.58 at 50 mA cm^{-2}_{geo}	NA	NA	1 M H_2SO_4	28 h at 1.72 V vs. RHE (OT) j from 7.2 to 6 mA cm^{-2}_{geo} 2 h at 10 mA cm^{-2}_{geo} (OT)	41
Spinel Co_2TiO_4	Coprecipitation	0.513	NA	NA	0.5 M H_2SO_4	10 h at 1.79 V vs. RHE (OT) j from 10 to 5 mA cm^{-2}_{geo}	42
$Cu_{1.5}Mn_{1.5}O_4$-200	High energy mechanical milling	0.324	NA	NA	0.5 M H_2SO_4	20 h at 1.55 V vs. RHE (OT) j from ~10 to 1.5 mA cm^{-2}_{geo}	43
$Cu_{1.5}Mn_{1.5}O_4$-800	High energy mechanical milling	0.352	NA	NA	0.5 M H_2SO_4	20 h at 1.55 V vs. RHE (OT) j from ~3.2 to 2.8 mA cm^{-2}_{geo}	43

[a] Overpotential after 2 h of electrolysis at 10 mA cm^{-2}_{geo}.
[b] Estimated from overpotential at 1 mA cm^{-2}_{geo} and Tafel slope values.
[c] Overpotential after 0.5 h of electrolysis at 10 mA cm^{-2}_{geo}. The overpotential for the same current density in the LSV is smaller at 0.35 V.
The reported stability is also shown as either operation time (OT, time length of electrolysis) or lifetime (LT, time until deactivation).
Pi: phosphate additive; FE: Faradaic efficiency;
[d] The authors suspect that the reported currents are not due to OER of MnMoCoO, but OER of the highly active IrO_2/Ti substrate.[30]

Supplementary Table 15. Numerical data for the Ir- and Ru-based OER catalysts in Supplementary Figure 26.

Catalyst	Catalyst loading (mg cm^{-2}_{geo})	Electrolyte	Overpotential for 10 mA cm^{-2}_{geo} (V)	Mass activity at 10 mA cm^{-2}_{geo} (A mg^{-1})	Ref	Notes
$K_{x\approx0.25}IrO_2$	0.20	0.1 M $HClO_4$	0.35	0.05	44	
3×RuO_2@SiO_2[250]	0.75	3 M H_2SO_4	0.30	0.01	45	
3×RuO_2@SiO_2[300]	0.75	3 M H_2SO_4	0.31	0.01	45	
1×RuO_2@C@SiO_2[300/Ar]	0.43	3 M H_2SO_4	0.28	0.02	45	
2×RuO_2@C@SiO_2[300/Ar]	0.74	3 M H_2SO_4	0.27	0.01	45	
2×RuO_2@C@SiO_2[350/Ar]	0.72	3 M H_2SO_4	0.27	0.01	45	
IrNi NCs	0.01	0.1 M $HClO_4$	0.28	0.80	46	
IrO_x-Ir	0.13	0.5 M H_2SO_4	0.29	0.08	47	
Ir-black	0.13	0.5 M H_2SO_4	0.33	0.08	47	
$Bi_2Ir_2O_7$	0.40	1 M H_2SO_4	0.36	0.02	48	
Ir-nano 99.8-P	0.06	0.5 M H_2SO_4	0.29	0.16	49	m_{Ir}
Ir-nano 99.8	0.06	0.5 M H_2SO_4	0.32	0.16	49	m_{Ir}
Ir-nano 99.5	0.06	0.5 M H_2SO_4	0.33	0.16	49	m_{Ir}
Ir-black UC	0.06	0.5 M H_2SO_4	0.34	0.16	49	m_{Ir}
Ir-nano 99.5\CTAB	0.06	0.5 M H_2SO_4	0.35	0.16	49	m_{Ir}
IrO_2-RuO_2@Ru (3:1)	0.38	0.5 M H_2SO_4	0.28	0.03	50	
IrO_2-RuO_2@Ru (3:1)	0.28	0.5 M H_2SO_4	0.29	0.04	50	
IrO_2-RuO_2@Ru (3:1)	0.18	0.5 M H_2SO_4	0.30	0.06	50	
IrO_2-RuO_2@Ru (3:1)	0.10	0.5 M H_2SO_4	0.32	0.10	50	
IrO_2-RuO_2@Ru (3:1)	0.08	0.5 M H_2SO_4	0.32	0.13	50	
IrO_2	0.38	0.5 M H_2SO_4	0.32	0.03	50	
IrO_2-RuO_2@Ru (1:1)	0.38	0.5 M H_2SO_4	0.31	0.03	50	
IrO_2-RuO_2@Ru (2:1)	0.38	0.5 M H_2SO_4	0.30	0.03	50	
IrO_2-RuO_2@Ru (3:1)	0.38	0.5 M H_2SO_4	0.28	0.03	50	
IrO_2-RuO_2@Ru (4:1)	0.38	0.5 M H_2SO_4	0.30	0.03	50	
IrO_2	0.38	0.5 M H_2SO_4	0.32	0.03	50	
Ir_3RuO_2	0.38	0.5 M H_2SO_4	0.29	0.03	50	
IrO_2 (CM)	0.38	0.5 M H_2SO_4	0.32	0.03	50	
RuO_2 (CM)	0.38	0.5 M H_2SO_4	0.29	0.03	50	
IrOOH nanosheet	0.20	0.1 M $HClO_4$	0.34	0.05	51	
IrOOH, bulk	0.20	0.1 M $HClO_4$	0.43	0.05	51	
IrO_2 bulk	0.20	0.1 M $HClO_4$	0.42	0.05	51	
r-IrO_2 NP	0.05	0.1 M $HClO_4$	0.44	0.20	52	
r-RuO_2 NP	0.05	0.1 M $HClO_4$	0.45	0.20	52	

6H-$SrIrO_3$	0.90	0.5 M H_2SO_4	0.25	0.01	[53]	
3C-$SrIrO_3$	0.90	0.5 M H_2SO_4	0.27	0.01	[53]	
IrO_2	0.90	0.5 M H_2SO_4	0.30	0.01	[53]	
$Cr_{0.6}Ru_{0.4}O_2$(550)	0.28	0.5 M H_2SO_4	0.18	0.04	[54]	
Ru_1-Pt_3Cu	0.02	0.1 M $HClO_4$	0.22	0.61	[55]	m_{Pt+Ru}
Ru_1-PtCu	0.02	0.1 M $HClO_4$	0.25	0.61	[55]	m_{Pt+Ru}
Cu@Ru_1-$PtCu_3$	0.02	0.1 M $HClO_4$	0.28	0.61	[55]	m_{Pt+Ru}

The data in the table was originally summarized by Kibsgaard and Chorkendorff (ref. [13]).
m_{Ir} and m_{Pt+Ru} denote the masses of the metals Ir and Pt+Ru of the catalysts reported in the literature, respectively.

Supplementary Table 16. Numerical data for non-noble metal catalysts in Supplementary Figure 26.

No[a]	Catalyst	Catalyst loading (mg cm$^{-2}_{geo}$)	Electrolyte	η (V) at 10 mA cm$^{-2}_{geo}$	Mass activity (A mg^{-1}) at 10 mA cm$^{-2}_{geo}$	Mass stability[d] (h mg^{-1})	Ref	Notes[e]
This work	Co_2MnO_4/FTO	5.00	pH 1 H_2SO_4	0.395	0.002	64 (LT) at 100 mA cm$^{-2}_{geo}$		m_{Co}
This work	Co_2MnO_4/FTO	2.50	pH 1 H_2SO_4	0.405	0.005	98 (LT) at 100 mA cm$^{-2}_{geo}$		m_{Co}
This work	Co_2MnO_4/FTO	1.00	pH 1 H_2SO_4	0.415	0.01	171 (LT) at 100 mA cm$^{-2}_{geo}$		m_{Co}
This work	Co_2MnO_4/FTO	0.50	pH 1 H_2SO_4	0.423	0.02	208 (LT) at 100 mA cm$^{-2}_{geo}$		m_{Co}
This work	Co_2MnO_4/FTO	0.20	pH 1 H_2SO_4	0.443	0.05	194 (LT) at 100 mA cm$^{-2}_{geo}$		m_{Co}
This work	Co_2MnO_4/FTO	0.10	pH 1 H_2SO_4	0.433	0.1	190 (LT) at 100 mA cm$^{-2}_{geo}$		m_{Co}
1	$Mn_{0.67}Sb_{0.33}O_z$	0.12	1 M H_2SO_4	0.51	0.084	17 (OT) at 10 mA cm$^{-2}_{geo}$	[41]	m_{Mn}
2	Spinel Co_2TiO_4	0.16[b]	0.5 M H_2SO_4	0.51	0.063[b]	62.5 (OT) at <10 mA cm$^{-2}_{geo}$	[42]	
3	$Ni_4Fe_5S_8$-1000	0.40	0.5 M H_2SO_4	0.54	0.025	NA	[33]	
4	c-Fe_2O_3	1.00	0.5 M H_2SO_4	0.65	0.010	24 (LT) at 10 mA cm$^{-2}_{geo}$	[32]	
5	$Co_{0.05}Fe_{0.95}O_y$/Ti foil	1.00	pH 2	0.65	0.010	85 (LT) at 10 mA cm$^{-2}_{geo}$	[31]	
6	$Mn_{0.8}Nb_{0.2}O_2$:10F	0.30	0.5 M H_2SO_4	0.68	0.030	83 (OT) at <10 mA cm$^{-2}_{geo}$	[21]	
7	Co-Fe Prussian blue-type films	0.30	pH 2.0 with Pi	0.69	0.033	NA	[27]	m_{Co+Fe}
8	Ba[Co-POM]	11.20	0.5 M H_2SO_4	0.50[c]	< 0.001	0.04 (OT) at 10 mA cm$^{-2}_{geo}$	[28]	m_{Co}
9	Cs[Co-POM]	12.10	0.5 M H_2SO_4	0.52[c]	< 0.001	0.04 (OT) at 10 mA cm$^{-2}_{geo}$	[28]	m_{Co}

[a] No 1-9 correspond to data points 1-9 in Supplementary Fig. 26, respectively.

[b] Estimated from figure 2 in ref [42].

[c] Overpotential after 0.5 h of electrolysis at 10 mA cm$^{-2}_{geo}$. The overpotential for the same current density in the LSV is much smaller at 0.35 V.

[d] The mass stability was calculated by Operation time (OT) or Lifetime (LT) divided by catalyst loading. The lifetime stability test for Co_2MnO_4/FTO were present in Supplementary Fig. 48.

[e] m_{Mn}, m_{Co+Fe} and m_{Co} denote the masses of the metals Mn, Co+Fe and Co of the catalysts reported in the literature, respectively.

Supplementary Table 17. Adsorption free energies for OH*, OOH* and O*.

Adsorption free energies for OH* OOH* and O* on different surfaces[#].

	G_{ad} OH*	G_{ad} OOH*	G_{ad} O*
$CoMn_2O_4$(100)	-0.25	2.71	0.39
$CoMn_2O_4$(311)	0.61	3.91	1.54
Co_2MnO_4(100)-A	-0.52	2.86	0.30
Co_2MnO_4(100)-B	0.31	3.46	1.78
Co_2MnO_4(311)-A	0.52	3.54	1.86
Co_2MnO_4(311)-B	0.57	3.75	2.00
Co_3O_4(100)-A	-0.41	2.96	0.58
Co_3O_4(100)-B	0.17	3.40	0.93
Co_3O_4(311)-A	0.32	3.69	1.18
Co_3O_4(311)-B	0.63	3.84	2.27
λ-MnO_2(100)	0.90	4.13	1.00
λ-MnO_2(311)	-0.72	2.57	-0.52
R-MnO_2(311)-A	1.24	4.38	1.79
R-MnO_2(311)-B	-0.03	3.06	0.07
β-MnO_2(311)-A	-0.18	3.07	0.50
β-MnO_2(311)-B	-0.77	2.76	0.11

[#] Free energy corrections were conducted for all of the adsorbates and gas molecules. A standard correction was applied, including zero-point energy, pressure, inner energy and entropy using the following equation:

$$E_{cor} = E_{cor}^{ZPE} + E_{cor}^{U} + E_{cor}^{P} + E_{cor}^{S} \quad (1)$$

where E_{cor}^{ZPE} refers to the correction of zero-point energy, E_{cor}^{U} and E_{cor}^{P} refer to the correction of temperature (inner energy correction) and pressure, respectively, and E_{cor}^{S} refers to the correction of entropy. The free energy correction for entropy can be separated into transitional entropy, rotational entropy and vibrational entropy; however, only vibrational entropy was considered for the surface adsorbates, which are only dependent on the vibrational frequency[56]. The frequencies for adsorbates were calculated using the finite difference method of VASP in this work, and the free energies were corrected to the temperature of 298 K. In addition, the free energy corrections were conducted for gas molecules of H_2 and H_2O with the pressure of 1.0 and 0.035 bar, respectively. The free energy of O_2(g) was calculated as:

$$G_{O_2(g)} = 1.23\ eV \times 4 + 2G_{H_2O(l)} - 2G_{H_2(g)} \quad (2)$$

The chemical potential of OH^- was calculated as:

$$G_{OH^-} = G_{H_2O(l)} - G_{H^+} \quad (3)$$

In equilibrium, the chemical potential of a pair of (H^+ + e^-) at 0 V vs. RHE was referred to the ½ chemical potential of H_2 molecules in light of the computational hydrogen electrode (CHE) approximation. The solvation effect from explicit model (see Supplementary Table 18) has been corrected into the adsorption energies.

Supplementary Table 18. Comparisons of solvent effect with explicit or implicit models.

Comparisons of solvent effect calculated using explicit or implicit models.

Solvent effect	Explicit model[#] (4-layer water)	Implicit model (VASPsol)
O*	-0.29	-0.22
OH*	-0.25	-0.28
OOH*	-0.06	-0.10

[#] We attempted to correct for the solvation effect on adsorbates due to the formation of H-bonds, which results in the stabilization of adsorptions[57]. In this work, an explicit 4-layer water model was first applied on Co_2MnO_4 (311) surfaces (Supplementary Fig. 52). Molecular dynamics (MD) simulations were performed for 2000 steps with a timestep of 0.5 femtoseconds. 5 snapshots were selected randomly from the MD simulation and the adsorption energies with explicit water in the system were calculated. Longer MD simulations were performed up to 10 ps, and solvent effects calculated by more re-optimized structures were found to be converged with an error less than 0.05 eV. The average of the calculated adsorption energies were used, namely, a stabilization for O*, OH* and OOH* was estimated to be 0.29, 0.25 and 0.06 eV, respectively. Considering the uncertainty from the explicit water layer structure, the solvation effects were also examined based on the implicit model VASPsol[58] model (Supplementary Table 18), which are comparable with the results of explicit solvation model.

Supplementary Table 19. Hubbard *U* corrections effect on reaction energies. Investigation of the effect from Hubbard *U* corrections on reaction energies. The bold numbers refer to the Δ*G*-limiting energies (ΔG_{lim}) at 1.7 V vs. RHE.

	GGA		GGA + *U*[#]	
	Co_3O_4	Co_2MnO_4	Co_3O_4	Co_2MnO_4
$H_2O(l) + * \rightarrow OH* + (H^+ + e^-)$	-1.07	-1.13	-1.06	-1.30
$OH* \rightarrow O* + (H^+ + e^-)$	**-0.06**	-0.27	**0.01**	-0.11
$O* + H_2O(l) \rightarrow OOH* + (H^+ + e^-)$	-0.14	**0.04**	-0.19	**0.03**
$OOH* \rightarrow * + O_2(g) + (H^+ + e^-)$	-0.62	-0.53	-0.64	-0.49

[#] *U* values (employed as *U* - *J*) of 4.0 and 2.0 were applied for Mn and Co.

Supplementary Table 20. Energy changes of Co and Mn sites in $CoMn_2O_4$ and Co_2MnO_4[#].

Comparisions of energy change between Co and Mn site in $CoMn_2O_4$ and Co_2MnO_4[#]

U = 1.7 V vs. RHE	Co-B site		Mn-B site	
	$CoMn_2O_4$	Co_2MnO_4	$CoMn_2O_4$	Co_2MnO_4
$H_2O(l) + * \rightarrow OH^* + (H^+ + e^-)$	-1.08	-1.13	-3.11	-2.84
$OH^* \rightarrow O^* + (H^+ + e^-)$	-0.77	-0.27	-1.59	-1.27
$O^* + H_2O(l) \rightarrow OOH^* + (H^+ + e^-)$	**0.66**	**0.04**	1.17	1.06
$OOH^* \rightarrow * + O_2(g) + (H^+ + e^-)$	-0.69	-0.53	**1.69**	**1.16**

[#] The bold numbers refer to the ΔG-limiting energies (ΔG_{lim}). Larger ΔG_{lim} was obtained on Mn site compared with that on the Co site, which indicates that the Co site is more favored as the active site for OER.

Supplementary Table 21. Description of the structures with local modifications.

Description of the structures with local modifications

Structure	Description
Co_2MnO_4-A$_{Co\_v}$	The structure describes the Mn-rich surface with a Co vacancy at the spinel A site, which was observed from the Rietveld refinement of the SR-PXRD (Supplementary Figs. 1-3). The OER activity was calculated on the adjacent Co B site (E_{ad} OH* = 0.61 eV, E_{ad} O* = 2.12 eV).
Co_2MnO_4-B$_{Co\_v}$	The structure describes the Mn-rich surface with a Co vacancy at the spinel B site as a comparison. The OER activity was calculated on the adjacent Co A site (E_{ad} OH* = 0.83 eV, E_{ad} O* = 2.38 eV).
Co_2MnO_4-AB$_{Co\_v}$	The structure describes the Mn-rich surface with a Co vacancy at both spinel A and B site as a comparison. The OER activity was calculated on the adjacent Co B site (E_{ad} OH* = 0.75 eV, E_{ad} O* = 2.29 eV).
Co_2MnO_4-A$_{Co\_v\text{-}bulk}$	The structure describes the surface with a Co vacancy at the spinel A site in the bulk phase. The OER activity was tested on Co B-site (E_{ad} OH* = 0.69 eV, E_{ad} O* = 2.10 eV).
Co_2MnO_4-B$_{3Co1Mn}$-perfect	The structure describes the case with excess Co at the B site (Co/Mn ratio > 1), which was experimentally confirmed in (Supplementary Figs. 1-3 and 7). The OER activity on Co B site was calculated (E_{ad} OH* = 0.60 eV, E_{ad} O* = 2.06 eV).
Co_2MnO_4-B$_{3Co1Mn}$- A$_{Co\_v}$	The structure describes the case of Co_2MnO_4-B$_{3Co1Mn}$ with the Co vacancy on the spinel A site. The OER activity on Co B site was calculated (E_{ad} OH* = 0.69 eV, E_{ad} O* = 2.17 eV).

Supplementary Table 22. The degree of rate control analysis.

Degree of rate control analysis describing the effect on the total rate from different elementary steps or coverages at 1.7 V vs. RHE.

Reaction[#]	**R1**	**R2**	**R3**	**R4**
R1	2.78E-11	9.77E-13	1.00E+00	1.58E-10
R2	2.78E-11	9.77E-13	1.00E+00	1.58E-10
R3	2.78E-11	9.77E-13	1.00E+00	1.58E-10
R4	2.78E-11	9.77E-13	1.00E+00	1.58E-10

Coverage	**O***	**OH***	**OOH***	**Free site**
R1	-1.00E+00	-2.62E-05	-9.71E-13	-2.78E-11
R2	-1.00E+00	-2.62E-05	-9.71E-13	-2.78E-11
R3	-1.00E+00	-2.62E-05	-9.71E-13	-2.78E-11
R4	-1.00E+00	-2.62E-05	-9.71E-13	-2.78E-11

[#] R1-R4 see equations (1)-(4) in main text.

Supplementary Table 23. Two pathways describing catalyst dissolution reaction with different priority.

Two pathways describing catalyst dissolution with different priority.

M-Path	Elementary steps
R’1	Perfect → Defect_Co/Mn_{vac} + Co/Mn[#]
R’2	Defect_Co/Mn_{vac} + H_2O → Defect_(Co/Mn_{vac}+O_{vac})-OOH* + (H^+ + e^-)
R’3	Defect_(Co/Mn_{vac}+O_{vac})-OOH* → Defect_(Co/Mn_{vac}+O_{vac}) + O_2 + (H^+ + e^-)

O-Path	Elementary steps
R’4	Perfect + H_2O → Defect_O_{vac}-OOH* + (H^+ + e^-)
R’5	Defect_O_{vac}-OOH* → Defect_O_{vac} + O_2 + (H^+ + e^-)
R’6	Defect_O_{vac} → Defect_(Co/Mn_{vac}+O_{vac}) + Co/Mn

[#] Co^{2+} and MnO_4^- were considered as the dissolution products, where the energy of Co and Mn element were referred to Co^{2+} and MnO_4^-.

Supplementary Table 24. Energetic data for the scheme of charge-extrapolation.

Energetic data for the scheme of charge-extrapolation on Co_2MnO_4.

	φ_IS	φ_TS	φ_FS	q_IS[#]	q_TS	q_FS	E_{TS-IS}	E_{FS-IS}
$H_2O(l) + * \rightarrow OH* + (H^+ + e^-)$	4.63	3.72	3.68	0.00	0.93	0.94	0.61	0.66
$OH* \rightarrow O* + (H^+ + e^-)$	5.02	3.88	3.79	0.00	0.92	0.94	1.06	1.11
$O* + H_2O(l) \rightarrow OOH* + (H^+ + e^-)$	4.99	4.20	3.70	0.00	0.63	0.92	1.19	1.18
$OOH* \rightarrow * + O_2(g) + (H^+ + e^-)$	4.65	3.99	3.73	0.00	0.85	0.89	0.34	0.14

[#] The charge transfer in IS was corrected to 0 as a reference.

Supplementary Notes

Supplementary Note 1. Rietveld analysis

The crystal structures of the as-synthesized Co_2MnO_4 and those after electrolysis for 4 h and 23 h were refined with the Rietveld analysis using the RIETAN-FP software.[59] The occupancies of the Co and Mn atoms at the A and B sites in the spinel structure were constrained on the refinements based on the results of the ICP-MS and the XANES measurements.

Initial values and constraints of the Co and Mn site occupancies on the Rietveld refinements. When the chemical compositions of the Co and Mn in the analyzed materials are denoted x and y, respectively, the formula can be described as $Co_xMn_yO_4$. The Co/Mn ratio was fixed to be 2, that is $M = x/y = 2$, based on the ICP-MS results (Supplementary Fig. 4). The average atomic valence of Co and Mn were obtained from the XANES K-edge (Supplementary Figs. 5 and 6). For example, the average valence of the Co and Mn were $v_{\text{Co}} = 2.37$ and $v_{\text{Mn}} = 3.67$ in the as-synthesized material. Since the valency of all the oxygen atoms can be assumed to be -2, the relation among the Co and Mn compositions and valences were described as:

$$v_{\text{Co}} \bullet x + v_{\text{Mn}} \bullet y = 8 \tag{4}$$

By substitution of $M = x/y$ we have

$$x = \frac{8M}{Mv_{\text{Co}} + v_{\text{Mn}}} \tag{5}$$

and

$$y = \frac{8}{Mv_{\text{Co}} + v_{\text{Mn}}} \tag{6}$$

The EXAFS data of the Co K-edge indicates that Co is located at both A and B sites, whereas the Mn K-edge indicate that Mn is located only at the B site (Supplementary Fig. 7). In order to reflect this information, we have used the following chemical structure for the EXAFS fitting:

$$[\text{Co}_{g\text{CoA}}\square_{1-g\text{CoA}}]_{\text{A}}\ [\text{Co}_{2g\text{CoB}}\ \text{Mn}_{2g\text{MnB}}\ \square_{2-2g\text{CoB}-2g\text{MnB}}]_{\text{B}}\ \text{O}_4 \tag{7}$$

Here, □ indicates a vacancy. g_{CoA}, g_{CoB}, and g_{MnB} indicates the occupancy of the A-site Co, the B-site Co, and the B-site Mn. Comparison with the chemical composition $Co_xMn_yO_4$ yields:

$$g_{\text{CoA}} + 2g_{\text{CoB}} = x = \frac{8M}{Mv_{\text{Co}} + v_{\text{Mn}}} \tag{8}$$

$$g_{\text{CoA}}2g_{\text{MnB}} = y = \frac{8}{Mv_{\text{Co}} + v_{\text{Mn}}} \tag{9}$$

The preliminary Rietveld refinements were performed under the assumption $M = 2$. When the v_{Co} and v_{Mn} values obtained from EXAFS were introduced into equations (8) and (9), the occupancy of the B site exceeded 1 ($g_{\mathrm{CoB}} + g_{\mathrm{MnB}} > 1$) for all 3 samples. This indicates that the B-site is fully occupied, and therefore, we can assume

$$g_{\mathrm{CoB}} + g_{\mathrm{MnB}} = 1 \tag{10}$$

As $M = 2$, equations (8) and (9) yield:

$$g_{\mathrm{CoA}} + 2g_{\mathrm{CoB}} = 2 \cdot 2g_{\mathrm{MnB}} \tag{11}$$

Based on equations (10) and (11), we obtain the following B-site occupancies:

$$g_{\mathrm{CoB}} = -\frac{1}{6}g_{\mathrm{CoA}} + \frac{2}{3} \tag{12}$$

and

$$g_{\mathrm{MnB}} = \frac{1}{6}g_{\mathrm{CoA}} + \frac{1}{3} \tag{13}$$

The occupancies of the Co and Mn were constrained with equations (12) and (13) on the Rietveld refinements in Supplementary figures 1-3. In this analysis, the oxygen occupancy was fixed to 1 according to the previous literature[60]. The isotropic atomic displacement parameters of $\mathrm{Co_B}$ and $\mathrm{Mn_B}$ were constrained to be the same.

Supplementary Note 2. Fitting and Simulation of EXAFS

The XAFS analysis was performed on the Demeter software platform[61]. Fourier transforms were applied to all the k^3-weighted Co K-edge EXAFS spectra from $k = 3$ Å^{-1} to 14 Å^{-1} to obtain radial distribution functions with ATHENA software.

Co K-edge EXAFS fitting. EXAFS fitting in *R*-space for the standard Co_3O_4 sample was conducted first with *R* range of 1 - 3.5 Å with ARTEMIS software. A CIF file of cubic spinel Co_3O_4 (ICSD code 36256) from ICSD, Inorganic Crystal Structure Database, was used as an initial model. Since Co atoms occupied both A site (Tetrahedral site, Co_A) and B site (Octahedral site, Co_B), the scattering paths were calculated by running FEFF6 separately by setting either of A site or B site as an absorber, and paths from both calculations were used for the fitting. Three representative single-scattering paths for each calculation were included: Co_A-O (1st shell), Co_A-Co_B, and Co_A-Co_A for Co_A core; Co_B-O (1st shell), Co_B-Co_B, and Co_B-Co_A for Co_B core. The amplitude reduction factor, S_0^2, for these two sites were set to be the same value and allowed to float. A fractional occupancy factors of 1/3 for A site and 2/3 for B site were multiplied to separate the contribution from these two sites. The same value of energy shift ΔE_0 that aligns the energy grid of the calculation with the energy grid of the data was used for all the path which is commonly used in the EXAFS fitting[62]. The coordination number for all the paths were fixed to the crystallography values of spinel structure. The amplitude reduction factor, S_0^2, energy shift, ΔE_0, the changes in path length from the theoretical values, ΔR, and Debye-Waller factors, σ^2, were refined through the fitting process. The final fitting result and parameters were shown in Supplementary Figure 8 and Table 4.

The fitting of Co_2MnO_4 was based on the procedure described in the Chapter 15.10. in the Artemis manual[63]. The initial structure model of Co_2MnO_4 were obtained from the Rietveld refinement result of synchrotron-radiation powder XRD of Co_2MnO_4 in Supplementary Table 1. The scattering paths were calculated by running FEFF6 separately by setting either of A site or B site Co as an absorber, and paths from both calculations were used for the fitting. Four representative single-scattering paths for each calculation were included: Co_A-O (1st shell), Co_A-Co_B, Co_A-Mn_B, and Co_A-Co_A for Co_A core; Co_B-O (1st shell), Co_B-Co_B, Co_B-Mn_B, and Co_B-Co_A for Co_B core. The S_0^2 for these two sites were fixed to 0.85, the same value obtained by fitting of the standard Co_3O_4 sample, and multiplied by the appropriate fractional occupancy elucidated from the Rietveld analysis. Energy shifts, ΔE_0, were fixed for all the paths to 1.6 eV, the value calculated from Co_3O_4. Same ΔR and σ^2 were used for Co_A-O and Co_B-O paths, both of which contributed to the first shell, considering the path lengths were generally too close to be distinguished by EXAFS. The coordination numbers were allowed to float. For the second and third shells, single scattering paths of Co-M (M = Co or Mn) were included. The distance with scattering atoms in octahedral B site was split into Co_B-Co_B and Co_B-Mn_B because the octahedral site was occupied by both Co and Mn while imposing same distance ΔR and Debye-Waller factor σ^2. Moreover, Co_A-Co_B and Co_B-Co_A scattering path present the same distance.

Therefore, same ΔR and Debye-Waller factor σ^2 were used for these two paths. Finally, the coordination number for all these paths were fixed to the value calculated by multiplying the occupancy of scattering atoms to the crystallography values of spinel structure. The fitting result and parameters were shown in Supplementary Figure 9 and Supplementary Table 6.

Mn K-edge EXAFS fitting. EXAFS fitting in *R*-space for the standard β-MnO_2 sample was conducted first with *R* range of 1-3.5 Å. The single scattering paths of Mn-O, Mn-Mn.1 (second shell) and Mn-Mn.2 (third shell) were included for fitting. The coordination number for all the paths were fixed to the crystallography values. The amplitude redactor factor, S_0^2, energy shift, ΔE_0, the changes in path length from the theoretical values, ΔR, and Debye-Waller factors, σ^2, were refined through the fitting process. The fitting result and parameters were shown in Supplementary figure 8 and Supplementary Table 5. Obtained value of S_0^2 (0.78) and ΔE_0 (0.2) were used for the fitting of Mn K-edge EXAFS of Co_2MnO_4. The scattering paths were calculated by running FEFF6 by setting Mn in octahedral B site as an absorber. The single scattering paths of Mn_B-O.1 (first shell), Mn_B-Mn_B, Mn_B-Co_B, Mn_B-Co_A and Mn_B-O.3 (third shell) were included for the fitting. The distance with scattering atoms in the octahedral B site was split into Mn_B-Co_B and Mn_B-Mn_B because octahedral site was occupied by both Co and Mn while imposing same distance ΔR and Debye-Waller factor σ^2. The other paths were set with additional distance ΔR and Debye-Waller factor σ^2. The coordination number for Mn_B-O.1 was let free while other paths were fixed to the value calculated by multiplying the occupancy of scattering atoms to the crystallography value of spinel structure. The fitting result and parameters were shown in Supplementary Figure 10 and Supplementary Table 7.

The parameters of the above fittings were physically reasonable[62] and the *R*-factors validates the rationality of our fitting.

Simulation made on Co_2MnO_4 model with various Co vacancies. The simulation was conducted with the same procedure as that for Co K-edge EXAFS fitting of Co_2MnO_4. All the parameters including the amplitude reduction factor S_0^2, the energy shift ΔE_0, the changes in path length from the theoretical values, ΔR, and Debye-Waller factors, σ^2, were fixed to the values obtained by fitting Co_2MnO_4 before electrolysis. The initial occupancy of 0.841 for Co in A site and 0.527 for Co in B site were used. The simulation on the EXAFS spectra with Co vacancies in A site was conducted by fixing the B site occupancy as the initial value, while A site occupancy was multiplied by g_A factor varying from 100% to 0%. Therefore, the g_A factor was involved to correct the site contribution to S_0^2 and the coordination number of the paths with A site Co as scattering atoms (Co_A-Co_A and Co_B-Co_A)[64]. The simulation on the EXAFS spectra with Co vacancies in B site was conducted by fixing the A site occupancy as the initial value, while B site occupancy was multiplied by g_B factor varying from 100% to 0%. Therefore, the g_B factor was involved to correct the site contribution to S_0^2 and the coordination number of the paths with B site Co as scattering atoms (Co_B-Co_B and Co_A-Co_B)[64]. The simulation result was shown in Supplementary Figure 11.

Supplementary Note 3. Discussion on H_2SO_4 oxidation for Supplementary figure 18

Although Qixi et al.[65] have reported the possibility of H_2SO_4 oxidation, we deny the possibility of it occurring in our study based on the following 3 considerations:

(1) The equilibrium potential for the oxidation of HSO_4^- to $S_2O_8^{2-}$ is 2.12 V vs. RHE. This is above the maximum potential (2 V vs. RHE after *iR* corrections) applied on our Co_2MnO_4 catalyst, and therefore, the electrochemical oxidation of H_2SO_4 to $S_2O_8^{2-}$ is thermodynamically improbable.

$$2\mathrm{HSO_4^-(aq)} \rightarrow \mathrm{S_2O_8^{2-}(aq)} + 2\mathrm{H^+} + 2\mathrm{e^-}, E^0 = 2.12\ \mathrm{V\ vs.RHE} \quad (14)$$

We believe that photocatalytic oxidation of H_2SO_4 occurred in the study recommended by the reviewer because the photogenerated holes of WO_3 have an equilibrium potential of 3 V vs. RHE.

(2) We have performed the colorimetry procedure based on the EES paper above[65]. No $S_2O_8^{2-}$ could be detected from the electrolyte (Supplementary Fig. 18). Namely, no peak assignable to $[Fe(SCN)_6]^{3-}$, which is the titration product of $S_2O_8^{2-}$, was observed after electrolysis (100 mA cm^{-2}_{geo} at 1.72 V vs RHE after *iR* correction for 23 hours).

(3) We have confirmed that the dioxygen is generated from water, based on isotope labeling experiments. Namely, when OER was conducted in $H_2{}^{18}O$ (^{18}O purity ≥ 98 atom%) using $H_2S^{16}O_4$ as the electrolyte at pH 0, $^{18}O^{18}O$ ($m/z = 36$) was the dominant O_2 product (> 97%, Supplementary Fig. 17). A small peak assigned to $^{16}O^{18}O$ ($m/z = 34$) were observed with a percentage of < 3%, which is consistent with the portion of $H_2{}^{16}O$ in $H_2{}^{18}O$. As the isotope exchange between $H_2S^{16}O_4$ and $H_2{}^{18}O$ is negligible[66] (2.16×10^{-8} M s^{-1} at 25 °C), the $^{18}O^{18}O$ detected is not due to H_2SO_4 oxidation.

Supplementary References

1 Julien, C., Massot, M., Rangan, S., Lemal, M. & Guyomard, D. Study of structural defects in γ-MnO_2 by Raman spectroscopy. *J. Raman Spectrosc.* **33**, 223-228 (2002).

2 Hadjiev, V. G., Iliev, M. N. & Vergilov, I. V. The Raman spectra of Co_3O_4. *J. Phys. C: Solid State Phys.* **21**, L199-L201 (1988).

3 Gnezdilov, V. P. *et al.* Phonon Raman scattering in $LaMn_{1-x}Co_xO_3$ (x=0, 0.2, 0.3, 0.4, and 1.0). *Low Temp. Phys.* **29**, 963-966 (2003).

4 Iliev, M. N. *et al.* Monitoring B-site ordering and strain relaxation in $NiFe_2O_4$ epitaxial films by polarized Raman spectroscopy. *Phys. Rev. B Condens. Matter* **83**, 014108 (2011).

5 Oku, M. & Hirokawa, K. X-ray photoelectron spectroscopy of Co_3O_4, Fe_3O_4, Mn_3O_4, and related compounds. *J. Electron. Spectrosc. Relat. Phenom* **8**, 475-481 (1976).

6 Okamoto, Y., Imanaka, T. & Teranishi, S. Surface structure of CoO-MoO_3/Al_2O_3 catalysts studied by X-ray photoelectron spectroscopy. *J. Catal.* **65**, 448-460 (1980).

7 Dupin, J. C., Gonbeau, D., Benqlilou-Moudden, H., Vinatier, P. & Levasseur, A. XPS analysis of new lithium cobalt oxide thin-films before and after lithium deintercalation. *Thin Solid Films* **384**, 23-32 (2001).

8 Ilton, E. S., Post, J. E., Heaney, P. J., Ling, F. T. & Kerisit, S. N. XPS determination of Mn oxidation states in Mn (hydr)oxides. *Appl. Surf. Sci.* **366**, 475-485 (2016).

9 Navrotsky, A. & Kleppa, O. J. The thermodynamics of cation distributions in simple spinels. *J. Inorg. Nucl. Chem.* **29**, 2701-2714 (1967).

10 Zhao, Q., Yan, Z., Chen, C. & Chen, J. Spinels: Controlled preparation, oxygen reduction/evolution reaction application, and beyond. *Chem. Rev.* **117**, 10121-10211 (2017).

11 Hitz, C. & Lasia, A. Experimental study and modeling of impedance of the her on porous Ni electrodes. *Journal of Electroanalytical Chemistry* **500**, 213-222 (2001).

12 McCrory, C. C. *et al.* Benchmarking hydrogen evolving reaction and oxygen evolving reaction electrocatalysts for solar water splitting devices. *J. Am. Chem. Soc.* **137**, 4347-4357 (2015).

13 Kibsgaard, J. & Chorkendorff, I. Considerations for the scaling-up of water splitting catalysts. *Nat. Energy* **4**, 430-433 (2019).

14 Geiger, S. *et al.* The stability number as a metric for electrocatalyst stability benchmarking. *Nat. Catal.* **1**, 508-515 (2018).

15 Huynh, M., Ozel, T., Liu, C., Lau, E. C. & Nocera, D. G. Design of template-stabilized active and earth-abundant oxygen evolution catalysts in acid. *Chem. Sci.* **8**, 4779-4794 (2017).

16 Morales Cano, F. *Manganese promotion in titania-supported cobalt Fischer-Tropsch catalysis*, Utrecht University, (2006).

17 Burke, M. S., Kast, M. G., Trotochaud, L., Smith, A. M. & Boettcher, S. W. Cobalt–Iron (oxy)hydroxide oxygen evolution electrocatalysts: the role of structure and composition on activity, stability, and mechanism. *J. Am. Chem. Soc.* **137**, 3638-3648 (2015).

18 Burke, M. S. *et al.* Revised oxygen evolution reaction activity trends for first-row transition-metal (oxy)hydroxides in alkaline media. *J. Phys. Chem. Lett.* **6**, 3737-3742 (2015).

19 Wagner, C. D. *et al.* Empirical atomic sensitivity factors for quantitative analysis by electron spectroscopy for chemical analysis. *Surf. Interface Anal.* **3**, 211-225 (1981).

20 Li, A. *et al.* Stable potential windows for long-term electrocatalysis by manganese oxides under acidic conditions. *Angew. Chem. Int. Ed.* **58**, 5054-5058 (2019).

21 Ghadge, S. D. *et al.* Computational and experimental study of fluorine doped $(Mn_{1-x}Nb_x)O_2$ nanorod electrocatalysts for acid-mediated oxygen evolution reaction. *ACS Applied Energy Materials* **3**, 541-557 (2020).

22 Moreno-Hernandez, I. A. *et al.* Crystalline nickel manganese antimonate as a stable water-oxidation catalyst in aqueous 1.0 M H_2SO_4. *Energy Environ. Sci.* **10**, 2103-2108 (2017).

23 Mondschein, J. S. *et al.* Crystalline cobalt oxide films for sustained electrocatalytic oxygen evolution under strongly acidic conditions. *Chem. Mater.* **29**, 950-957 (2017).

24 Frydendal, R., Paoli, E. A., Chorkendorff, I., Rossmeisl, J. & Stephens, I. E. L. Toward an active and stable catalyst for oxygen evolution in acidic media: Ti-stabilized MnO_2. *Adv. Energy Mater.* **5**, 1500991 (2015).

25 Huynh, M., Bediako, D. K. & Nocera, D. G. A functionally stable manganese oxide oxygen evolution catalyst in acid. *J. Am. Chem. Soc.* **136**, 6002-6010 (2014).

26 Huynh, M., Shi, C., Billinge, S. J. & Nocera, D. G. Nature of activated manganese oxide for oxygen evolution. *J. Am. Chem. Soc.* **137**, 14887-14904 (2015).

27 Han, L. *et al.* Enhanced activity and acid pH stability of Prussian blue-type oxygen evolution electrocatalysts processed by chemical etching. *J. Am. Chem. Soc.* **138**, 16037-16045 (2016).

28 Blasco-Ahicart, M., Soriano-Lopez, J., Carbo, J. J., Poblet, J. M. & Galan-Mascaros, J. R. Polyoxometalate electrocatalysts based on earth-abundant metals for efficient water oxidation in acidic media. *Nat. Chem.* **10**, 24-30 (2018).

29 Mondschein, J. S. *et al.* Intermetallic Ni_2Ta electrocatalyst for the oxygen evolution reaction in highly acidic electrolytes. *Inorg. Chem.* **57**, 6010-6015 (2018).

30 Delgado, D., Minakshi, M., McGinnity, J. & Kim, D.-J. Co/Mo bimetallic addition to electrolytic manganese dioxide for oxygen generation in acid medium. *Sci. Rep.* **5**, 15208 (2015).

31 Kwong, W. L., Lee, C. C., Shchukarev, A. & Messinger, J. Cobalt-doped hematite thin films for electrocatalytic water oxidation in highly acidic media. *Chem. Commun.* **55**, 5017-5020 (2019).

32 Kwong, W. L., Lee, C. C., Shchukarev, A., Björn, E. & Messinger, J. High-performance iron (III) oxide electrocatalyst for water oxidation in strongly acidic media. *J. Catal.* **365**, 29-35 (2018).

33 Hu, Q. *et al.* Coupling pentlandite nanoparticles and dual-doped carbon networks to yield efficient and stable electrocatalysts for acid water oxidation. *Journal of Materials Chemistry A* **7**, 461-468 (2019).

34 Chatti, M. *et al.* Intrinsically stable in situ generated electrocatalyst for long-term oxidation of acidic water at up to 80 °C. *Nat. Catal.* **2**, 457-465 (2019).

35 Yan, K.-L. *et al.* Mesoporous Ag-doped Co_3O_4 nanowire arrays supported on FTO as efficient electrocatalysts for oxygen evolution reaction in acidic media. *Renew. Energy* **119**, 54-61 (2018).

36 Bloor, L. G., Molina, P. I., Symes, M. D. & Cronin, L. Low pH electrolytic water splitting using earth-abundant metastable catalysts that self-assemble in situ. *J. Am. Chem. Soc.* **136**, 3304-3311 (2014).

37 Hu, F. *et al.* Amorphous metallic NiFeP: A conductive bulk material achieving high activity for oxygen evolution reaction in both alkaline and acidic media. *Adv. Mater.* **29**, 1606570 (2017).

38 Patel, P. P. *et al.* Noble metal-free bifunctional oxygen evolution and oxygen reduction acidic media electro-catalysts. *Sci. Rep.* **6**, 28367 (2016).

39 Wu, J. *et al.* Exfoliated 2D transition metal disulfides for enhanced electrocatalysis of oxygen evolution reaction in acidic medium. *Adv. Mater. Inter.* **3**, 1500669 (2016).

40 Schäfer, H. *et al.* Steel-based electrocatalysts for efficient and durable oxygen evolution in acidic media. *Catal. Sci. Technol.* **8**, 2104-2116 (2018).

41 Zhou, L. *et al.* Rutile alloys in the Mn–Sb–O system stabilize Mn^{3+} to enable oxygen evolution in strong acid. *ACS Catal.* **8**, 10938-10948 (2018).

42 Anantharaj, S., Karthick, K. & Kundu, S. Spinel cobalt titanium binary oxide as an all-non-precious water oxidation electrocatalyst in acid. *Inorg. Chem.* **58**, 8570-8576 (2019).

43 Ghadge, S. D. *et al.* Influence of defects on activity-stability of $Cu_{1.5}Mn_{1.5}O_4$ for acid-mediated oxygen evolution reaction. *J. Electrochem. Soc.* **167** (2020).

44 Sun, W., Song, Y., Gong, X.-Q., Cao, L.-m. & Yang, J. Hollandite structure $K_{x\approx0.25}IrO_2$ catalyst with highly efficient oxygen evolution reaction. *ACS Applied Materials & Interfaces* **8**, 820-826 (2016).

45 DeSario, P. A., Chervin, C. N., Nelson, E. S., Sassin, M. B. & Rolison, D. R. Competitive oxygen evolution in acid electrolyte catalyzed at technologically relevant electrodes painted with nanoscale RuO_2. *ACS Applied Materials & Interfaces* **9**, 2387-2395 (2017).

46 Pi, Y., Shao, Q., Wang, P., Guo, J. & Huang, X. General formation of monodisperse IrM (M = Ni, Co, Fe) bimetallic nanoclusters as bifunctional electrocatalysts for acidic overall water splitting. *Advanced Functional Materials* **27**, 1700886 (2017).

47 Lettenmeier, P. *et al.* Nanosized IrO(x)-Ir catalyst with relevant activity for anodes of proton exchange membrane electrolysis produced by a cost-effective procedure. *Angew Chem Int Ed Engl* **55**, 742-746 (2016).

48 Sardar, K. *et al.* Bismuth Iridium oxide oxygen evolution catalyst from hydrothermal synthesis. *Chem. Mater.* **24**, 4192-4200 (2012).

49 Lettenmeier, P. *et al.* Highly active nano-sized iridium catalysts: synthesis and operando spectroscopy in a proton exchange membrane electrolyzer. *Chem. Sci.* **9**, 3570-3579 (2018).

50 Li, G., Li, S., Ge, J., Liu, C. & Xing, W. Discontinuously covered IrO_2–RuO_2@Ru electrocatalysts for the oxygen evolution reaction: how high activity and long-term durability can be simultaneously realized in the synergistic and hybrid nano-structure. *Journal of Materials Chemistry A* **5**, 17221-17229 (2017).

51 Weber, D. *et al.* IrOOH nanosheets as acid stable electrocatalysts for the oxygen evolution reaction. *Journal of Materials Chemistry A* **6**, 21558-21566 (2018).

52 Lee, Y., Suntivich, J., May, K. J., Perry, E. E. & Shao-Horn, Y. Synthesis and activities of rutile IrO_2 and RuO_2 nanoparticles for oxygen evolution in acid and alkaline solutions. *J. Phys. Chem. Lett.* **3**, 399-404 (2012).

53 Yang, L. *et al.* Efficient oxygen evolution electrocatalysis in acid by a perovskite with face-sharing IrO_6 octahedral dimers. *Nat. Commun.* **9**, 5236 (2018).

54 Lin, Y. *et al.* Chromium-ruthenium oxide solid solution electrocatalyst for highly efficient oxygen evolution reaction in acidic media. *Nat. Commun.* **10**, 162 (2019).

55 Yao, Y. *et al.* Engineering the electronic structure of single atom Ru sites via compressive strain boosts acidic water oxidation electrocatalysis. *Nat. Catal.* **2**, 304-313 (2019).

56 Cao, X.-M., Burch, R., Hardacre, C. & Hu, P. An understanding of chemoselective hydrogenation on crotonaldehyde over Pt(111) in the free energy landscape: the microkinetics study based on first-principles calculations. *Catal. Today* **165**, 71-79 (2011).

57 Calle-Vallejo, F., Martínez, J. I., García-Lastra, J. M., Abad, E. & Koper, M. T. M. Oxygen reduction and evolution at single-metal active sites: Comparison between functionalized graphitic materials and protoporphyrins. *Surf. Sci.* **607**, 47-53 (2013).

58 Mathew, K., Sundararaman, R., Letchworth-Weaver, K., Arias, T. A. & Hennig, R. G. Implicit solvation model for density-functional study of nanocrystal surfaces and reaction pathways. *J. Chem. Phys.* **140**, 084106 (2014).

59 Izumi, F. & Momma, K. Three-Dimensional Visualization in Powder Diffraction. *Solid State Phenomena* **130**, 15-20 (2007).

60 Wei, C. *et al.* Cations in octahedral sites: A descriptor for oxygen electrocatalysis on transition-metal spinels. *Adv. Mater.* **29**, 1606800 (2017).

61 Ravel, B. & Newville, M. ATHENA, ARTEMIS, HEPHAESTUS: data analysis for X-ray absorption spectroscopy using IFEFFIT. *J. Synchrotron Radiat.* **12**, 537-541 (2005).

62 Ravel, B. in *X‐Ray Absorption and X‐Ray Emission Spectroscopy* 281-302 (2016).

63 Artemis: EXAFS Data Analysis using Feff with Larch or Ifeffit. *https://bruceravel.github.io/demeter/documents/Artemis/extended/dopants.html*.

64 Saratovsky, I., Wightman, P. G., Pastén, P. A., Gaillard, J.-F. & Poeppelmeier, K. R. Manganese Oxides: Parallels between Abiotic and Biotic Structures. *J. Am. Chem. Soc.* **128**, 11188-11198 (2006).

65 Mi, Q., Zhanaidarova, A., Brunschwig, B. S., Gray, H. B. & Lewis, N. S. A quantitative assessment of the competition between water and anion oxidation at WO_3 photoanodes in acidic aqueous electrolytes. *Energy Environ. Sci.* **5**, 5694-5700 (2012).

66 Hoering, T. C. & Kennedy, J. W. The exchange of oxygen between sulfuric acid and water1. *J. Am. Chem. Soc.* **79**, 56-60 (1957).